Study on Spherical Microlasers Levitated in an Ion Trap

Masahide TONA

Course of Intelligent Mechanical Systems Engineering,

KOCHI UNIVERSITY OF TECHNOLOGY

A Dissertation Submitted to the Faculty of
Kochi University of Techology in Partial Fulfillment of
the Requirement for the Degree of

Doctor of Engineering

September 2002

Study on Spherical Microlasers Levitated in an Ion Trap

by

Masahide TONA

A Dissertation Submitted to the Faculty of
Kochi University of Techology in Partial Fulfillment of
the Requirement for the Degree of

Doctor of Engineering

Approved by:

Masahiro KIMURA (Director)

Yoshio INOUE

Yoichi NOJIRI

Masaoki FURUE

Koichi OKA

ABSTRACT

Study on Spherical Microlasers Levitated in an Ion Trap

Masahide TONA
Course of Intelligent Mechanical Systems Engineering,
Kochi University of Technology
September 2002
Director: Prof. Masahiro KIMURA

Optical processes in micrometer-sized spherical particles have been studied extensively in recent years. Light waves traveling along a circumference of a spherical particle are efficiently confined near the surface by almost total internal reflection. If they round the circumference in phase, resonant standing waves are produced along the great circles. Such resonances are called "morphology dependent resonances (MDRs)" because the resonance frequencies strongly depend on the size parameter defined as the ratio of a radius of the sphere to the light wavelength. The particle acts as a high Q resonator and exhibits a variety of linear and nonlinear optical effects in elastic scattering, fluorescence, laser emission and Raman scattering.

In order to obtain fundamental information on optical properties of spherical microlasers, we have investigated laser actions of dye-doped microdroplets in an ion trap. Unlike spherical microparticles around wires or on substrates employed by other investigators, the single droplets isolated in the ion trap are not supported by any material and are naturally shaped into almost perfect spheres owing to surface tension. The ion trap technique is hence ideally suited to the studies on the spherical microlasers.

Droplets composed of liquid glycerol doped with rhodamine 6G molecules were generated by a method of electrospray ionization and injected into the ion trap. A droplet in the ion trap was irradiated by an SHG radiation of a Q-switched

Nd:YAG laser (532 nm, pulse width of 10 ns). Perpendicularly emitted radiation from the droplet was spectrally recorded by using a spectrometer equipped with a charge-coupled device (CCD) detector, and the radiating images were photographed with a color CCD camera mounted on a microscope.

In this study, the following novel phenomena have been revealed and analyzed:

(a) Microscopic images of the lasing droplet exhibit symmetrically arranged bright spots near the surface,

(b) Polarization of laser light waves from the droplet strongly depend on the observation direction and the polarization of exciting light,

(c) The polarization properties are very useful to identify the lasing modes of spherical microlasers, and

(d) The density and the polarization of lasing modes are closely related to concentration of the dye molecules.

This thesis is organized as follows. In Chap. 1, Introduction, a review of various researches in this field and motivation of this work are stated. In Chap. 2, Optical Properties of Spherical Particles, we introduce the Mie theory and discuss MDRs. Chapter 3, Experimental Details, describes the ion trap technique and observation methods of emission from single droplets confined in the ion trap. In Chap. 4, Results and Discussion, the novel phenomena, as mentioned above, are described and discussed in detail. In Chap. 5, Conclusion, the summary and the future development of this study are stated.

© Copyright by
Masahide Tona
2002
All Rights Reserved

Acknowledgements

First of all, I would like to express my sincere gratitude to my director Prof. Masahiro Kimura who introduced me to this field of experimental research and continuously guided me.

I am grateful to my thesis committee members, Prof. Yoshio Inoue, Prof. Yoichi Nojiri, Prof. Masaoki Furue and Associate Prof. Koichi Oka for their valuable input and technical advice.

I would like to thank Mr. Tomoaki Takaichi, a member of the Kimura group, for his contribution to the development of the laser manipulation system.

I would like to acknowledge a scholarship for my thesis research from Kochi University of Technology.

I also acknowledge partly support by the Grants-in-Aid for Scientific Research (No. 14750034) from the Ministry of Education, Culture, Sports, Science and Technology.

Finally, I am much grateful to my wife Naomi. Without her encouragement and understanding this work has not been completed.

Table of Contents

List of Tables **xv**

List of Figures **xxii**

1 Introduction **1**

1.1 Historical Remarks 1

1.2 Motivation of the Present Study 4

1.3 Outline of the Present Thesis 5

2 Optical Properties of Spherical Particles **7**

2.1 Solutions to Vector Wave Equations 7

2.1.1 Vector wave equations 8

2.1.2 Vector functions satisfying vector wave equations 11

2.1.3 Solutions to the scalar wave equation in spherical polar coordinates 12

2.1.4 Vector spherical functions 17

2.1.5 Orthogonal relations of vector wave functions 18

2.2 The Mie Theory 20

2.2.1 Expansion of an incident, an inside and a scattered waves in vector wave functions 21

2.2.2 Derivation of expansion coefficients of inside and scattered waves 26

2.2.3 Characteristics of scattering coefficients 29

2.3 Morphology Dependent Resonances 32
  2.3.1 Simple model of MDRs 32
  2.3.2 Spatial characteristics of MDRs 35
  2.3.3 Quality factors of MDRs 38
  2.3.4 Analogy between MDRs and hydrogen atom 40

3 Experimental Details **43**
3.1 Ion Trap Technique 43
  3.1.1 Trapping of charged particles in three dimensional quadrupole fields 43
  3.1.2 Ion trap employed in this study 47
  3.1.3 Single microdroplet levitated in the ion trap 51
3.2 Observation Methods of Emission from Single Droplets 52
  3.2.1 Overview of the experimental apparatus 53
  3.2.2 Specifications of the main instruments 54
  3.2.3 Methods for simultaneously obtaining emission spectra and microscopic images 59

4 Results and Discussion **63**
4.1 Dependence of Lasing Modes on Pump Intensity 63
  4.1.1 Experimental setup 63
  4.1.2 Emission spectra from microdroplet for various pump intensities 64
  4.1.3 Spatial images of microdroplet for various pump intensities 66
  4.1.4 Discussion 66
  4.1.5 Summary 69
4.2 Polarization Properties of Lasing Modes 69
  4.2.1 Experimental setup 70
  4.2.2 Polarization phenomena obtained from microscopic images of lasing droplets 71
  4.2.3 Identification of Polarization of MDRs 72

4.2.4 Discussion 74

4.2.5 Summary 77

4.3 Dependence of Lasing Modes on Dye Concentration 78

4.3.1 Experimental setup 78

4.3.2 Microscopic images of microdroplets 79

4.3.3 Emission spectra of microdroplets 80

4.3.4 Mode identification of MDRs 83

4.3.5 Discussion 85

4.3.6 summary 87

5 Conclusion 89

5.1 Summary of the Present Work 89

5.2 Future Development of this Study 91

Appendix A Drawings of Ion Trap Assembly 97

Appendix B Laser Manipulation System 99

Bibliography 103

List of Tables

I The first few associated Legendre functions. 14

II The first two orders Bessel functions of the first and second kind. 15

III The resonance size parameters and the quality factors of TE MDRs with $l = 60$ and $s = 1$, 2 and 3. 39

IV The resonance size parameters and the quality factors of the first order TE MDRs with $l = 30$, 45 and 60. 40

V Mode identification of MDRs for droplets with various dye concentrations. 85

List of Figures

2.1 Spherical polar coordinates. 13

2.2 (A)Spherical Bessel functions of the first kind. (B)Spherical Bessel functions of the second kind (spherical Neumann functions). . . . 16

2.3 Three light waves; the linearly polarized incident plane wave, the spherical wave inside the sphere and the spherical wave scattered by the sphere. 21

2.4 The incident plane wave whose propagation direction and polarization are parallel to the z- and x-axes, respectively. 22

2.5 Computed Q_{sca} for the sphere with refractive index $n = 1.4$ as a function of the size parameter x. 29

2.6 The expanded view of the scattering efficiency spectrum of Fig. 2.5, centered around x=17. 30

2.7 The real (solid line) and imaginary (dotted line) parts of the a_{19} scattering coefficient in the same range as Fig. 2.6. 31

2.8 The contribution of a_{19} to the scattering efficiency spectrum. The resonance peak of the l mode and the s order are shown as $a_{l,s}$. . 31

2.9 (A)The ray hits the surface of the spherical particle at glancing angle. If $\theta_{\mathrm{in}} > \theta_{\mathrm{c}}$ the totally reflection occurs. (B)If the ray returns to the same position in phase, resonant standing waves grow along the circumference of the sphere. 33

2.10 The resonant light wave propagates along the great circle whose normal direction is inclined at an angle $\pi/2-\theta$ with respect to the z-axis. 34

2.11 The internal intensity distributions in the equatorial plane for (A)TE$_{30,1}$, (B)TE$_{30,2}$ and (C)TE$_{30,3}$ modes of a sphere with $n = 1.4$. The resonant size parameters are shown in the upper side of each figure. 36

2.12 The internal intensity distributions as a function of θ for TE MDRs with $l = 30$ and $m = 1$, 15 and 30. The maximum intensity of each m-mode is located near $\theta = \sin^{-1}(m/l)$. 37

2.13 The angle averaged intensity as a function of the normalized radius r/a for TE MDRs with $l = 60$ and $s = 1$, 2 and 3. The refractive index of the sphere is 1.4. 38

2.14 The resonance curves for the same MDRs and the sphere as in Fig. 2.13as a function of the size parameter, where each x_0 is centered. 39

2.15 the resonance curves for the first order TE MDRs with $l = 30$, 45 and 60 as a function of the size parameter, where x_0 is also centered. The refractive index of the sphere is 1.4. 40

3.1 The restoring force **F** increasing linearly with distance r acts on a particle. 44

3.2 (A) The electrode configuration for the ion trap built of an hyperbolically shaped ring and two hyperbolic caps. These electrode are rotationally symmetric with respect to the z axis. (B) The static quadrupole potential in the ion trap. 45

3.3 The stability diagram of the Mathieu's differential equations for the z (left side) and the r (right side) directions. 47

3.4 The lowest region for stability in the ion trap. 47

3.5 (A) The photographic images of an ion trap employed in this work. (B) The cross-section of four disk electrodes with geometrical dimensions. (C) Equipotential lines around the electrodes when the dc voltage is applied between the two center electrodes and the two end electrodes. 48

3.6 (A) The quasi-quadrupole potential around the center of the ion trap used in this work. (B) The quadrupole potential generated from the hyperbolically shaped electrodes. 50

3.7 Setup scheme of the ion trap. The two middle electrodes are applied ac voltage, whereas the two end electrodes are used to form an additional dc field. 50

3.8 (A) The method of electro-spray ionization (B) The photographic image of the microdroplet levitated in the ion trap. 51

3.9 The distinct scattering light pattern from the spherical microparticle. 52

3.10 Schematic of experimental setup for optical spectroscopy and microscopy of the droplets in the ion trap. 53

3.11 The upper side shows the chamber for housing the ion trap assembly, while the lower side shows the ion trap assembly attached to the top plate. 55

3.12 The electric circuit for the measurement of the pulse width (left side). The temporal spectrum of the SHG radiation (532 nm) of the Q-switched Nd:YAG laser (right side) 56

3.13 The left column is the mercury spectra obtained by using (A) 150, (B) 600 and (C) 1800 groove/mm gratings. For each frame, spectra (a), (b), (c) and (d) are recorded when the slit width is adjusted to 150, 100, 50 and 10 μm, respectively. The right column shows the values of FWHM plotted as a function of the slit width. 57

3.14 Photographic images of the microscope originally developed for obtaining spatial images of radiating microdroplets suspended in the ion trap. The left is the front view, while the right is the side view. 58

3.15 Experimental setup for simultaneously obtaining emission spectra and microscopic images of the microdroplets in the ion trap. . . . 59

3.16 (A)The electric circuit of the synchronous device. (B) Timing relationships of this system. 60

4.1 Emission spectra of Rh6G-doped microdroplet for various pump intensities. Only spectrum (a) was obtained by using the cw laser and, in this case, the power is below the lasing threshold, whereas (b), (c) and (d) were obtained by using the pulsed laser. 65

4.2 Microscopic spatial images of light-emitting microdroplet. Images (A), (B), (C) and (D) were simultaneously obtained with corresponding spectra (a), (b), (c) and (d) in Fig. 4.1, respectively. . . 67

4.3 (A) Schematic image of focusing effect. (B)MDRs with low order number confine light waves near the surface of droplet. Only light waves emerging to the direction of observation can be detected. . 68

4.4 The incident pump beam whose propagation direction and polarization are parallel to the z- and x-axes, respectively. 70

4.5 Microscopic images of a lasing microdroplet. Arrows at the left of each image indicate the direction and polarization of the pump beam, while an arrow at the right indicates the transparent axis of the analyzer. In images (A) and (D), laser emissions due to MDRs dominate at both poles, whereas, in (B) and (D), intensities at both poles are considerably weak. 71

4.6 Emission spectra of the lasing microdroplet. Spectra (A) and (D) were obtained under the same polarization conditions as images (A) and (D) in Fig. 4.5. These images are inserted to each spectrum. Only radiation from TM modes can be detected in spectrum (A) since laser light due to MDRs dominates at both poles and TE modes have no radial components. The peaks corresponding to TM and TE modes are indicated by open and closed circles, respectively 73

4.7 Microscopic images of a microdroplet obtained without an optical filter. The polarization conditions of images (A) and (B) were the same as those of (A) and (B) in Fig. 4.5, but the pump intensity was much weaker than that in the cases of Figs. 4.5and 4.6. The bright spots in (A) are caused by light rays as shown schematically in (C). Note that the x axis is vertical in (A) and (B), while horizontal in (C). 76

4.8 Microscopic images of lasing microdroplets of various dye concentrations. Arrows at the left of each image indicate the direction and polarization of the pump beam, while an arrow at the right indicates the transparent axis of the analyzer. In images (A) - (E), laser emissions due to MDRs dominate at both poles, whereas, in (F), intensities at both poles are considerably weak and lasing from side regions dominates. 79

4.9 Emission spectra of the lasing microdroplet. Spectra (A), (C) and (E) were obtained under the same polarization conditions as images (A), (C) and (E) in Fig. 4.8. As dye concentration decreases from (A) to (E), laser lines shift toward shorter wavelength and the structures of the spectra become more complicated. 81

4.10 Emission spectra (A) - (E) were obtained from the same droplets and under the same polarization conditions as (A) - (E) in Fig. 4.8, correspondingly. 82

4.11 N lasing peaks at wavelength λ_{Ei} $(i = 1, 2, \cdots, N)$ and calculated theoretical resonance position λ_{Ti}. $\triangle_i$ is defined as the difference between λ_{Ti} and λ_{Ei}. 83

4.12 Calculated MDRs mode positions (upper) and the emission spectrum for the droplet of 7×10^{-6} mol/L (lower). 84

4.13 Calculated Q_0's of $l = 135$ - 150 and $s = 5$ modes of MDRs. The parameters of the droplet are $a = 12$ μm and $n = 1.4$, similar to ones of the droplets in the present observations. Closed and open circles refer to resonant positions of TE and TM modes, respectively. 87

5.1 (A) The wave functions Ψ_A and Ψ_B of the two atoms at large separation. (B) The bonding orbital $\Psi_\mathrm{A}+\Psi_\mathrm{B}$. (C) The antibonding orbital $\Psi_\mathrm{A} - \Psi_\mathrm{B}$. 92

5.2 (A) The splitting of the degenerate energy level of the H atoms is schematically drawn. (B) The modes with same resonant frequency split to two coupled modes. 93

5.3 (A) The photon is confined in the photonic molecule. (B) By removing the interaction between the two spheres the photon propagates toward the outer region of the sphere. 94

A.1 The drawings of (A) the middle electrode and (B) the end electrode. 97

A.2 The drawing of the top plate. 98

A.3 The drawing of the sidewall. 98

B.1 Principle of optical trapping. Refraction and reflection at the surface of the particle cause momentum transfer from photon to the particle. The refraction of the ray A leads to the light momentum change $\Delta\mathbf{P_A}$ as shown in the right side. 99

B.2 The apparatus of the laser manipulation system. 100

B.3 (A) Photographs before (a) and after (b) trapping the 13 μm polystyrene spherical particle. The optically levitated particle is denoted by the arrow in (b). (B) The particle in (a) was extremely stable and remained for hours. In (b) through (d) by scanning the laser beam, the particle was moved along the characters "K, U and T". 101

Chapter 1

Introduction

1.1 Historical Remarks

Microstructures, e.g. spherical particles, cylinders and disks, act as high Q resonators in optical regime. The curved surface of a microstructure leads to efficient confinement of light waves. The light waves totally reflect at the surface and propagate along the circumference. If they round in phase, resonant standing waves are produced near the surface. Such resonances are called "morphology dependent resonances (MDRs)" because the resonance frequencies strongly depend on the size parameter x ($= 2\pi a/\lambda$, where a is the radius of microstructure and λ is the light wavelength). The resonant modes are often called "Whispering Gallery Modes (WGMs)". The WGMs are named because of the similarity with acoustic waves traveling around the inside wall of a gallery. Early this century, L. Rayleigh [1] first observed and analyzed the "whispers" propagating around the dome of St. Catherine's cathedral in England. Optical processes associated with MDRs have been studied extensively in recent years [2]. Microstructures exhibit linear and nonlinear optical effects in elastic scattering, Raman scattering, fluorescence and laser emission. In what follows, we describe mainly a historical review of investigations on optical properties related with spherical microparticles.

Early this century, Mie and Debye solved analytically the problem of the elastic scattering of spherical particles. Nowadays this theory is well known as the Mie theory. By using the force of radiation pressure predicted from the Mie theory, Ashkin [3] developed the technique of the optical levitation which suspends a small particle in a given position without mechanical support. Ashkin and Dziedzic also reported an elastic scattering spectrum with many resonant peaks due to MDRs of spherical particles in ref. [4]. These experimental studies have opened the door for the development of laser manipulation systems [5].

Thurn and Kiefer [6] reported the Raman spectra of optically levitated liquid droplets of mixtures of water and glycerol. Peak structure in the Raman spectra due to MDRs lying within O-H stretching spectral region of the mixtures were observed. Snow *et al.* [7] reported stimulated Raman scattering (SRS) from water and ethanol droplets produced by an aerosol generator actuated with a piezoelectric device. They revealed that the input intensity required to achieve the SRS threshold for the droplets is considerably less than that for the liquid in an optical cell. Armstrong and his co-workers [8] reported SRS from droplets in a double-resonance condition where the droplets were in resonance with not only emitted wavelength but also incident laser wavelength. They showed SRS emission occurs at lower incident laser intensities for the double-resonance than that for single (output) resonance conditions.

Peak structures due to MDRs in fluorescence spectra of dye-doped polystyrene spheres were observed by Benner *et al.* [9]. MDRs modify the emission from the microspheres and, in the emission spectra, many peaks are superposed on the well known broadband structure of the dye molecules. Holler *et al.* [10] compared the emission spectrum from a fluorescent droplet with the semiclassical theory of the interaction of MDRs with excited molecules. When atoms or molecules are placed in a microcavity, the fluorescence from them are alternately enhanced or inhibited. The enhancement or inhabitation of the radiation depends on whether or not the radiation frequency coincides with the resonant frequency of the microcavity. This effect has been first predicted by Purcell [11] and is known as cavity quantum electrodynamics (cavity QED) [12]. Cavity QED enhancement of emission rate in microdroplets was reported in refs. [13, 14]. Barnes *et al.* [15] also reported the modification of spontaneous emission rate for oriented molecules in a spherical microcavity where molecular position and transition moment orientation were well defined.

Laser emission from spherical particles were first observed by Garret *et al.* [16] who employed Sm^{2+} doped CaF_2 spherical particles having 1mm radii. More recently several investigators have observed lasing from microspheres as follows. Chang and his co-workers [17, 18] reported lasing action of the dye-doped ethanol droplet stream generated by a piezoelectric aerosol generator and revealed, using microscopic spatial images, that laser emission from individual droplets highlights the droplet surface. Temporal properties of laser emission from dye-doped water and ethanol droplets were investigated by Biswas *et al.* [19]. Gonokami *et al.* [20] reported spectral and temporal responses and spatial profiles of laser emission from dye-doped polystyrene microspheres placed on a glass plate.

MDRs in other geometries, micro-cylinders, -disks and -rings, have also been investigated. Spectra of elastic scattering [21], Raman scattering [22], SRS [23], fluorescence [24] and laser emission [23] from cylinders exhibit intense peaks associated with MDRs. Thin semiconductor microdisk lasers based on MDRs were fabricated by etching techniques and their optical properties were reported in refs. [25, 26]. Kawabe *et al.* [27] observed laser emission from a microring composed of a semiconducting polymer.

A number of applications utilizing MDRs have been proposed by several researchers. MDRs are useful for characterizing microstructures. By comparing observed spectral peak positions of MDRs with results calculated from the Mie theory, the radii of spherical and cylindrical materials are determined with extreme precision [28, 29]. Chang and his co-workers [30, 31] determined evaporation and condensation rates of droplets and the degree of the shape deformation for a slightly deformed droplet. Fluorescence coupled with MDRs is used to detect small number of fluorescent molecules in a microcavity. Whitten *et al.* [32] reported that 12 molecules were detected in glycerol-water microdroplets. The coupling between MDRs of solid spheres and optical fibers were reported in refs.

[33, 34]. The microsphere-fiber system has a potential to realize a narrow band optical filter in dispersive microphotonics. Sbanski *et al.* [35] reported elastic light scattering from single microparticles on a femtosecond time scale and proposed the potential application of the results to optical data communications. Efficient confinements of electromagnetic fields inside microstructures lead to decreased thresholds for lasing. A lot of attention is attracted to such microlasers not only for the fundamental research problems of cavity QED effects but also for application of these effects to thresholdless lasers [36].

1.2 Motivation of the Present Study

In order to obtain fundamental information on optical properties of spherical microlasers, laser actions of dye-doped microdroplets in an ion trap have been investigated. Unlike droplet streams or droplets on substrates as mentioned in the previous section, the single droplets isolated in the ion trap are suspended without mechanically supports. This leads levitated droplets into almost perfect spheres owing to surface tension. The ion trap technique is hence ideally suited to the studies on the spherical microlasers.

We employ droplets composed of liquid glycerol doped with rhodamine 6G (Rh6G) molecules. Rh6G molecules are generally used in conventional dye lasers and their optical properties are well known [37]. Glycerol is employed as the solvent for the much lower vapor presser (0.13 kPa at 122.5 °C) than that of water or ethanol [38]. The reduction rate of a droplet having 13 μm radius is experimentally estimated at 4 nm/min as will be seen in Chap. 4.

For droplets levitated in a ion trap, Arnold and his co-workers [39, 40] reported enhanced energy transfer between donor and acceptor molecules, and polarization effect in fluorescence emission spectra from droplets. These results were obtained from spectroscopic and microscopic experiments. Investigations on the lasing action of a droplet using an ion trap, however, have not been performed. Accordingly we have developed original experimental apparatuses including an ion trap and observation devises for lasing droplets. We have carried out spectroscopic and microscopic experiments to investigate lasing modes coupled with MDRs. In this thesis we describe results and analysis of these experimental studies.

MDRs are characterized by three numbers, s, l and m. These integers distinguish intensity distribution of the resonant mode inside a sphere as will been seen in Chap. 2. On the analogy of quantum mechanics, three integers correspond to the radial, the total angular momentum and the azimuthal quantum numbers. Accordingly the system of a dielectric sphere with MDRs is often called "photonic atom" by analogy with a hydrogen atom. Moreover it is recently reported that the coherent coupling between two adjacent dielectric spheres of almost the same radius are called "photonic molecule" [41]. The authors in [41] proposed to develop new type of photonic devices which can manipulate light waves in micrometer length scale based on photonic molecules. We consider the present study to be a basic research on developing photonic devices, which will be discussed in Chap. 5.

1.3 Outline of the Present Thesis

In Chap. 2, Optical Properties of Spherical Particles, we introduce the Mie theory and discuss MDRs. Section 2.1 describes vector wave functions which are solutions to the vector wave equations derived from the Maxwell equations. In § 2.2 we introduce the Mie theory based on the vector wave functions and discuss elastic scattering of spherical particles. Section 2.3 deals with MDRs in terms of geometric and wave optics.

Chapter 3, Experimental Details, describes the ion trap technique and observation methods of emission from single droplets confined in the ion trap. Section 3.1 deals with the principle of confining charged particles in an ion trap and describes an ion trap originally developed for this work. Section 3.2 presents experimental apparatuses for observations of emission from single droplets levitated in the ion trap.

In Chap. 4, Results and Discussion, the novel phenomena obtained in the present study are described and discussed in detail. Section 4.1 discusses modes of laser emission from levitated microdroplets observed for various pump intensities. Section 4.2 discusses polarization properties of levitated lasing droplets obtained from both emission spectra and microscopic spatial images. Section 4.3 discusses the lasing modes of levitated droplets of various dye concentrations.

In Chap. 5, Conclusion, the summary and the future development of this study are stated. In the latter of the chapter, we propose novel photonic devises based on photonic molecules.

Chapter 2

Optical Properties of Spherical Particles

2.1 Solutions to Vector Wave Equations

We here describe vector spherical functions which is solutions to the vector wave equations in spherical polar coordinate[1] in order to introduce the Mie theory and to discuss optical resonances in spherical particles, i.e., MDRs. We first derive the vector wave equation for electromagnetic fields from the Maxwell equations. Secondly, we show the problem of finding solutions to the vector wave equation can be reduced to the simpler problem of finding solutions to the scalar wave equation.

---

[1] In this chapter we treat vector functions in spherical polar coordinates. In these coordinates the divergence and the rotation of a vector $\mathbf{a} = (a_r, a_\theta, a_\phi)$ are

$$\begin{aligned} \text{div } \mathbf{a} \equiv \nabla \cdot \mathbf{a} &= \frac{1}{r^2 \sin\theta} \left[\sin\theta \frac{\partial}{\partial r} \left(r^2 a_r \right) + r \frac{\partial}{\partial \theta} \left(\sin\theta a_\theta \right) + r \frac{\partial a_\phi}{\partial \phi} \right] , \qquad (2.1.1) \\ \text{rot } \mathbf{a} \equiv \nabla \times \mathbf{a} &= \mathbf{e}_r \frac{1}{r \sin\theta} \left[\frac{\partial}{\partial \theta} \left(a_\phi \sin\theta \right) - \frac{\partial}{\partial \phi} a_\theta \right] \\ &+ \mathbf{e}_\theta \frac{1}{r \sin\theta} \left[\frac{\partial}{\partial \phi} a_r - \sin\theta \frac{\partial}{\partial r} \left(a_\phi r \right) \right] + \mathbf{e}_\phi \frac{1}{r} \left[\frac{\partial}{\partial r} \left(a_\theta r \right) - \frac{\partial}{\partial \theta} a_r \right] , \qquad (2.1.2) \end{aligned}$$

where $\mathbf{e}_r$, $\mathbf{e}_\theta$ and $\mathbf{e}_\phi$ are unit vectors for the r, θ and ϕ directions, respectively, and the Laplacian of a scalar function ψ is

$$\nabla^2 \psi = \frac{1}{r} \frac{\partial}{\partial r} \left(r^2 \frac{\partial \psi}{\partial r} \right) + \frac{1}{r^2 \sin\theta} \frac{\partial}{\partial \theta} \left(\sin\theta \frac{\partial \psi}{\partial \theta} \right) + \frac{1}{r^2 \sin\theta} \frac{\partial^2 \psi}{\partial \phi^2} . \qquad (2.1.3)$$

Thirdly, we construct the vector wave functions corresponding to the electric and magnetic fields from the scalar functions. Finally, we discuss orthogonal relations between the vector wave functions, which play an important role when we determine the expansion coefficients of light waves treated in the Mie theory.

2.1.1 Vector wave equations

The basic laws of electricity and magnetism can be summarized in the set of four equations, known as Maxwell Equations [42];

$$\begin{aligned} \nabla\cdot\mathbf{D} &= \rho\ , && (2.1.4)\\ \nabla\cdot\mathbf{B} &= 0\ , && (2.1.5)\\ \nabla\times\mathbf{E} &= -\frac{\partial\mathbf{B}}{\partial t}\ , && (2.1.6)\\ \nabla\times\mathbf{H} &= \mathbf{j}+\frac{\partial\mathbf{D}}{\partial t}\ , && (2.1.7)\end{aligned}$$

where $\mathbf{E}$ and $\mathbf{H}$ are the electric and the magnetic fields, and ρ and $\mathbf{j}$ are the free charge and current densities, respectively. In linear isotropic materials, the vector fields $\mathbf{D}$ and $\mathbf{B}$ are given by

$$\mathbf{D} = \epsilon\epsilon_0\mathbf{E}\ , \tag{2.1.8}$$

$$\mathbf{B} = \mu\mu_0\mathbf{H}\ , \tag{2.1.9}$$

where ϵ_0 and μ_0 are the permittivity and the permeability of free space, and ϵ and μ, which are complex in general, are the dielectric constant and the magnetic permeability of the medium, respectively. As seen in eqs. (2.1.6) and (2.1.7), in time dependent problems the independence nature of the electric and magnetic fields disappears. Time-varying magnetic fields give rise to electric fields whereas time-varying electric fields to magnetic fields.

The properties of electromagnetic waves involve such an interaction between two fields. We confine the analyses for electromagnetic waves to isotropic and homogeneous materials and to non-conducting materials for simplicity. In the case of non-conducting materials ($\mathbf{j} = 0$) with no free charge ($\rho = 0$), these equations are rewritten in terms of **E** and **B** as follows;

$$\begin{aligned} \nabla \cdot \mathbf{E} &= 0\ , \qquad (2.1.10) \\ \nabla \cdot \mathbf{B} &= 0\ , \qquad (2.1.11) \\ \nabla \times \mathbf{E} &= -\frac{\partial \mathbf{B}}{\partial t}\ , \qquad (2.1.12) \\ \nabla \times \mathbf{B} &= \epsilon\epsilon_0\mu\mu_0\frac{\partial \mathbf{E}}{\partial t}\ . \qquad (2.1.13) \end{aligned}$$

In order to eliminate the magnetic field, we take the rotation of the both sides of eq. (2.1.12);

$$\begin{aligned} \nabla \times (\nabla \times \mathbf{E}) &= -\nabla \times \frac{\partial \mathbf{B}}{\partial t} \qquad (2.1.14) \\ &= -\frac{\partial}{\partial t}\nabla \times \mathbf{B}\ . \end{aligned}$$

By combining this equation with eq. (2.1.13), we obtain;

$$\nabla \times (\nabla \times \mathbf{E}) = -\epsilon\epsilon_0\mu\mu_0\frac{\partial^2 \mathbf{E}}{\partial^2 t}\ . \qquad (2.1.15)$$

If we use a vector formula [43];

$$\nabla \times (\nabla \times \mathbf{a}) = \nabla(\nabla \cdot \mathbf{a}) - \nabla^2\mathbf{a}\ , \qquad (2.1.16)$$

eq. (2.1.15) is replaced by

$$\nabla^2\mathbf{E} = \epsilon\epsilon_0\mu\mu_0\frac{\partial^2 \mathbf{E}}{\partial^2 t}\ , \qquad (2.1.17)$$

because $\nabla \cdot \mathbf{E} = 0$. By applying a similar procedure to the field **B**, we obtain ;

$$\nabla^2\mathbf{B} = \epsilon\epsilon_0\mu\mu_0\frac{\partial^2 \mathbf{B}}{\partial^2 t}\ . \qquad (2.1.18)$$

Eqs. (2.1.17) and (2.1.18) are vector wave equations, and, for real ϵ and μ (no losses), those solutions represent unattenuated electromagnetic waves propagating in any direction. By comparing these equations with a scalar wave equation,

$$\nabla^2\psi = \frac{1}{v^2}\frac{\partial^2 \psi}{\partial^2 t}\ , \qquad (2.1.19)$$

we obtain the propagation velocity of the electromagnetic wave as follows;

$$v = \left(\frac{1}{\epsilon\epsilon_0\mu\mu_0}\right)^{\frac{1}{2}}\ . \qquad (2.1.20)$$

All electromagnetic waves in free space ($\epsilon = \mu = 1$) propagate with the same velocity which is a fundamental constant denoted by the symbol $c \left(= 1/\sqrt{\epsilon_0 \mu_0}\right)$. The phase velocity of the wave propagating in a medium with ϵ and μ being not unity is

$$v = \frac{1}{\sqrt{\epsilon\epsilon_0\mu\mu_0}} = \frac{c}{\sqrt{\epsilon\mu}} = \frac{c}{n} \ , \tag{2.1.21}$$

where the quantity n is the refractive index.

When we consider solutions of the vector wave equations with harmonic time dependence $\exp(-i\omega t)$, the Maxwell equations (2.1.10) through (2.1.13) are rewritten by

$$\nabla \cdot \mathbf{E} = 0 \ , \tag{2.1.22}$$

$$\nabla \cdot \mathbf{B} = 0 \ , \tag{2.1.23}$$

$$\nabla \times \mathbf{E} = i\omega \mathbf{B} \ , \tag{2.1.24}$$

$$\nabla \times \mathbf{B} = -i\frac{\omega}{v^2}\mathbf{E} \ . \tag{2.1.25}$$

As seen these equations, electric and magnetic fields have the following properties; the rotation of the divergence-free electric field is proportional to the magnetic field and the rotation of the magnetic field is proportional to the electric field. Harmonic time dependence also gives us the Helmholtz wave equations for electric and magnetic fields,

$$\nabla^2\mathbf{E} + k^2\mathbf{E} = 0 \ , \tag{2.1.26}$$

$$\nabla^2\mathbf{B} + k^2\mathbf{B} = 0 \ , \tag{2.1.27}$$

where k is wave number and is equal to ω/v. By solving the Helmholtz equations in spherical polar coordinates, we obtain vector spherical wave functions as eigenfunctions of the equations. The eigenvalues of the Helmholtz equations give modes of optical resonances in spherical particles, i.e., MDRs and the eigenfunctions give spatial characteristics of MDRs. In the subsequent subsections, we describe solutions to the Helmholtz equations.

2.1.2 Vector functions satisfying vector wave equations

Elementary solutions to the vector Helmholtz equations is found in ref. [44]. We construct a vector function;

$$\mathbf{M} = \nabla \times (\mathbf{c}\psi) \ , \tag{2.1.28}$$

where $\mathbf{c}$ is an arbitrary vector functions, and ψ is a scalar function and is the solution to the scalar Helmholtz equation, that is,

$$\nabla^2\psi + \lambda_{\mathrm{M}}^2\psi = 0 \ . \tag{2.1.29}$$

The divergence of $\mathbf{M}$ is equal to zero because the divergence of the rotation of any vector function vanishes. If we add together the following two equations;

$$\begin{aligned} \nabla \times (\nabla \times \mathbf{M}) &= \nabla \times [\nabla \times (\mathbf{c}\psi)] \ , & (2.1.30) \\ -\lambda_{\mathrm{M}}^2\mathbf{M} &= -\nabla \times \left(\mathbf{c}\lambda_{\mathrm{M}}^2\psi\right) \ , & (2.1.31) \end{aligned}$$

we obtain

$$\nabla^2\mathbf{M} + \lambda_{\mathrm{M}}^2\mathbf{M} = \nabla \times \left[\mathbf{c}\left(\nabla^2\psi + \lambda_{\mathrm{M}}^2\psi\right)\right] \ . \tag{2.1.32}$$

Since the scalar function ψ is defined as satisfying the scalar wave equations (see eq. (2.1.29)), $\mathbf{M}$ also satisfies the vector wave equation, that is,

$$\nabla^2\mathbf{M} + \lambda_{\mathrm{M}}^2\mathbf{M} = 0 \ . \tag{2.1.33}$$

We construct another vector function from $\mathbf{M}$ as follows;

$$\mathbf{N} = \frac{1}{\lambda_{\mathrm{N}}}\nabla \times \mathbf{M} \ . \tag{2.1.34}$$

Taking the rotation of both sides of eq. (2.1.34) and using the vector formula eq. (2.1.16), we obtain ;

$$\begin{aligned} \nabla \times \mathbf{N} &= \frac{1}{\lambda_{\mathrm{N}}}\nabla(\nabla \times \mathbf{M}) \\ &= \frac{1}{\lambda_{\mathrm{N}}}\nabla(\nabla \cdot \mathbf{M}) - \frac{1}{\lambda_{\mathrm{N}}}\nabla^2\mathbf{M} \ . \end{aligned} \tag{2.1.35}$$

The first term in the right side of the above equation vanishes because $\nabla \cdot \mathbf{M} = 0$, whereas the second term is equal to $(\lambda_{\mathrm{M}}^2/\lambda_{\mathrm{N}})\mathbf{M}$ as seen in eq. (2.1.33). Accordingly, we get $\nabla \times \mathbf{N} = (\lambda_{\mathrm{M}}^2/\lambda_{\mathrm{N}})\mathbf{M}$. Taking the rotation of both sides of this equation again, we fined that $\mathbf{N}$ also satisfies the vector wave equations;

$$\nabla^2 \mathbf{N} + \lambda_{\mathrm{M}}^2 \mathbf{N} = 0 \ . \tag{2.1.36}$$

The divergence and the rotation of the vector functions $\mathbf{M}$ and $\mathbf{N}$ are as follows;

$$\nabla \cdot \mathbf{M} = 0 \ , \tag{2.1.37}$$

$$\nabla \cdot \mathbf{N} = 0 \ , \tag{2.1.38}$$

$$\nabla \times \mathbf{M} = \lambda_{\mathrm{N}} \mathbf{N} \ , \tag{2.1.39}$$

$$\nabla \times \mathbf{N} = \frac{\lambda_{\mathrm{M}}^2}{\lambda_{\mathrm{N}}} \mathbf{M} \ . \tag{2.1.40}$$

Remarkably, these equations are analogous to the Maxwell equations (2.1.22) through (2.1.25). The vector functions $\mathbf{M}$ and $\mathbf{N}$, therefore, not only satisfy the vector wave equation but also have the required properties of electromagnetic fields. If the scalar function ψ satisfying the scalar wave equation is found, the vector functions $\mathbf{M}$ and $\mathbf{N}$ will be constructed from eqs. (2.1.28) and (2.1.34).

In the next subsection, we will find the solution to the scalar wave equation in order to construct $\mathbf{M}$ and $\mathbf{N}$. The scalar wave equation should be solved in spherical polar coordinates r, θ and ϕ as shown in Fig. 2.1, because we are interested in the resonant modes of electromagnetic fields in spherical particles.

2.1.3 Solutions to the scalar wave equation in spherical polar coordinates

The Helmholtz equation in spherical polar coordinates is

$$\frac{1}{r}\frac{\partial}{\partial r}\left(r^2 \frac{\partial \psi}{\partial r}\right) + \frac{1}{r^2 \sin\theta}\frac{\partial}{\partial \theta}\left(\sin\theta \frac{\partial \psi}{\partial \theta}\right) + \frac{1}{r^2 \sin\theta}\frac{\partial^2 \psi}{\partial \phi^2} + k^2 \psi = 0 \ . \tag{2.1.41}$$

The simplest way of treating a partial differential equation such as eq. (2.1.41) is to split it into a set of ordinary differential equations. When we assume

$$\psi(r, \theta, \phi) = R(r)\Theta(\theta)\Phi(\phi) \tag{2.1.42}$$

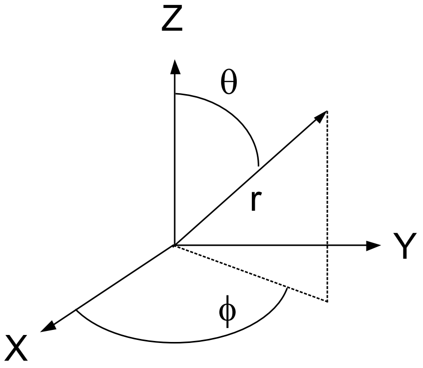

Fig. 2.1: Spherical polar coordinates.

and put it into eq. (2.1.41), we obtain three differential equations as follows [45];

$$\frac{d^2\Phi}{d\phi^2} + m^2\Phi = 0 \ , \tag{2.1.43}$$

$$\frac{1}{\sin\theta}\frac{d}{d\theta}\left(\sin\theta\frac{d\Theta}{d\theta}\right) + \left[l(l+1) - \frac{m^2}{\sin^2\theta}\right]\Theta = 0 \ , \tag{2.1.44}$$

$$\frac{d}{dr}\left(r^2\frac{dR}{dr}\right) + \left[k^2r^2 - l(l+1)\right]R = 0 \ , \tag{2.1.45}$$

where the separation constants m and l are integers and determined by conditions that ψ must satisfy.

Eq. (3.1.14) has the two linearly independent solutions;

$$\Phi_e = \cos m\phi \ , \tag{2.1.46}$$

$$\Phi_o = \sin m\phi \ , \tag{2.1.47}$$

where subscripts e and o denote even and odd as the same notation in ref. [44]. The solutions to eq. (2.1.44) are the associated Legendre functions [46],

$$\Theta = P_l^m(\cos\theta) \ . \tag{2.1.48}$$

The associated Legendre functions satisfy the following recurrence relations;

$$(l-m+1)P_{l+1}^m = \left[(2l+1)\cos\theta P_l^m - (l+m)P_{l-1}^m\right] \ , \tag{2.1.49}$$

$$\sin\theta\frac{dP_l^m}{d\cos\theta} = \frac{1}{2}P_l^{m+1} - \frac{1}{2}(l+m)(l-m+1)P_l^{m-1} \ . \tag{2.1.50}$$

These relations are useful for computing the angular distribution pattern of scattered light waves from a spherical particle. The first few associated Legendre functions are listed in Table I.

Although the radial equation (2.1.45) is not the Bessel equation, with substituting

$$R(\rho) = \frac{Z(\rho)}{\sqrt{\rho}} \ , \tag{2.1.51}$$

where dimensionless variables ρ is equal to kr, we obtain the Bessel equation [47];

$$\rho \frac{d}{d\rho}\left(\rho \frac{dZ}{d\rho}\right) + \left[\rho^2 - \left(l + \frac{1}{2}\right)^2\right] Z = 0 \ . \tag{2.1.52}$$

Accordingly, Z is a Bessel function of order $l + \frac{1}{2}$ (l is an integer). The solutions to eq. (2.1.45), therefore, are

$$R(\rho) = z_l(\rho) = \sqrt{\frac{\pi}{2\rho}} Z_{l+\frac{1}{2}}(\rho) \ , \tag{2.1.53}$$

where the constant factor $\sqrt{\pi/2}$ is introduced for convenience. The functions $z_l(\rho)$ are known as the spherical Bessel functions. They satisfy the following recurrence

Table I: The first few associated Legendre functions.

$$\begin{aligned}
P_1^1(\cos\theta) &= \sin\theta \\
P_2^1(\cos\theta) &= 3\cos\theta\sin\theta \\
P_2^2(\cos\theta) &= 3\sin^2\theta \\
P_3^1(\cos\theta) &= \tfrac{3}{2}(5\cos^2\theta - 1)\sin\theta \\
P_3^2(\cos\theta) &= 15\cos\theta\sin^2\theta \\
P_3^3(\cos\theta) &= 15\sin^3\theta \\
P_4^1(\cos\theta) &= \tfrac{5}{2}(7\cos^3\theta - 3\cos\theta)\sin\theta \\
P_4^2(\cos\theta) &= \tfrac{15}{2}(7\cos^2\theta - 1)\sin^2\theta \\
P_4^3(\cos\theta) &= 105\cos\theta\sin^3\theta \\
P_4^4(\cos\theta) &= 105\sin^4\theta
\end{aligned}$$

relations;

$$\frac{2l+1}{\rho}z_l(\rho) = z_{l-1}(\rho) + z_{l+1}(\rho) \ , \tag{2.1.54}$$

$$(2l+1)\frac{d}{d\rho}z_l(\rho) = l z_{l-1}(\rho) - (l+1)z_{l+1}(\rho) \ . \tag{2.1.55}$$

These relations are useful for computing scattering coefficients of spherical particles and spectral resonant positions of MDRs.

There are the following two linearly independent Bessel functions: one is the first kind and the other is the second kind known as the Neumann functions;

$$j_l(\rho) = \sqrt{\frac{\pi}{2\rho}}J_{l+\frac{1}{2}}(\rho) \ , \tag{2.1.56}$$

$$n_l(\rho) = \sqrt{\frac{\pi}{2\rho}}N_{l+\frac{1}{2}}(\rho) \ . \tag{2.1.57}$$

Using the Bessel functions of the first two orders listed in Table II, higher order functions and their differential functions are generated because both of these functions satisfy the recurrence relations (2.1.54) and (2.1.55). Figure 2.2 shows $j_l(\rho)$ and $n_l(\rho)$ of the first four orders. The functions of the second and third orders are computed by using the recurrence relations (2.1.54). Remarkably, $n_l(\rho)$ becomes infinite as ρ approaches the origin although $j_l(\rho)$ converges to finite values at the origin. This leads us to choose not $n_l(\rho)$ but $j_l(\rho)$ as the radial functions of electromagnetic fields inside the sphere when we discuss the Mie scattering and MDRs.

The spherical Bessel functions of the third kind, called the spherical Hankel

Table II: The first two orders Bessel functions of the first and second kind.

first kind	second kind
$j_0 = \sin\rho/\rho$	$n_0 = -\cos\rho/\rho$
$j_1 = \sin\rho/\rho^2 - \cos\rho/\rho$	$n_1 = \cos\rho/\rho^2 - \sin\rho/\rho$

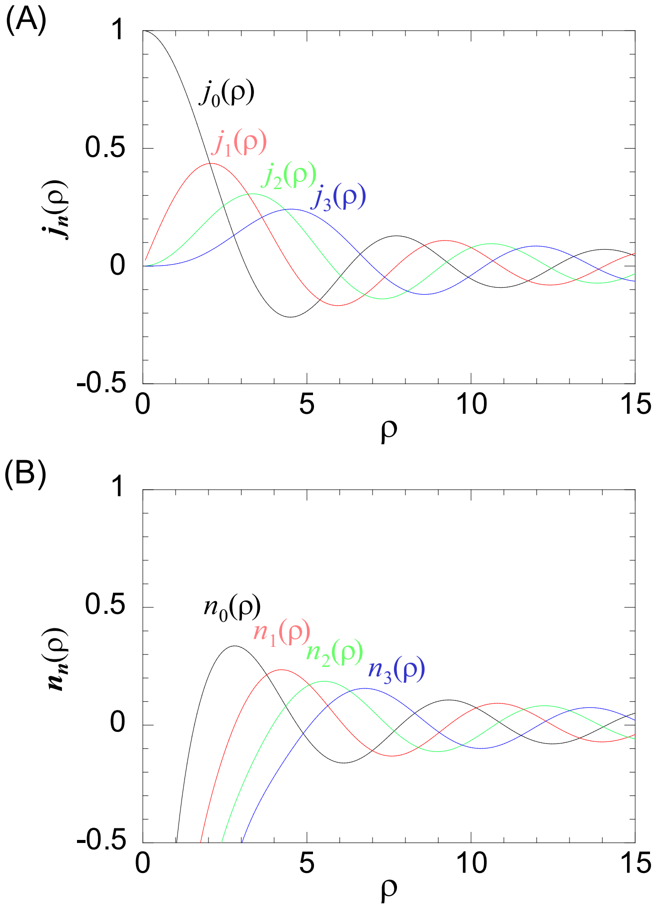

Fig. 2.2: (A)Spherical Bessel functions of the first kind. (B)Spherical Bessel functions of the second kind (spherical Neumann functions).

functions, are defined as the linear combination of $j_l(\rho)$ and $n_l(\rho)$;

$$h_l^{(1)}(\rho) = j_l(\rho) + in_l(\rho) , \tag{2.1.58}$$

$$h_l^{(2)}(\rho) = j_l(\rho) - in_l(\rho) , \tag{2.1.59}$$

and are also the solution to eq. (2.1.45). The spherical Hankel functions are asymptotically given by

$$h_l^{(1)}(\rho) \sim \frac{(-i)^l e^{i\rho}}{i\rho} , \tag{2.1.60}$$

$$h_l^{(2)}(\rho) \sim -\frac{i^l e^{-i\rho}}{i\rho} . \tag{2.1.61}$$

When these functions are combined with time dependence $\exp(-i\omega t)$, eq. (2.1.60) represents outgoing spherical waves whereas eq. (2.1.61) corresponds to incoming spherical waves. Therefore $h_l^{(1)}(\rho)$ is used as radial functions of electromagnetic fields when we consider the outgoing waves scattered by a spherical particle,.

We now have the elementary solutions to the scalar wave equation in spherical polar coordinate;

$$\begin{aligned} \psi_{eml} &= \cos m\phi P_l^m(\cos\theta) z_l(\rho) \ , && (2.1.62) \\ \psi_{oml} &= \sin m\phi P_l^m(\cos\theta) z_l(\rho) \ , && (2.1.63) \end{aligned}$$

where $z_l(\rho)$ is one of the four spherical Bessel functions $j_l(\rho)$, $n_l(\rho)$, $h_l^{(1)}(\rho)$ and $h_l^{(2)}(\rho)$, which is selected appropriate by according to physical conditions. A general solution is expanded as an infinite series of the functions (2.1.62) and (2.1.63). In the following subsection we generate the vector spherical functions $\mathbf{M}$ and $\mathbf{N}$ by using ψ_{eml} and ψ_{oml}.

2.1.4 Vector spherical functions

We construct the vector functions $\mathbf{M}$ and $\mathbf{N}$ based on the relations of $\mathbf{M} = \nabla \times (\mathbf{c}\psi)$ and $\mathbf{N} = \frac{1}{\lambda_{\mathrm{N}}} \nabla \times \mathbf{M}$, where ψ is the solution to the scalar wave equation as mentioned in the previous subsection. The radial vector $\mathbf{r}$ is elected as the arbitrary vector $\mathbf{c}$ in our treatment. Accordingly, the vector functions $\mathbf{M}$ is rewritten as

$$\mathbf{M} = \nabla \times (\mathbf{r}\psi) \ . \tag{2.1.64}$$

It is to be noted that $\mathbf{M}$ is everywhere tangential to the r direction because $\mathbf{r} \cdot \mathbf{M} = 0$. When electric fields are proportional to $\mathbf{M}$, the fields are called transverse electric or TE modes which have no radial components of the electric fields. On the other hand, when magnetic fields are proportional to $\mathbf{M}$, the fields are called transverse magnetic or TM modes which have no radial components of the magnetic fields. Electric fields corresponding to TM modes are given as the rotation of $\mathbf{M}$, that is, $\mathbf{N}$.

Four vector spherical functions generated by ψ_{eml} and ψ_{oml} are

$$\begin{aligned}
\mathbf{M}_{eml} &= \nabla \times (\mathbf{r}\psi_{elm}) \ , && (2.1.65)\\
\mathbf{M}_{oml} &= \nabla \times (\mathbf{r}\psi_{olm}) \ , && (2.1.66)\\
\mathbf{N}_{eml} &= \frac{1}{\lambda_N}\nabla \times \mathbf{M}_{eml} \ , && (2.1.67)\\
\mathbf{N}_{oml} &= \frac{1}{\lambda_N}\nabla \times \mathbf{M}_{oml} \ . && (2.1.68)
\end{aligned}$$

With unit vectors $\mathbf{e}_r$, $\mathbf{e}_\theta$ and $\mathbf{e}_\phi$ for the r, θ and ϕ directions, these functions are written in component form as follows;

$$\begin{aligned}
\mathbf{M}_{eml} &= -m \sin m\phi \frac{P_l^m(\cos\theta)}{\sin\theta} z_l(\rho)\,\mathbf{e}_\theta \\
&\quad - \cos m\phi \frac{dP_l^m(\cos\theta)}{d\theta} z_l(\rho)\,\mathbf{e}_\phi \ , && (2.1.69)\\
\mathbf{M}_{oml} &= m \cos m\phi \frac{P_l^m(\cos\theta)}{\sin\theta} z_l(\rho)\,\mathbf{e}_\theta \\
&\quad - \sin m\phi \frac{dP_l^m(\cos\theta)}{d\theta} z_l(\rho)\,\mathbf{e}_\phi \ , && (2.1.70)\\
\lambda_{\mathrm{N}}\mathbf{N}_{eml} &= \frac{z_l(\rho)}{\rho} \cos m\phi \ l(l+1) P_l^m(\cos\theta)\,\mathbf{e}_r \\
&\quad + \cos m\phi \frac{dP_l^m(\cos\theta)}{d\theta} \frac{1}{\rho}\frac{d}{d\rho}\left[\rho z_l(\rho)\right]\mathbf{e}_\theta \\
&\quad - m \sin m\phi \frac{P_l^m(\cos\theta)}{\sin\theta} \frac{1}{\rho}\frac{d}{d\rho}\left[\rho z_l(\rho)\right]\mathbf{e}_\phi \ , && (2.1.71)\\
\lambda_{\mathrm{N}}\mathbf{N}_{oml} &= \frac{z_l(\rho)}{\rho} \sin m\phi \ l(l+1) P_l^m(\cos\theta)\,\mathbf{e}_r \\
&\quad + \sin m\phi \frac{dP_l^m(\cos\theta)}{d\theta} \frac{1}{\rho}\frac{d}{d\rho}\left[\rho z_l(\rho)\right]\mathbf{e}_\theta \\
&\quad + m \cos m\phi \frac{P_l^m(\cos\theta)}{\sin\theta} \frac{1}{\rho}\frac{d}{d\rho}\left[\rho z_l(\rho)\right]\mathbf{e}_\phi \ . && (2.1.72)
\end{aligned}$$

A general solution to the vector wave equations is expanded as an infinite series of the functions (2.1.69) through (2.1.72).

2.1.5 Orthogonal relations of vector wave functions

In this subsection we discuss orthogonal relations between four vector wave functions derived in the previous subsection. These relations play an important role when we determine the expansion coefficients of light waves treated in the Mie theory.

Because $\sin m\phi$ is orthogonal to $\cos m'\phi$;

$$\int_0^{2\pi} \sin m\phi \ \cos m'\phi \ d\phi = 0 \ , \tag{2.1.73}$$

$\mathbf{M}_{em'l'}$ and $\mathbf{M}_{oml}$ are the orthogonal set of functions, that is,

$$\int_0^{2\pi} \int_0^{\pi} \mathbf{M}_{em'l'} \cdot \mathbf{M}_{oml} \sin\theta d\theta d\phi = 0 \ , \tag{2.1.74}$$

for all m, l, m' and l'. Similarly, ($\mathbf{N}_{em'l'}$, $\mathbf{N}_{oml}$), ($\mathbf{M}_{om'l'}$, $\mathbf{N}_{oml}$) and ($\mathbf{M}_{em'l'}$, $\mathbf{N}_{eml}$) sets are also orthogonal. Orthogonal relations between $\cos m\phi$ and $\cos m'\phi$ and between $\sin m\phi$ and $\sin m'\phi$;

$$\int_0^{2\pi} \cos m\phi \ \cos m'\phi \ d\phi = 0 \ , \tag{2.1.75}$$

$$\int_0^{2\pi} \sin m\phi \ \sin m'\phi \ d\phi = 0 \ , \tag{2.1.76}$$

except when $m = m'$, imply any two vector wave functions of different order m are orthogonal.

We next consider orthogonal relations of ($\mathbf{M}_{eml}$, $\mathbf{N}_{oml}$) and ($\mathbf{M}_{oml}$, $\mathbf{N}_{eml}$). In order to show these orthogonalities we must consider the following integral for all l and l';

$$\begin{aligned} & \int_0^{\pi} \left[\frac{P_l^m(\cos\theta)}{\sin\theta} \frac{dP_{l'}^m(\cos\theta)}{d\theta} + \frac{P_{l'}^m(\cos\theta)}{\sin\theta} \frac{dP_l^m(\cos\theta)}{d\theta} \right] \sin\theta d\theta \\ = & \int_{\theta=0}^{\theta=\pi} \left[P_l^m(\cos\theta) \frac{dP_{l'}^m(\cos\theta)}{d(\cos\theta)} + P_{l'}^m(\cos\theta) \frac{dP_l^m(\cos\theta)}{d(\cos\theta)} \right] d(\cos\theta) \\ = & \left[P_l^m(\cos\theta) P_{l'}^m(\cos\theta) \right]_{\theta=0}^{\theta=\pi} \ . \end{aligned} \tag{2.1.77}$$

By using the fact that $P_l^m(\cos\theta)$ is related to the mth derivative of the Legendre polynomial $P_l(\cos\theta)$ with the same order l;

$$P_l^m(\cos\theta) = \sin\theta \frac{d^m P_l(\cos\theta)}{d(\cos\theta)^m}, \tag{2.1.78}$$

the integral (2.1.77) vanishes because $\sin 0 = \sin\pi = 0$. ($\mathbf{M}_{eml}$, $\mathbf{N}_{oml}$) and ($\mathbf{M}_{oml}$, $\mathbf{N}_{eml}$), therefore, are orthogonal for all m and l and l' except when $l = l'$.

Finally, in order to proof the remaining orthogonal relations, $(\mathbf{M}_{eml}, \mathbf{M}_{eml'})$, $(\mathbf{M}_{oml}, \mathbf{M}_{oml'})$, $(\mathbf{N}_{eml}, \mathbf{N}_{eml'})$ and $(\mathbf{N}_{oml}, \mathbf{N}_{oml'})$, we show the following equation;

$$\int_0^\pi \left[m^2 \frac{P_l^m(\cos\theta)\, P_{l'}^m(\cos\theta)}{\sin^2\theta} + \frac{dP_l^m(\cos\theta)}{d\theta}\frac{dP_{l'}^m(\cos\theta)}{d\theta} \right] \sin\theta d\theta = 0 \; . \tag{2.1.79}$$

We recall both $P_l^m(\cos\theta)$ and $P_{l'}^m(\cos\theta)$ satisfy eq. (2.1.44);

$$\frac{1}{\sin\theta}\frac{d}{d\theta}\left(\sin\theta \frac{dP_l^m(\cos\theta)}{d\theta}\right) + \left[l(l+1) - \frac{m^2}{\sin^2\theta} \right] P_l^m(\cos\theta) = 0 \; , \tag{2.1.80}$$

$$\frac{1}{\sin\theta}\frac{d}{d\theta}\left(\sin\theta \frac{dP_{l'}^m(\cos\theta)}{d\theta}\right) + \left[l(l+1) - \frac{m^2}{\sin^2\theta} \right] P_{l'}^m(\cos\theta) = 0 \; . \tag{2.1.81}$$

By multiplying eq. (2.1.80) by $P_{l'}^m(\cos\theta)$ and eq. (2.1.81) by $P_l^m(\cos\theta)$, and adding each other, we get the following equation;

$$\begin{aligned} & \left[m^2 \frac{P_l^m(\cos\theta)\, P_{l'}^m(\cos\theta)}{\sin^2\theta} + \frac{dP_l^m(\cos\theta)}{d\theta}\frac{dP_{l'}^m(\cos\theta)}{d\theta} \right] \sin\theta \\ = \; & l(l+1) P_l^m(\cos\theta)\, P_{l'}^m(\cos\theta) \sin\theta \\ + \; & \frac{1}{2}\frac{d}{d\theta}\left[\sin\theta \frac{dP_l^m(\cos\theta)}{d\theta} P_{l'}^m(\cos\theta) + \sin\theta \frac{dP_{l'}^m(\cos\theta)}{d\theta} P_l^m(\cos\theta) \right] \end{aligned} \tag{2.1.82}$$

From the recurrence relations (2.1.50) and the orthogonality relations of $P_l^m(\cos\theta)$, the integral of the right side of eq. (2.1.82) is equal to zero. Therefore eq. (2.1.79) is obtained and orthogonal relations of the $(\mathbf{M}_{eml}, \mathbf{M}_{eml'})$, $(\mathbf{M}_{oml}, \mathbf{M}_{oml'})$, $(\mathbf{N}_{eml}, \mathbf{N}_{eml'})$ and $(\mathbf{N}_{oml}, \mathbf{N}_{oml'})$ sets are proved.

Since we now get elementary solutions to the vector wave equations in spherical polar coordinates and the orthogonal relations of all the vector wave functions, we will introduce, in subsequent two sections, the Mie theory and discuses MDRs based on these functions.

2.2 The Mie Theory

The Mie theory is a rigorous scattering and absorption theory for spheres with arbitrary radii. In this theory we consider three light waves as shown in Fig. 2.3; the linearly polarized incident plane wave, the spherical wave inside the sphere and the spherical wave scattered by the sphere. In order to simplify the notation

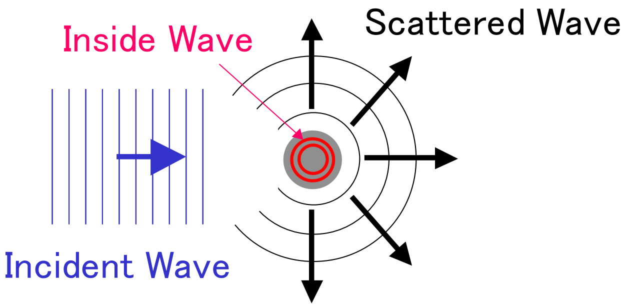

Fig. 2.3: Three light waves; the linearly polarized incident plane wave, the spherical wave inside the sphere and the spherical wave scattered by the sphere.

we assume the outside medium is vacuum, and the material of the sphere with a radius a has an arbitrary refractive index n. In the following subsection, such waves will be expanded as an infinite series in the vector spherical functions derived in previous section. In subsequent subsection, we will derive the expansion coefficients based on Maxwell's boundary conditions. In final subsection, we will discuss the scattering efficiency written by the expansion coefficients.

2.2.1 Expansion of an incident, an inside and a scattered waves in vector wave functions

We assume an incident plane wave propagates along the z-axis in free space and it polarization is parallel to the x-axes as shown in Fig. 2.4. Electric fields $\mathbf{E}_{\text{inc}}$ of this light wave are written expect for time dependence $\exp(-i\omega t)$;

$$\mathbf{E}_{\text{inc}} = E_0 e^{ikz} \mathbf{e}_x \ . \tag{2.2.1}$$

Here $\mathbf{e}_x$ is the unit vector in the x direction and k $(= 2\pi/\lambda$, where λ is the wavelength of the light) is the wave number of the light wave. In spherical polar coordinate, eq. (2.2.1) is replaced by

$$\mathbf{E}_{\text{inc}} = E_0 e^{i\rho\cos\theta} (\sin\theta\cos\phi\mathbf{e}_r + \cos\theta\cos\phi\mathbf{e}_\theta - \sin\phi\mathbf{e}_\phi) \ , \tag{2.2.2}$$

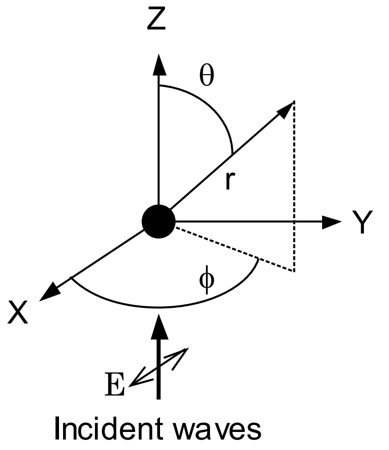

Fig. 2.4: The incident plane wave whose propagation direction and polarization are parallel to the z- and x-axes, respectively.

where $\rho = kr$. We expand $\mathbf{E}_{\text{inc}}$ in vector wave functions as follows;

$$\mathbf{E}_{\text{inc}} = \sum_{m=0}^{\infty}\sum_{l=m}^{\infty}\left(B_{eml}\mathbf{M}_{eml} + B_{oml}\mathbf{M}_{oml} + A_{eml}\mathbf{N}_{eml} + A_{oml}\mathbf{N}_{oml}\right) \;, \tag{2.2.3}$$

where B_{eml}, B_{oml}, A_{eml} and A_{oml} are expansion coefficients. The orthogonality of all the vector wave equations as mentioned in the previous section implies the expansion coefficients are of form;

$$B_{eml} = \frac{\int_0^{2\pi}\int_0^{\pi}\mathbf{E}_{\text{inc}}\cdot\mathbf{M}_{eml}\sin\theta d\theta d\phi}{\int_0^{2\pi}\int_0^{\pi}|\mathbf{M}_{eml}|^2\sin\theta d\theta d\phi} \;, \tag{2.2.4}$$

with similar expressions for the remaining coefficients. B_{eml} and A_{oml} are equal to zero because of the orthogonality of the sine and cosine and, moreover, B_{oml} and A_{eml} also vanish for the same reason except when $m = 1$. Therefore, the expansion for $\mathbf{E}_{\text{inc}}$ is reduced as follows;

$$\mathbf{E}_{\text{inc}} = \sum_{l=1}^{\infty}\left(B_{o1l}\mathbf{M}_{o1l}^{(1)} + A_{e1l}\mathbf{N}_{e1l}^{(1)}\right) \;, \tag{2.2.5}$$

where the superscript (1) is appended to the vector wave functions for the following reason. Because the incident wave is finite at the origin, the Bessel function of the first kind $j_l(\rho)$ should be adopted as the radial function: we reject $n_l(\rho)$ because of its divergent bihavior at the origin as seen in Fig. 2.2. The superscript (1) represents the Bessel function of the first kind is adopted as radial dependence of the vector wave functions.

The integral in the denominator of the expression for B_{o1l} is as follows;

$$\begin{aligned}
&j_l(\rho)^2 \int_0^{2\pi} \int_0^{\pi} \left[\cos^2\phi \frac{\left(P_l^1(\cos\theta)\right)^2}{\sin^2\theta} + \sin^2\phi \left(\frac{dP_l^1(\cos\theta)}{d\theta} \right)^2 \right] \sin\theta d\theta d\phi \\
= \;& j_l(\rho)^2 \pi \int_0^{\pi} \left[\frac{\left(P_l^1(\cos\theta)\right)^2}{\sin^2\theta} + \left(\frac{dP_l^1(\cos\theta)}{d\theta} \right)^2 \right] \sin\theta d\theta \; . \qquad (2.2.6)
\end{aligned}$$

The integral (2.2.6) can be evaluated from eq. (2.1.82) and the orthogonality integral for the associated Legendre functions, and given by

$$2 j_l(\rho)^2 \pi \frac{l^2(l+1)^2}{2l+1} \; . \qquad (2.2.7)$$

On the other hand, the integral in the numerator is as follows;

$$\begin{aligned}
&E_0 j_l(\rho) \int_0^{2\pi} \int_0^{\pi} \left[\cos^2\phi \cos\theta \frac{P_l^1(\cos\theta)}{\sin\theta} + \sin^2\phi \frac{dP_l^1(\cos\theta)}{d\theta} \right] e^{i\rho\cos\theta} \sin\theta d\theta d\phi \\
= \;& E_0 j_l(\rho) \pi \int_0^{\pi} \left[\cos\theta P_l^1(\cos\theta) + \sin\theta \frac{dP_l^1(\cos\theta)}{d\theta} \right] e^{i\rho\cos\theta} d\theta \\
= \;& E_0 j_l(\rho) \pi \int_0^{\pi} \frac{d}{d\theta} \left[\sin\theta P_l^1(\cos\theta) \right] e^{i\rho\cos\theta} d\theta \; . \qquad (2.2.8)
\end{aligned}$$

From eq. (2.1.78) , we get

$$\begin{aligned}
P_l^1(\cos\theta) &= \sin\theta \frac{dP_l(\cos\theta)}{d(\cos\theta)} \\
&= -\frac{dP_l(\cos\theta)}{d\theta} \; . \qquad (2.2.9)
\end{aligned}$$

Because the Legendre polynomials $P_l(\cos\theta)$ satisfy eq. (2.1.44) with $m = 0$,

$$\frac{d}{d\theta} \left(\sin\theta \frac{dP_l(\cos\theta)}{d\theta} \right) = -l(l+1) P_l(\cos\theta) \sin\theta \; . \qquad (2.2.10)$$

Accordingly, the integral (2.2.8) is replaced by

$$E_0 j_l(\rho) \pi l(l+1) \int_0^{\pi} \sin\theta P_l(\cos\theta) e^{i\rho\cos\theta} d\theta \; . \qquad (2.2.11)$$

This integral is evaluated from the following relation between the Legendre polynomials and the Bessel functions of the first kind [48];

$$j_l(\rho) = \frac{i^{-l}}{2} \int_0^{\pi} \sin\theta P_l(\cos\theta) e^{i\rho\cos\theta} d\theta \; . \qquad (2.2.12)$$

By putting this relation into (2.2.11), the integral in the numerator is given by

$$2i^l E_0 j_l(\rho)^2 \pi l(l+1) \ . \tag{2.2.13}$$

From (2.2.7) and (2.2.13), we obtain the expansion coefficients

$$B_{o1l} = i^l E_0 \frac{2l+1}{l(l+1)} \ . \tag{2.2.14}$$

The derivation of the expansion coefficients A_{e1l} is more complicated than that of B_{o1l}. In order to evaluate the numerator in A_{e1l}, we first treat the integral

$$\begin{aligned} & \int_0^\pi P_l^1(\cos\theta)\sin\theta e^{i\rho\cos\theta}\sin\theta d\theta \\ = & -\frac{1}{i\rho}\int_0^\pi P_l^1(\cos\theta)\sin\theta\left(\frac{d}{d\theta}e^{i\rho\cos\theta}\right)d\theta \ , \end{aligned} \tag{2.2.15}$$

which is integrated by parts and is replaced by

$$-\frac{1}{i\rho}\left[P_l^1(\cos\theta)\sin\theta e^{i\rho\cos\theta}\right]_0^\pi + \frac{1}{i\rho}\int_0^\pi \frac{d}{d\theta}\left[\sin\theta P_l^1(\cos\theta)\right]e^{i\rho\cos\theta}d\theta \ . \tag{2.2.16}$$

It is to be noted that the first term is equal to zero and the second term is the same as eq. (2.2.8). Accordingly, the integral (2.2.15) yields

$$\frac{2l(l+1)j_l(\rho)i^l}{i\rho} \ . \tag{2.2.17}$$

Secondly, we treat the integral

$$\int_0^\pi \left(\cos\theta\frac{dP_l^1(\cos\theta)}{d\theta} + \frac{P_l^1(\cos\theta)}{\sin\theta}\right)e^{i\rho\cos\theta}\sin\theta d\theta \ . \tag{2.2.18}$$

If we multiply eq. (2.2.12) by ρ and differentiate it with respect to ρ, we get the following relation;

$$\frac{d\rho j_l(\rho)}{d\rho} = \frac{i^{-l}}{2}\int_0^\pi \left[\sin\theta P_l(\cos\theta) + i\rho\cos\theta\sin\theta P_l(\cos\theta)\right]e^{i\rho\cos\theta}d\theta \ . \tag{2.2.19}$$

After a little algebra for this relation and eq.(2.2.10), we obtain

$$A_{e1l} = -i^{l+1}E_0\frac{2l+1}{l(l+1)} \ . \tag{2.2.20}$$

From eqs. (2.2.14) and (2.2.20), the expantion of the electric field $\mathbf{E}_{\mathrm{inc}}$ of the plane wave in vector wave functions is given by

$$\mathbf{E}_{\mathrm{inc}} = E_0\sum_{l=1}^{\infty} i^l \frac{2l+1}{l(l+1)}\left(\mathbf{M}_{o1l}^{(1)} - i\mathbf{N}_{e1l}^{(1)}\right) \ . \tag{2.2.21}$$

The corresponding $\mathbf{H}_{\mathrm{inc}}$ is obtained from the rotation of $\mathbf{E}_{\mathrm{inc}}$;

$$\mathbf{H}_{\mathrm{inc}} = \frac{-k}{\omega\mu_0} E_0 \sum_{l=1}^{\infty} i^l \frac{2l+1}{l(l+1)} \left(\mathbf{M}^{(1)}_{e1l} + i\mathbf{N}^{(1)}_{o1l} \right) \ . \tag{2.2.22}$$

We also expand the electromagnetic field inside the sphere of radius a, ($\mathbf{E}_{\mathrm{ins}}$, $\mathbf{H}_{\mathrm{ins}}$), and the scattered field, ($\mathbf{E}_{\mathrm{sca}}$, $\mathbf{H}_{\mathrm{sca}}$). At the boundary between the sphere and the surrounding medium, i.e., $r = a$, we impose the following conditions;

$$(\mathbf{E}_{\mathrm{inc}} + \mathbf{E}_{\mathrm{sca}} - \mathbf{E}_{\mathrm{ins}}) \times \mathbf{e}_r = (\mathbf{H}_{\mathrm{inc}} + \mathbf{H}_{\mathrm{sca}} - \mathbf{H}_{\mathrm{ins}}) \times \mathbf{e}_r = 0 \ , \tag{2.2.23}$$

based on Maxwell's boundary conditions [49]. Because of these boundary conditions, the orthogonality of the vector wave functions and the form of the expansion of ($\mathbf{E}_{\mathrm{inc}}$, $\mathbf{H}_{\mathrm{inc}}$), the coefficients in the expansions of ($\mathbf{E}_{\mathrm{ins}}$, $\mathbf{H}_{\mathrm{ins}}$) and ($\mathbf{E}_{\mathrm{sca}}$, $\mathbf{H}_{\mathrm{sca}}$) vanish except for $m = 1$.

For the internal fields the Bessel functions of the first kind $j_l(k_1 r)$, where $k_1 (= nk)$ is the wave number in the sphere, are adopted as the radial function just as the incident wave because the inside wave should be finite at the origin. For the scattered fields, on the other hand, when we consider the outgoing scattered waves, the Bessel functions of the third kind $h^{(1)}_l(\rho)$ are used as radial functions of electromagnetic fields because of the good asymptotic behavior as mentioned in the previous section. Therefore we expand the electromagnetic field inside the sphere as follows;

$$\begin{aligned} \mathbf{E}_{\mathrm{ins}} &= \sum_{l=1}^{\infty} E_l \left(c_l \mathbf{M}^{(1)}_{o1l} - i d_l \mathbf{N}^{(1)}_{e1l} \right) \ , & (2.2.24) \\ \mathbf{H}_{\mathrm{ins}} &= \frac{-k_1}{\omega\mu\mu_0} \sum_{l=1}^{\infty} E_l \left(d_l \mathbf{M}^{(1)}_{e1l} + i c_l \mathbf{N}^{(1)}_{o1l} \right) \ , & (2.2.25) \end{aligned}$$

where $E_l = i^l E_0 (2l+1)/l(l+1)$, whereas the scattered field is expanded as follows;

$$\begin{aligned} \mathbf{E}_{\mathrm{sca}} &= \sum_{l=1}^{\infty} E_l \left(i a_l \mathbf{N}^{(3)}_{e1l} - b_l \mathbf{M}^{(3)}_{o1l} \right) \ , & (2.2.26) \\ \mathbf{H}_{\mathrm{sca}} &= \frac{-k}{\omega\mu_0} \sum_{l=1}^{\infty} E_l \left(i b_l \mathbf{N}^{(3)}_{o1l} + a_l \mathbf{M}^{(3)}_{e1l} \right) \ . & (2.2.27) \end{aligned}$$

The expansion coefficients a_l, b_l, c_l and d_l will be derived based on the Maxwell's boundary conditions in the following section.

2.2.2 Derivation of expansion coefficients of inside and scattered waves

For a give l, there are four unknown coefficient a_l, b_l, c_l and d_l. We therefore need four independent equations, which are obtained from the boundary conditions eq. (2.2.23) in the following component forms;

$$E_{\mathrm{inc}\theta} + E_{\mathrm{sca}\theta} = E_{\mathrm{ins}\theta} \ , \tag{2.2.28}$$

$$E_{\mathrm{inc}\phi} + E_{\mathrm{sca}\phi} = E_{\mathrm{ins}\phi} \ , \tag{2.2.29}$$

$$H_{\mathrm{inc}\theta} + H_{\mathrm{sca}\theta} = H_{\mathrm{ins}\theta} \ , \tag{2.2.30}$$

$$H_{\mathrm{inc}\phi} + H_{\mathrm{sca}\phi} = H_{\mathrm{ins}\phi} \ , \tag{2.2.31}$$

with $r = a$. If we assume that the magnetic permeability of the particle is the same as that of the surrounding medium, and use the above conditions, the orthogonality of the vector spherical functions, the component forms of the functions and the expansion of the three waves as mentioned in previous subsections, we eventually obtain four linear equations for the expansion coefficients;

$$j_l(y)c_l + h_l^{(1)}(x)b_l = j_l(x) \ , \tag{2.2.32}$$

$$[yj_l(y)]' \, c_l + \left[xh_l^{(1)}(x)\right]' b_l = [xj_l(x)]' \ , \tag{2.2.33}$$

$$nj_l(y)d_l + h_l^{(1)}(x)a_l = j_l(x) \ , \tag{2.2.34}$$

$$[yj_l(y)]' \, d_l + n\left[xh_l^{(1)}(x)\right]' a_l = n\,[xj_l(x)]' \ , \tag{2.2.35}$$

where the prime denotes the derivatives of these functions and x and y are

$$x = ka = \frac{2\pi a}{\lambda} \ , \ y = nx \ . \tag{2.2.36}$$

The dimensionless parameter x, well known as the "size parameter", is equal to the ratio of the circumference of the sphere to the wavelength and is the most important parameter throughout the present work. These equations are readily solved and we obtain for the coefficients c_l and d_l of the field inside the sphere

$$c_l = \frac{j_l(x)\left[xh_l^{(1)}(x)\right]' - h_l^{(1)}(x)\,[xj_l(x)]'}{j_l(y)\left[xh_l^{(1)}(x)\right]' - h_l^{(1)}(x)\,[yj_l(y)]'} \, , \tag{2.2.37}$$

$$d_l = \frac{nj_l(x)\left[xh_l^{(1)}(x)\right]' - nh_l^{(1)}(x)\,[xj_l(x)]'}{n^2 j_l(y)\left[xh_l^{(1)}(x)\right]' - h_l^{(1)}(x)\,[yj_l(y)]'} \, , \tag{2.2.38}$$

and for the coefficients a_l and b_l of the scattered field, which is called the scattering coefficients,

$$a_l = \frac{n^2 j_l(y)\,[xj_l(x)]' - j_l(x)\,[yj_l(y)]'}{n^2 j_l(y)\left[xh_l^{(1)}(x)\right]' - h_l^{(1)}(x)\,[yj_l(y)]'} \, , \tag{2.2.39}$$

$$b_l = \frac{j_l(y)\,[xj_l(x)]' - j_l(x)\,[yj_l(y)]'}{j_l(y)\left[xh_l^{(1)}(x)\right]' - h_l^{(1)}(x)\,[yj_l(y)]'} \, . \tag{2.2.40}$$

It is convenient to introduce the Riccati-Bessel functions

$$\psi_l(z) = zj_l(z) \ , \ \xi_l(z) = zh_l^{(1)}(z) \ . \tag{2.2.41}$$

Using these functions the expansion coefficients are simplified as follows;

$$a_l = \frac{n\psi(y)\psi_l'(x) - \psi_l(x)\psi_l'(y)}{n\psi_l(y)\xi_l'(x) - \xi_l(x)\psi_l'(y)} \, , \tag{2.2.42}$$

$$b_l = \frac{\psi(y)\psi_l'(x) - n\psi_l(x)\psi_l'(y)}{\psi_l(y)\xi_l'(x) - n\xi_l(x)\psi_l'(y)} \, , \tag{2.2.43}$$

$$c_l = \frac{-ni}{\psi_l(y)\xi_l'(x) - n\xi_l(x)\psi_l'(y)} \, , \tag{2.2.44}$$

$$d_l = \frac{-ni}{n\psi_l(y)\xi_l'(x) - \xi_l(x)\psi_l'(y)} \, , \tag{2.2.45}$$

where we use the following recurrence relations for eqs. (2.2.44) and (2.2.45);

$$\psi_{l+1}(z) = \frac{2l+1}{z}\psi_l(z) - \psi_{l-1}(z) \ , \tag{2.2.46}$$

$$\psi_l'(z) = -\frac{l}{z}\psi_l(z) + \psi_{l-1}(z) \ , \tag{2.2.47}$$

and similarly for $\xi_l(z)$. When a_l and b_l vanish as n approaches unity, that is, when the refractive index is the same as that of the medium, the scattered field is not generated.

It is noted that the denominators of a_l and d_l are identical as are those of b_l and c_l. When one of those denominators is very small for a given l, the corresponding "mode" will dominate the scattered and inside fields, presenting resonance structure as a function of the size parameter. The a_l mode for the scattered field and the d_l mode for the inside field are dominant if the condition

$$n\psi_l(y)\xi_l'(x) - \xi_l(x)\psi_l'(y) = 0 \ , \tag{2.2.48}$$

is satisfied. Similarly, The b_l mode and the c_l mode are dominant if

$$\psi_l(y)\xi_l'(x) - n\xi_l(x)\psi_l'(y) = 0 \ , \tag{2.2.49}$$

is satisfied. Eqs. (2.2.48) and (2.2.49) are called characteristic equations. As seen in eqs. (2.2.32) through (2.2.35), the characteristic equations are independent of the incident field although we now consider the polarized plane wave as the incident field.

When the conditions (2.2.48) or (2.2.49) are satisfied, the resonant standing wave builds up inside the sphere. Such resonances are called morphology dependent resonances (MDRs). The characteristic equation (2.2.48) for a_l and d_l modes give the resonance size parameters of the transverse magnetic (TM) modes of MDRs. These modes have no radial component of the magnetic field because a_l and d_l are the coefficients of vector spherical functions $\mathbf{M}_{e1l}$ for the scattering and inside magnetic fields (see eqs. (2.2.25) and (2.2.27), and note that $\mathbf{r} \cdot \mathbf{M} = 0$). The corresponding electric fields are given by $\nabla \times \mathbf{M}_{e1l} \propto \mathbf{N}_{e1l}$. On the other hand, eq. (2.2.49) for the b_l and c_l modes give the resonance size parameters of the transverse electric (TE) modes which have no radial component of the electric field because b_l and c_l are also the coefficients of $\mathbf{M}_{e1l}$ (see eqs. (2.2.24) and (2.2.26)).

MDRs are responsible for the ripple structure observed in the Mie scattering spectrum. The resonant peaks constricting the structure appear at the size parameters satisfying the characteristic equations. In the following subsection we will describe characteristics of scattering coefficients a_l and b_l corresponding to the TM and TE modes of MDRs.

2.2.3 Characteristics of scattering coefficients

The scattering efficiency Q_{sca}, which is obtained by integrating the scattered fields over the total solid angle, is written in terms of the scattering coefficients a_l and b_l as follows [44, 50, 51];

$$Q_{\mathrm{sca}} = \frac{2}{x^2}\sum_{l=1}^{\infty}(2l+1)\left(|a_l|^2 + |b_l|^2\right) \ . \qquad (2.2.50)$$

Figure 2.5 shows computed Q_{sca} for a sphere with refractive index $n = 1.4$ as a function of the size parameter x. Although the scattered field is a superposition of the modes as seen in eq. (2.2.50), a mode dominates at a given x where the mode satisfies the condition eq. (2.2.48) for the a_l mode or eq. (2.2.49) for the b_l mode. This causes the appearance of many resonant peaks in this spectrum. Since the denominators of a_l (b_l) and d_l (c_l) are identical, the field inside the sphere and the scattered field dominate at the same parameter.

Figure 2.6 shows an expanded view of the scattering efficiency spectrum of Fig. 2.5, centered around x=17. The Lorenzian line shapes of the MDRs are observed.

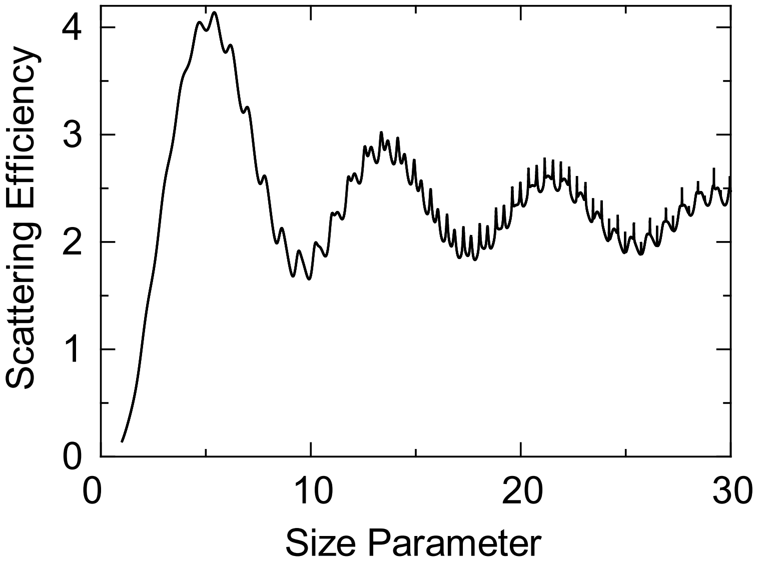

Fig. 2.5: Computed Q_{sca} for the sphere with refractive index $n = 1.4$ as a function of the size parameter x.

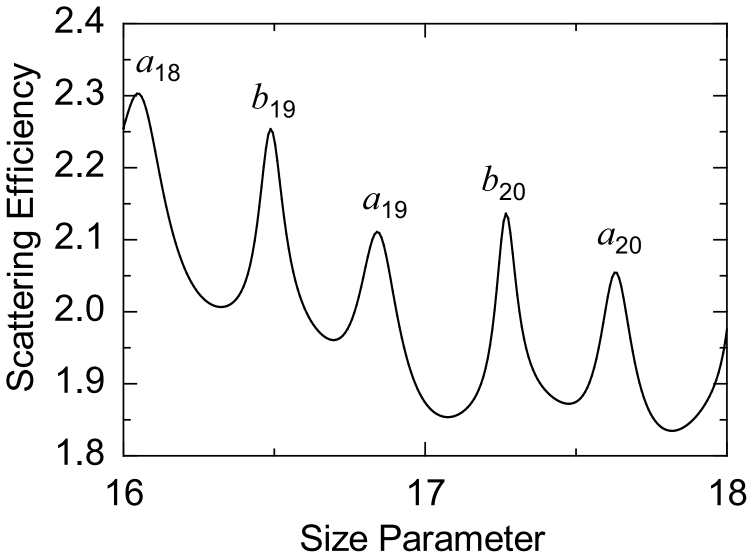

Fig. 2.6: The expanded view of the scattering efficiency spectrum of Fig. 2.5, centered around x=17.

The resonant peaks become progressively narrower as the size parameter increase (see the successive a_l peaks). The peaks of the b_l coefficients corresponding to the TE modes precedes those of the a_l coefficients corresponding to TM modes. The width of the b_l peak is narrower than that of the a_l peak. Figure 2.7 shows the real (solid line) and imaginary (dotted line) parts of the a_{19} scattering coefficient in the same range as Fig. 2.6. The imaginary component of the coefficient changes sign from positive to negative as the size parameter increase. This change occurs at the size parameter of the top of the resonant peak and is useful for computing spectral positions of MDRs.

The contribution of a_{19} MDR to the scattering efficiency is shown in Fig. 2.8. The three MDR peaks are observed in this size parameter range. In the spectrum the resonance peak of the lth mode and the sth order is denoted as $a_{l,s}$. As increasing the size parameter the first-order resonance appears in the spectrum, then the second-order resonance with broader line width, followed by the third-order resonance with the broadest line width among the three resonances. Remarkably,

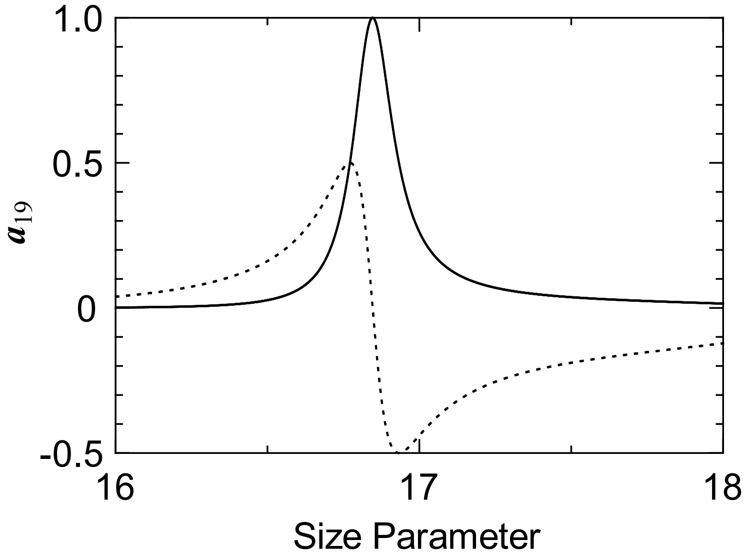

Fig. 2.7: The real (solid line) and imaginary (dotted line) parts of the a_{19} scattering coefficient in the same range as Fig. 2.6.

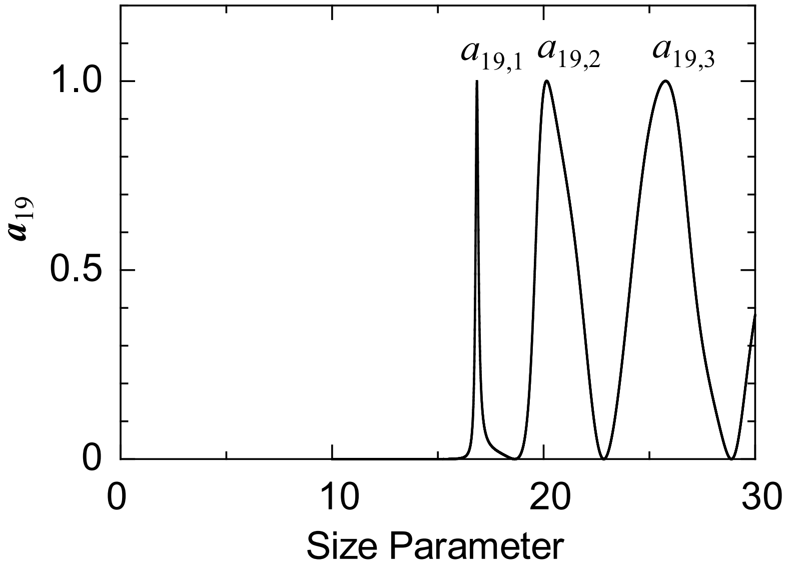

Fig. 2.8: The contribution of a_{19} to the scattering efficiency spectrum. The resonance peak of the l mode and the s order are shown as $a_{l,s}$.

only the first-order resonance is observed in the scattering efficiency spectrum. In the present case the remaining peaks are too broad to be observed individually in the spectrum. The mode number l indicates the number of maxima between 0 and 180 degrees in the angular distribution of MDRs. While the order number s indicates the number of maxima in the radial dependence of the MDRs where only maxima inside the sphere are included. Details of spatial characteristics of MDRs will be presented in the following section.

2.3 Morphology Dependent Resonances

MDRs correspond to the solutions to the characteristic equations (2.2.48) and (2.2.49). MDRs are characterized by three numbers, s, l and m, for both polarizations corresponding to TE (transverse electric) and TM (transverse magnetic) modes. TE and TM modes have no radial components of electric and magnetic fields, respectively. These integers distinguish intensity distribution of the resonant mode inside a sphere. As mentioned in the previous section, the order number s indicates the number of peaks in the radial intensity distribution inside the sphere and the mode number l is the number of waves of resonant light along the circumference of the sphere. The azimuthal mode number m describes azimuthal spatial distribution of the mode. For the perfect sphere, modes of MDRs are degenerate in respect to m. In this section we first describe a simple model of MDRs in terms of geometric optics. Secondly, we show the spatial characteristics of MDRs with a number of illustrative figures. Thirdly, we discuss the quality factors of MDRs. Finally, we state an analogy between MDRs and a hydrogen atom.

2.3.1 Simple model of MDRs

In this subsection we discuss a simple model of MDRs in terms of geometric optics for a qualitative interpretation. We assume a spherical particle with radius a and refractive index n. A ray propagates inside the sphere as hitting the surface with incident angle of $\theta_{\rm in}$. The ray is almost totally reflected inside the sphere when $\theta_{\rm in}$ is larger than a certain critical angle $\theta_{\rm c}(=\arcsin(1/n))$ as shown in Fig. 2.9 (A). For the spherical symmetry the ray hits the surface with the same angle subsequently and is then trapped near the surface. A fraction of the light wave leaks due to the diffractive effect, which will be only revealed when MDRs are dealt with wave optics. Resonant standing waves, i.e, MDRs, grow along the circumference of the sphere if the ray returns to the same position in phase as shown in Fig 2.9 (B). This condition is given by

$$2\pi a \approx l\frac{\lambda}{n} \ , \tag{2.3.1}$$

where l is an integer and $2\pi a$ is a distance in one round trip of the ray. Using a size parameter $x(=2\pi a/\lambda)$, eq. (2.3.1) is simplified as follows;

$$l \approx nx \ . \tag{2.3.2}$$

Eq. (2.3.1) will be derived in another way when we use a photon instead of the ray in Fig. 2.9. The momentum p of the photon is well known as follows;

$$p = \hbar k_1 = \hbar n\frac{2\pi}{\lambda} \ , \tag{2.3.3}$$

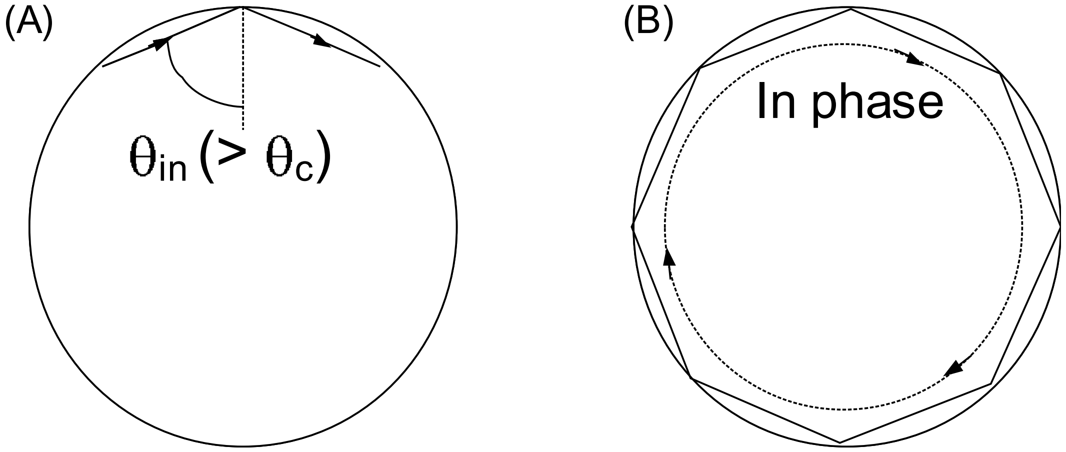

Fig. 2.9: (A)The ray hits the surface of the spherical particle at glancing angle. If $\theta_{\rm in} > \theta_{\rm c}$ the totally reflection occurs. (B)If the ray returns to the same position in phase, resonant standing waves grow along the circumference of the sphere.

where $\hbar$ is Planck's constant h divided by 2π and k_1 is the wave number inside the sphere. When the photon hits the surface at glancing angle and propagates close to the surface, the angular momentum $\hbar l$ is

$$\hbar l \approx ap = a\hbar n \frac{2\pi}{\lambda} \ . \tag{2.3.4}$$

This result is identical to eq. (2.3.1). Remarkably, the integer l, which is introduced as the number of wavelengths in the circumference, is identified as the angular momentum of the photon in the unit of $\hbar$.

When the photon propagates the great circle inclined at an angle θ with respect to the z-axis as shown in Fig. 2.10, the z component of the angular momentum m is

$$m = l \cos\left(\frac{\pi}{2} - \theta\right) \ . \tag{2.3.5}$$

It is to be noted that the modes are degenerate with respect to m because of the spherical symmetry of the sphere.

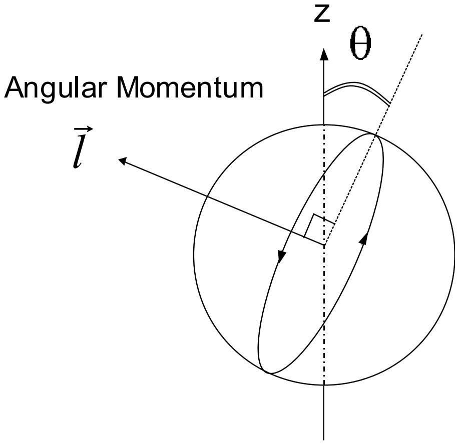

Fig. 2.10: The resonant light wave propagates along the great circle whose normal direction is inclined at an angle $\pi/2 - \theta$ with respect to the z-axis.

2.3.2 Spatial characteristics of MDRs

The vector functions **M** and **N** not only satisfy the vector wave equation but also have the required properties of electromagnetic fields as mentioned in §1.1.2. Therefore these functions correspond to the electromagnetic fields inside the sphere. Spatial characteristics of MDRs are described in terms of **M** and **N** at resonant size parameters satisfying the characteristic equations (2.2.48) and (2.2.49). Since TE modes are defined as the electric field having no radial components, these modes are represented by the vector functions **M**. Similarly, since TM modes are defined as the magnetic field having no radial components, these modes are represented by the vector functions **M**. The corresponding electric fields are represented by the vector functions **N** because the rotation of **M** is proportional to **N**.

Using the vector wave functions (2.1.69) through (2.1.72), the internal electric fields of a sphere are expanded as a sum of following functions;

$$\mathbf{E}_{\mathrm{TE}} = \mathbf{M}^{(1)}_{eml} + i\mathbf{M}^{(1)}_{oml} \, , \tag{2.3.6}$$

$$\mathbf{E}_{\mathrm{TM}} = \mathbf{N}^{(1)}_{eml} + i\mathbf{N}^{(1)}_{oml} \, , \tag{2.3.7}$$

where superscript (1) represents the Bessel functions of the first kind $j_l(nkr)$ adopted as radial dependence of the fields, while subscripts TE and TM represent TE and TM modes, respectively. The spatial distributions of the electric field of TE and TM modes of MDRs are obtained by $|\mathbf{E}_{\mathrm{TE}}|^2$ and $|\mathbf{E}_{\mathrm{TM}}|^2$ at the size parameter satisfying characteristic equations for a given l.

Figure 2.11 shows the internal intensity distributions in the equatorial plane of a sphere with $n = 1.4$ for (A)$\mathrm{TE}_{30,1}$, (B)$\mathrm{TE}_{30,2}$ and (C)$\mathrm{TE}_{30,3}$ modes, where the subscript denote mode and the order numbers. The resonant size parameter is shown in the upper side of each figure. Here the distributions are obtained by adding MDRs rounding along the $+\phi$ ($m = 30$) and $-\phi$ ($m = -30$) directions. Remarkably, the number of peaks in the angular distribution is identical as the mode number l multiplied by a factor 2, while the number of peaks in the radial intensity is the mode order s.

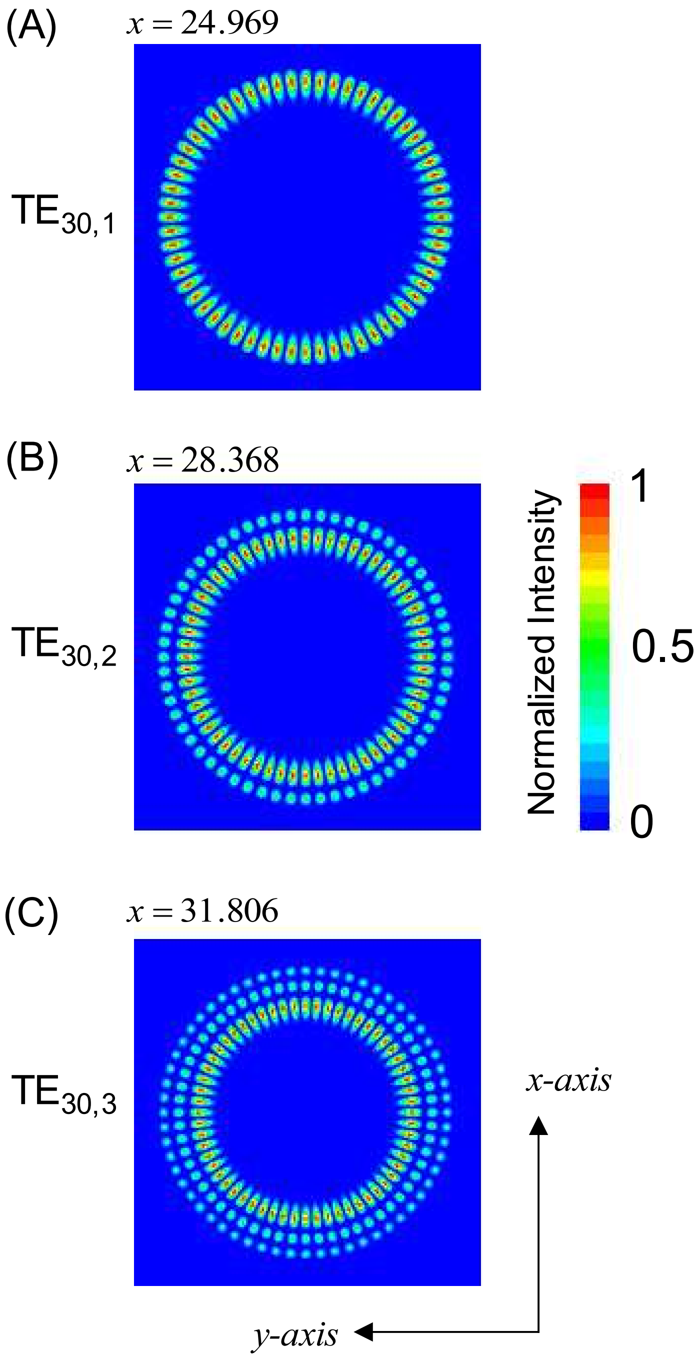

Fig. 2.11: The internal intensity distributions in the equatorial plane for (A)TE$_{30,1}$, (B)TE$_{30,2}$ and (C)TE$_{30,3}$ modes of a sphere with $n = 1.4$. The resonant size parameters are shown in the upper side of each figure.

Figure 2.12 shows the angular distribution of three TE MDRs with $l = 30$ and $m = 1$, 15 and 30 as a function of θ varied form 0 to 90 degrees. The maximum intensity of each m-mode is located near $\theta = \sin^{-1}(m/l)$. The $m = 1$ mode is confined near the pole region. The $m = 15$ mode is located near $\theta = \sin^{-1}(15/30) = 30°$ and the $m = 30$ mode is near the equatorial plane ($\theta = 90°$). These results are consistent with the qualitative interpretation mentioned in the previous subsection although the spatial distributions shown in this figure have somewhat broader structure.

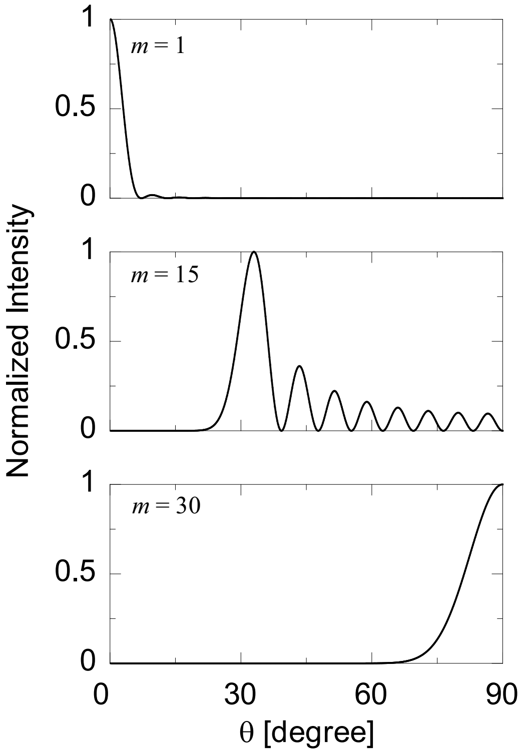

Fig. 2.12: The internal intensity distributions as a function of θ for TE MDRs with $l = 30$ and $m = 1$, 15 and 30. The maximum intensity of each m-mode is located near $\theta = \sin^{-1}(m/l)$.

2.3.3 Quality factors of MDRs

When resonant standing waves grow inside a sphere, the spherical particle acts as a high Q resonator. A fraction of the resonant light wave leaks due to the diffractive effect and the quality factor Q of the resonator is limited by the diffractive losses. Figure 2.13 shows the angle averaged intensity as a function of the normalized radius r/a for TE MDRs with $l = 60$ and $s = 1$, 2 and 3. The refractive index of the sphere is 1.4. This result is obtained by computing $|\mathbf{E}_{\mathrm{TE}}|^2$ integrated over the total solid angle [52]. The electric fields of the MDRs extend beyond the particle boundary as evanescent waves. The lowest order MDR has the maximum of the internal distribution at the region nearest the surface of the sphere, and has the shortest penetration depth toward the outer region of the sphere.

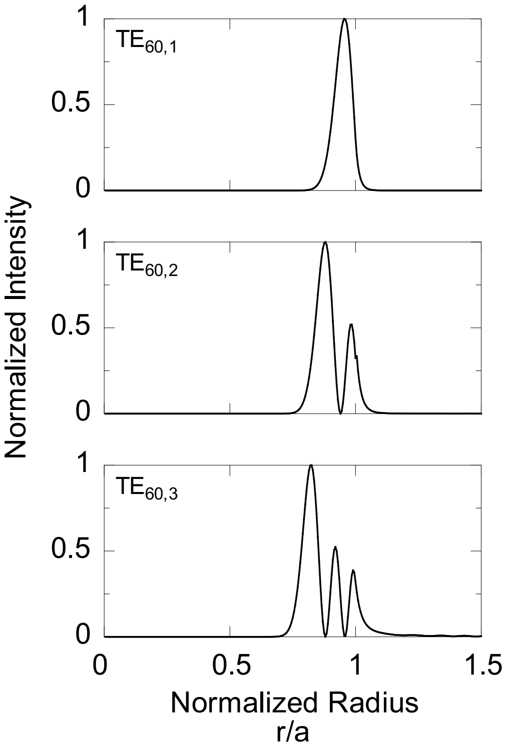

Fig. 2.13: The angle averaged intensity as a function of the normalized radius r/a for TE MDRs with $l = 60$ and $s = 1$, 2 and 3. The refractive index of the sphere is 1.4.

Figure 2.14 shows the resonance curves for the same MDRs and sphere as in Fig. 2.13 as a function of the size parameter, where each resonant size parameter x_0 is centered. The resonance curve of the lowest order MDR is extremely narrow compared with the higher order MDRs. The quality factor Q of the MDR is defined as

$$Q = \frac{x_0}{\triangle x} \,, \tag{2.3.8}$$

where $\triangle x$ is the full width at the half maximum of the resonance curve. The resonance size parameters and the quality factors of these modes are summarized in Table III. The lowest order MDR with the same mode number has the highest quality factor and is therefore most strongly confined inside the sphere.

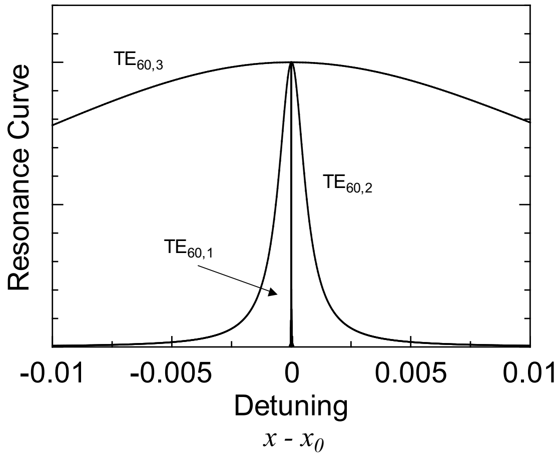

Fig. 2.14: The resonance curves for the same MDRs and the sphere as in Fig. 2.13 as a function of the size parameter, where each x_0 is centered.

Table III: The resonance size parameters and the quality factors of TE MDRs with $l = 60$ and $s = 1$, 2 and 3.

	$\mathrm{TE}_{60,1}$	$\mathrm{TE}_{60,2}$	$\mathrm{TE}_{60,3}$
resonance size parameter	47.491	51.677	55.218
quality factor	9.4×10^6	3.9×10^4	1.6×10^3

Figure 2.15 shows the resonance curves for the first order TE MDRs with $l = 30$, 45 and 60 as a function of the size parameter, where x_0 is also centered. The refractive index of the sphere is 1.4. Q increases as the mode number is increased for a fixed s. The resonance curve of $\mathrm{TE}_{60,1}$ MDR is also extremely narrow compared with the lower mode MDRs. The resonance size parameters and the quality factors of these modes are summarized in Table IV.

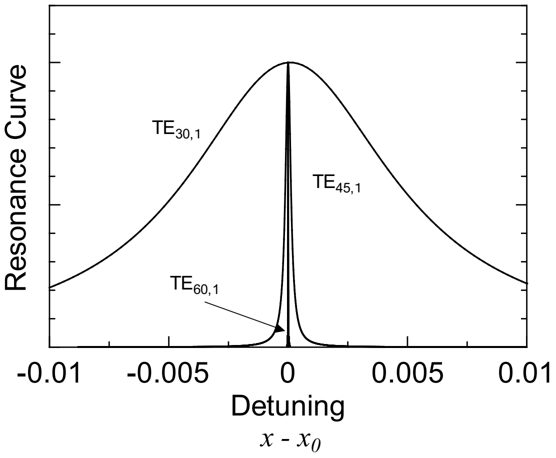

Fig. 2.15: the resonance curves for the first order TE MDRs with $l = 30$, 45 and 60 as a function of the size parameter, where x_0 is also centered. The refractive index of the sphere is 1.4.

Table IV: The resonance size parameters and the quality factors of the first order TE MDRs with $l = 30$, 45 and 60.

	$\mathrm{TE}_{30,1}$	$\mathrm{TE}_{45,1}$	$\mathrm{TE}_{60,1}$
resonance size parameter	24.969	36.299	47.491
quality factor	2.3×10^3	1.3×10^5	9.4×10^6

2.3.4 Analogy between MDRs and hydrogen atom

On the analogy of quantum mechanics, three integers, s, l and m, correspond to the radial, the total angular momentum and the azimuthal quantum numbers, respectively. The system of a dielectric sphere with MDRs is often called "photonic atom" by analogy with a hydrogen atom. The photon confined in the spherical particle is analogous to the electron bound in the hydrogen atom. While the spatial distributions of MDRs correspond to the eigenfunctions of the vector wave equation for electromagnetic fields in the sphere, the orbitals of the electron are to those of the Schrödinger equation for the hydrogen atom.

The solution to the separated differential equation (3.1.14) with respect to ϕ is rewritten by

$$\begin{aligned} \Phi &= \Phi_e + i\Phi_o \\ &= e^{im\phi}. \end{aligned} \tag{2.3.9}$$

and the scalar functions satisfying the scalar wave equations are replaced by

$$\psi = z_l(nkr)Y_{lm}(\theta, \phi), \tag{2.3.10}$$

where $Y_{lm}(\theta, \phi)$ are the spherical harmonics. We here introduce the vector spherical harmonics $\mathbf{X}_{lm}(\theta, \phi)$ as follows;

$$\mathbf{X}_{lm}(\theta, \phi) = \frac{1}{i}\mathbf{r} \times \nabla Y_{lm}(\theta, \phi) \ , \tag{2.3.11}$$

where $\mathbf{r} \times \nabla / i$ is the orbital angular momentum operator of wave mechanics [53]. The electric fields for TE MDRs are given by

$$\mathbf{E}_{\mathrm{TE}} = j_l(nkr)\mathbf{X}_{lm}(\theta, \phi) \ , \tag{2.3.12}$$

which differs from eq. (4.3.1) by a factor i, that is, the phase differs by $\pi/2$ between the two equations[2]. On the other hand, the wave functions Ψ_{slm} for the electron confined in the hydrogen atom are given by [54]

$$\Psi_{slm} = R_{sl}(r)Y_{lm}(\theta, \phi) \ , \tag{2.3.14}$$

---

[2] The relation between eqs. (4.3.1) and (2.3.12) is as follows;

$$\begin{aligned} \mathbf{M}^{(1)}_{eml} + i\mathbf{M}^{(1)}_{oml} &= \nabla \times (\mathbf{r}\psi_{eml}) + i\nabla \times (\mathbf{r}\psi_{oml}) \\ &= \nabla \times (\mathbf{r}\psi) \\ &= \nabla\psi \times \mathbf{r} + \psi\nabla \times \mathbf{r} \\ &= -\mathbf{r} \times \nabla\psi \\ &= -j_l(nkr)\mathbf{r} \times \nabla Y_{lm}(\theta, \phi) \\ &= ij_l(nkr)\mathbf{X}_{lm}(\theta, \phi) \ . \end{aligned} \tag{2.3.13}$$

where $R_{sl}(r)$ is known as the Laguerre polynomials. The two eigenfunctions are very similar and their spatial distributions are characterized by the three integer s, l and m. The probability $P(v)$ of finding the electron between v and $v + dv$, where v is a volume, is obtained by

$$P(v)dv = |\Psi_{slm}|^2 \, dv \ . \tag{2.3.15}$$

If a single photon coupls with TE MDRs of a spherical particle and is trapped in the sphere, the photon extends inside the sphere, and $P(v)$ for the photon should be given by $|\mathbf{E}_{\mathrm{TE}}|^2$.

As seen in Fig. 2.13 the angle-averaged spatial distribution, the spatial distribution of the modes of MDRs penetrate toward the outer region of the sphere. This suggests a coherent coupling occurs between two adjacent spherical particles with the same radius, just as a H_2 molecule is formed due to a overlapping of the wave functions of two H atoms. The system coherently coupled "photonic atoms" should be called "photonic molecule". If we can control the interaction between photonic atoms, we will develop novel type of photonic devices and manipulate photons in micrometer length scale. The application of MDRs to such photonic devices will be discussed in Chap. 5.

Chapter 3

Experimental Details

3.1 Ion Trap Technique

Ion trap technique has been well established for researches of atomic and molecular physics, mass spectroscopy and so on, since W. Paul *et al.* [55] firstly developed an ion trap in the 1950s. The technique is also useful to studies on spherical microlasers because single droplets isolated in the ion trap are not supported by any material and are naturally shaped into almost perfect spheres owing to surface tension. In this section, we deal with the principle of confining charged particles in the ion trap and describe an ion trap originally developed for this work.

3.1.1 Trapping of charged particles in three dimensional quadrupole fields

Particles experience a restoring force to the origin of a coordinate when they are confined in space. We consider the force F increasing linearly with distance r;

$$F = -cr \ , \tag{3.1.1}$$

in other words, a parabolic potential,

$$\Phi \cong \alpha x^2 + \beta y^2 + \gamma z^2 \ , \tag{3.1.2}$$

acts on particles as shown in Fig. 3.1. Electric multipole fields are appropriate to generate such fields for binding charged particles. In the electric quadrupole field, the potential is given in the Cartesian coordinates by

$$\Phi = \frac{\Phi_0}{2r_0^2}(\alpha x^2 + \beta y^2 + \gamma z^2). \tag{3.1.3}$$

The Laplace equation $\triangle\Phi = 0$ imposes the condition $\alpha + \beta + \gamma = 0$. One of the simple ways to satisfy this condition is obtained when $\alpha = \beta = 1$ and $\gamma = -2$ which generate the three dimensional configuration,

$$\Phi = \frac{\Phi_0}{r_0^2 + 2z_0^2}(r^2 - 2z^2) \;\; \text{with} \;\; r_0^2 = 2z_0^2, \tag{3.1.4}$$

in cylindrical coordinates. The ion trap firstly developed by W. Paul *et al.* in the 1950s had the potential configuration given by Eq. (3.1.4) and was built of an hyperbolically shaped ring and two hyperbolic caps, as schematically shown in Fig. 3.2 (A). The static quadrupole potential is shown in Fig. 3.2 (B) when voltage $\Phi_0/2$ and $-\Phi_0/2$ is applied to the ring and end-cap electrodes, respectively. Components of the field **E** is given by

$$E_r = -\frac{\partial\,\Phi}{\partial\,r} = -\frac{\Phi_0}{r_0^2}\,r \;\;,\;\; E_z = -\frac{\partial\,\Phi}{\partial\,z} = \frac{2\Phi_0}{r_0^2}\,z, \tag{3.1.5}$$

because $\mathbf{E} = -grad\,(\Phi)$. It is obvious that the particles with positive charges will perform harmonic oscillations in the r direction (the $x - y$ plane). Their motion

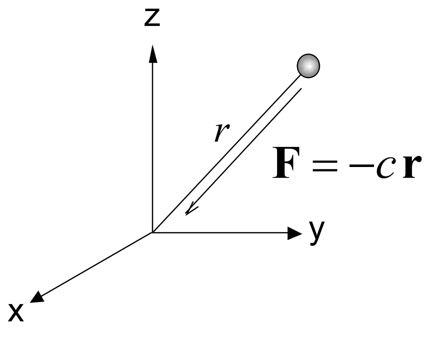

Fig. 3.1: The restoring force **F** increasing linearly with distance r acts on a particle.

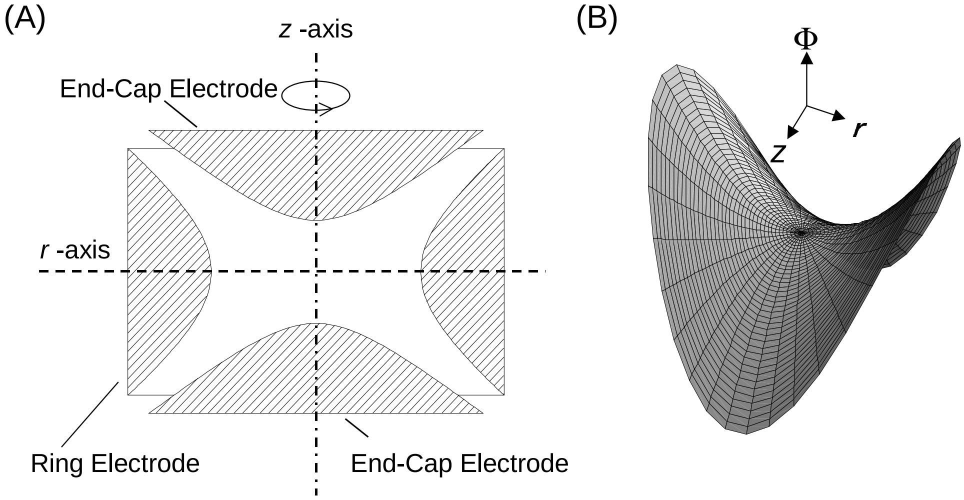

Fig. 3.2: (A) The electrode configuration for the ion trap built of an hyperbolically shaped ring and two hyperbolic caps. These electrode are rotationally symmetric with respect to the z axis. (B) The static quadrupole potential in the ion trap.

around the direction, therefore, will be stable. Oscillation amplitudes in the z direction, on the other hand, will increase exponentially due to the opposite sign in the field E_z, and the particles will be lost by hitting the end-cap electrodes.

The behavior is avoided if the applied voltage is periodic. Charged particles are stable and unstable in both the r and z directions alternately in time due to periodic changes in the sign of the corresponding electric fields. When applied voltage given by

$$\Phi_0 = U + V \cos \omega t \ , \tag{3.1.6}$$

where U is a dc voltage and V is an amplitude of an ac voltage of frequency ω, the equations of motion for the positive charged particle are

$$\ddot{r} + \frac{Ze}{mr_0^2}(U + V \cos \omega t)r = 0 \ , \tag{3.1.7}$$

in the r direction and

$$\ddot{z} - \frac{2Ze}{mr_0^2}(U + V \cos \omega t)z = 0 \ , \tag{3.1.8}$$

in the z direction, where m and Ze are the particle mass and charge, respectively. With dimensionless parameters,

$$\tau = \frac{\omega t}{2}, \quad a_z = -\frac{8ZeU}{mr_0^2\omega^2} = -2a_r \ \text{ and } q_z = -\frac{4ZeV}{mr_0^2\omega^2} = -2q_r, \tag{3.1.9}$$

and replacing r and z to u_r and u_z, Eqs. (3.1.7) and (3.1.8) are simply rewritten by

$$\frac{d^2u_i}{d\tau^2} + (a_i - 2q_i \cos 2\tau)u_i = 0 \quad (i = r,\ z). \tag{3.1.10}$$

The equations are well known as the Mathieu equations and the solutions of these differential equations have been analyzed in detail and are called the Mathieu functions [56].

The Mathieu equation has two linearly independent solutions:

(1) one is a periodic or quasi-periodic function. In the r and the z or both directions, the particles oscillate in the quadrupole field with limited amplitudes and their motion is stable. When their motion is stable in both directions, the particles are confined in the ion trap without hitting the electrodes.

(2) the other is nonperiodic. The amplitudes grow exponentially and the motion of the particles is unstable. As a result, the particle will hit the electrode and be lost.

The parameters a_i and q_i determine the stability of the motion of the particles. Therefore there are regions of stability and instability in an a-q map called the stability diagram. Figure 3.3 shows the stability diagrams for the z (left side) and the r (right side) directions. It is to be noted that the diagram for the r direction differs from that for the z direction by a factor -2 (see eq. (3.1.9)). The stability regions in both diagrams are hatched by oblique lines.

We are interested in the overlapping region of the z and the r directions for confining the particle three dimensionally. The lowest region for stability is shown in Fig. 3.4. The motion of the particles is stable in the z and the r directions only within the region enclosed by four curves. For trapping the particle with the m/Ze ratio, the physical parameters in a_i and q_i are adjusted as a_i and q_i existing in the stability region.

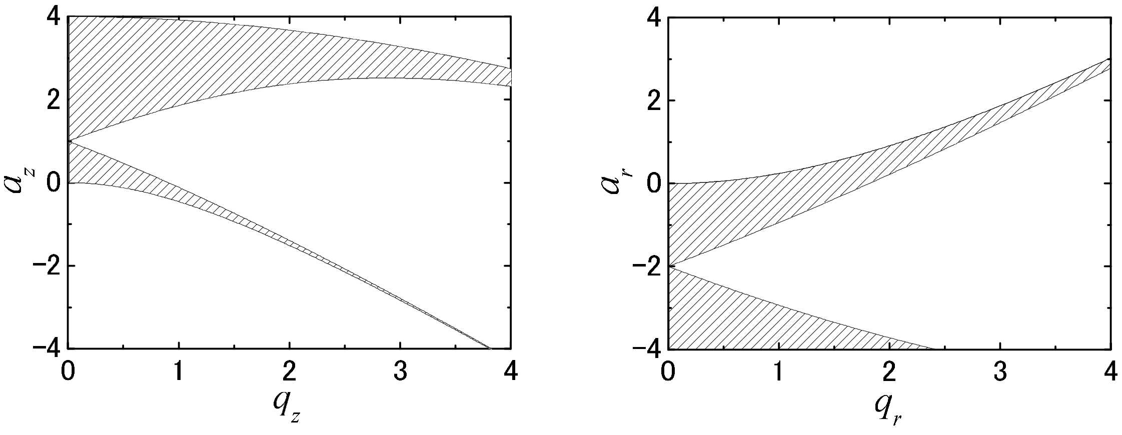

Fig. 3.3: The stability diagram of the Mathieu's differential equations for the z (left side) and the r (right side) directions.

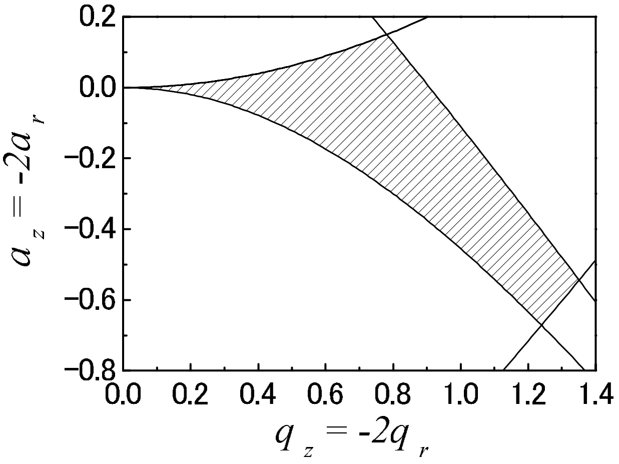

Fig. 3.4: The lowest region for stability in the ion trap.

3.1.2 Ion trap employed in this study

The photographic image in Fig. 3.5 (A) is the ion trap originally developed for the present research on microlasers. The ion trap is built of four disk electrodes holed at their centers. The cross-section of the electrodes is shown in Fig. 3.5 (B) with geometrical dimensions. The electrodes were arranged parallel with their centers

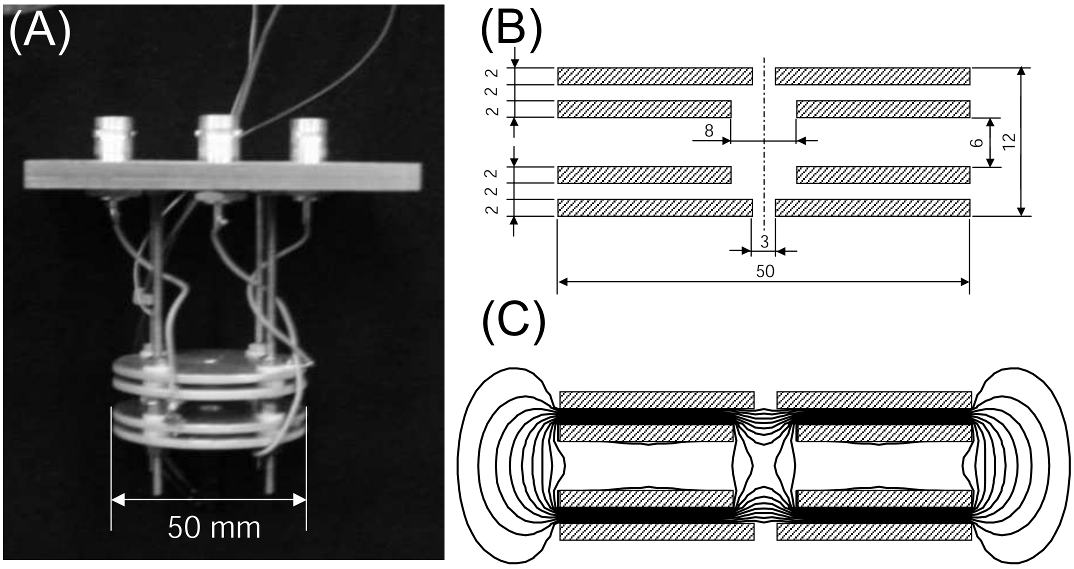

Fig. 3.5: (A) The photographic images of an ion trap employed in this work. (B) The cross-section of four disk electrodes with geometrical dimensions. (C) Equipotential lines around the electrodes when the dc voltage is applied between the two center electrodes and the two end electrodes.

on the vertical axis. Such a configuration of electrodes is suited for detection of elastic scattering light and radiation from suspended microdroplets.

For levitation of charged microparticles, the potential configuration around the center of this ion trap must be quadratic in three dimensions, as mentioned in previous section. The electric potential in the ion trap is obtained by numerically solving the Laplace equation in cylindrical coordinate. We consider a two dimensional grid composed of points separated by a distance h from four nearest neighbors. The potential $\phi(r,z)$ at a position (r,z) is computed in terms of the values of four nearest neighbors. By considering the Taylor series expansion, we get the potential values at the two adjacent mesh points for the r direction as follows;

$$\phi(r+h,z) = \phi(r,z) + h\frac{\partial \phi}{\partial r} + \frac{1}{2}h^2\frac{\partial^2 \phi}{\partial r^2} + \frac{1}{6}h^3\frac{\partial^3 \phi}{\partial r^3} + \mathrm{O}(h^4) \tag{3.1.11}$$

and

$$\phi(r-h,z)=\phi(r,z)-h\frac{\partial\phi}{\partial r}+\frac{1}{2}h^2\frac{\partial^2\phi}{\partial r^2}-\frac{1}{6}h^3\frac{\partial^3\phi}{\partial r^3}+\mathrm{O}(h^4)\ . \qquad (3.1.12)$$

Adding these equations gives

$$\phi(r+h,z)+\phi(r-h,z)=2\phi(r,z)+h^2\frac{\partial^2\phi}{\partial r^2}+\mathrm{O}(h^4)\ . \qquad (3.1.13)$$

By adding this equation to the equivalent results for the z direction and neglecting $\mathrm{O}(h^4)$, we obtain

$$\phi(r,z)=\frac{1}{4}\{\phi(r+h,z)+\phi(r-h,z)+\phi(r,z+h)+\phi(r,z-h)\}\ , \qquad (3.1.14)$$

where we use the Laplace condition,

$$\triangle\Phi=\frac{\partial^2\Phi}{\partial r^2}+\frac{\partial^2\Phi}{\partial z^2}=0. \qquad (3.1.15)$$

Accordingly the potential at point (r,z) is simply given by the mean potential of four nearest neighbors. When we numerically find the solutions for the equation, the Jacobi relaxation method is most often used as one of the simplest approaches. The algorism is as follows:

(1) Initialise $\phi(r,z)$ to some suitable value.

(2) Apply the boundary condition and decide the values of the grid points on the boundary, which is fixed during iterations.

(3) For each internal mesh point, compute the new potential values by using eq. (3.1.14).

(4) Replace old solutions with new ones.

(5) Repeat from step 3 until solutions satisfy desired tolerance.

Figure 3.5 (C) shows equipotential lines of the electric potential generating around the electrodes when the dc voltage is applied between the two middle electrodes and the two end electrodes. Remarkably, the fields stray to the center through the holes of both middle electrodes. Such stray fields play the important role in trapping the particle. In Fig. 3.6 (A), the potential around the center of the electrodes is shown, whereas, in (B), the quadrupole potential generated

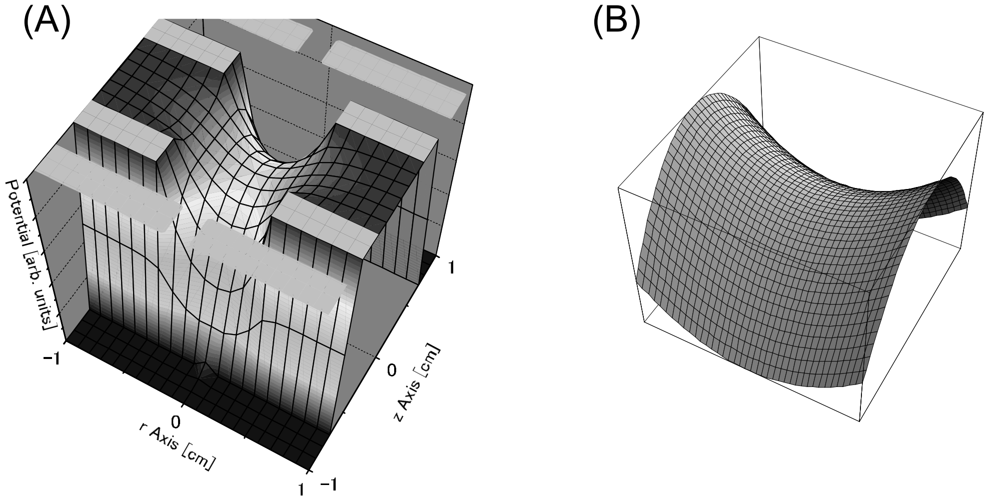

Fig. 3.6: (A) The quasi-quadrupole potential around the center of the ion trap used in this work. (B) The quadrupole potential generated from the hyperbolically shaped electrodes.

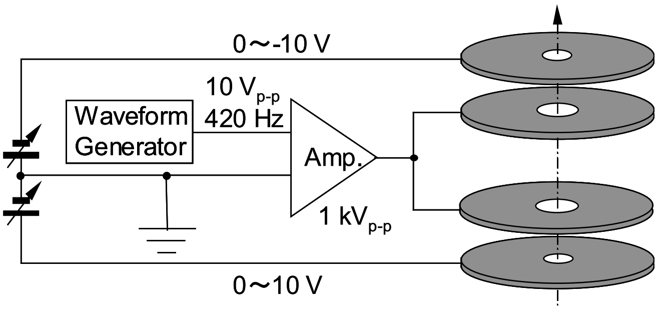

Fig. 3.7: Setup scheme of the ion trap. The two middle electrodes are applied ac voltage, whereas the two end electrodes are used to form an additional dc field.

from the hyperbolically shaped electrodes is shown. By comparing these figures, it is to be noted that the potential formed by the stray field are similar to those generated from the hyperbolically shaped electrodes. Such quasi-quadrupole field suspends charged microparticles.

Figure 3.7 (A) shows setup scheme of the ion trap. The two middle electrodes are applied ac voltage. A 420 Hz sin wave with an amplitude 10 V_{P-P} output from the wave form generator (HP 33120A, Agilent Technologies) is amplified to 1 kV_{P-P} by BOP 1000M POWER SUPPLY (KEPCO, INC.). The two end electrodes are used to form an additional dc field to balance the gravitational force on the droplet. The dc field is generated by the power supply (PMM35-1.2DU, KIKUSUI Electronics Corp.).

3.1.3 Single microdroplet levitated in the ion trap

Microdroplets are most often produced by devices utilizing piezoelectrically actuated droplet ejectors. In this work, however, glycerol droplets doped with rhodamine 6G (Rh6G) molecules are generated with a method of electro-spray ionization (ESI) as schematically shown in Fig 3.8 (A). A syringe contains solutions of R6G molecules dissolved in a glycerin and is attached with a needle having the inner diameter of 0.1 mm. By applying a high voltage ($\approx$ 2 kV) between the needle and a charging electrode, charged microdroplets are generated and injected in the ion trap.

The photographic image in Fig. 3.8 (B) shows the microdroplet levitated

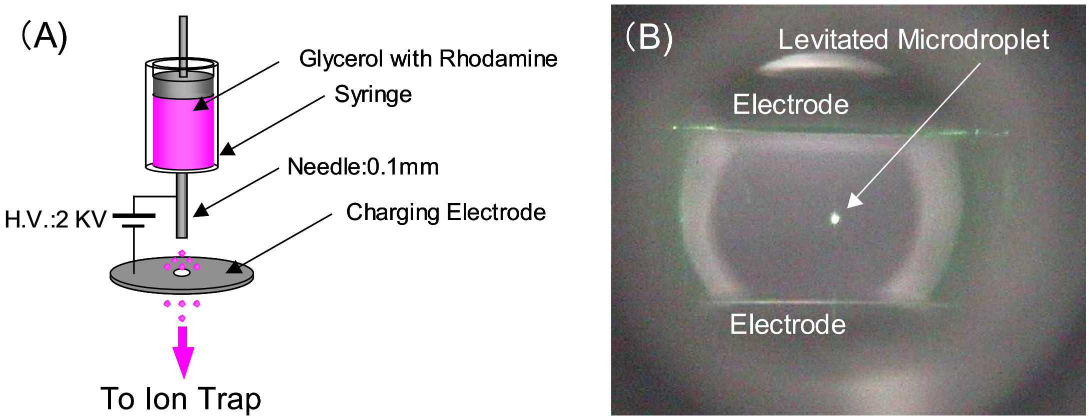

Fig. 3.8: (A) The method of electro-spray ionization (B) The photographic image of the microdroplet levitated in the ion trap.

at the center of the two middle electrodes of the ion trap. By levitating the isolated microdroplet not only the wall effect is prevented but also an almost perfect spherical shape can be maintained due to surface tension. Light waves elastically scattered by such a spherical particle exhibit a distinct spatial intensity distribution. Figure 3.9 shows the scattering light pattern obtained when a He-Ne laser beam irradiate a droplet in the ion trap and scattering light waves through the window is detected by a CCD camera positioned at an angle of 90 !with respect to the beam. The radius of the spherical particle is evaluated by comparing the pattern with the Mie theory. In this case, the radius is estimated at 6.7 μ m.

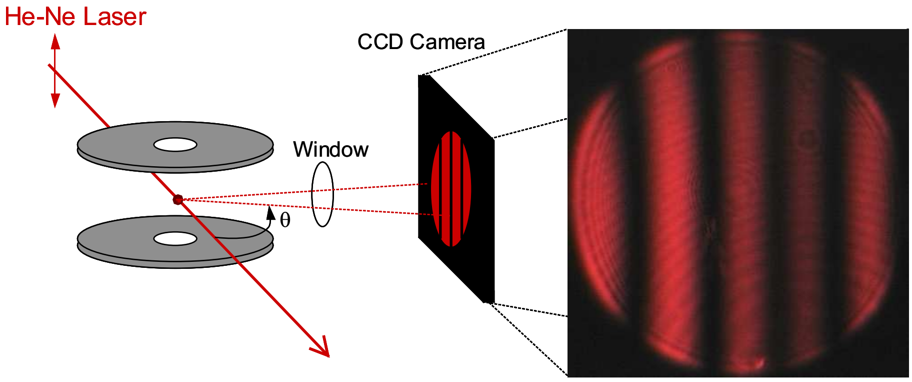

Fig. 3.9: The distinct scattering light pattern from the spherical microparticle.

3.2 Observation Methods of Emission from Single Droplets

In this section, we present the experimental apparatus for observations of emission from single droplets levitated in the ion trap. The following subsection describes the overview of the experimental apparatus. The subsequent subsection exhibits specifications of the main instruments in detail. In the last subsection, devices for simultaneously obtaining emission spectra and microscopic images are described.

3.2.1 Overview of the experimental apparatus

Figure 3.10 schematically shows the experimental setup for obtaining emission spectra and microscopic images of a levitated droplet. The ion trap assembly is housed in a chamber in which dry air is cooled using a thermoelectric cooler attached to the base plate of the chamber. A droplet in the ion trap is irradiated by a pulsed or a CW Nd:YAG laser operating in the 532 nm second harmonic. Perpendicularly emitted radiation from the droplet is focused onto the slit of a 50 cm-spectrometer and detected by an image-intensified charge-coupled device (CCD) detector for spectral analysis. The perpendicularly radiating images are also photographed with a color CCD camera mounted on a microscope. Optical filters are placed between the both CCD cameras and the droplet to block the elastically scattered strong incident radiation. A CCD camera shown in the right side of this figure is used to detect the elastically scattered light through the window.

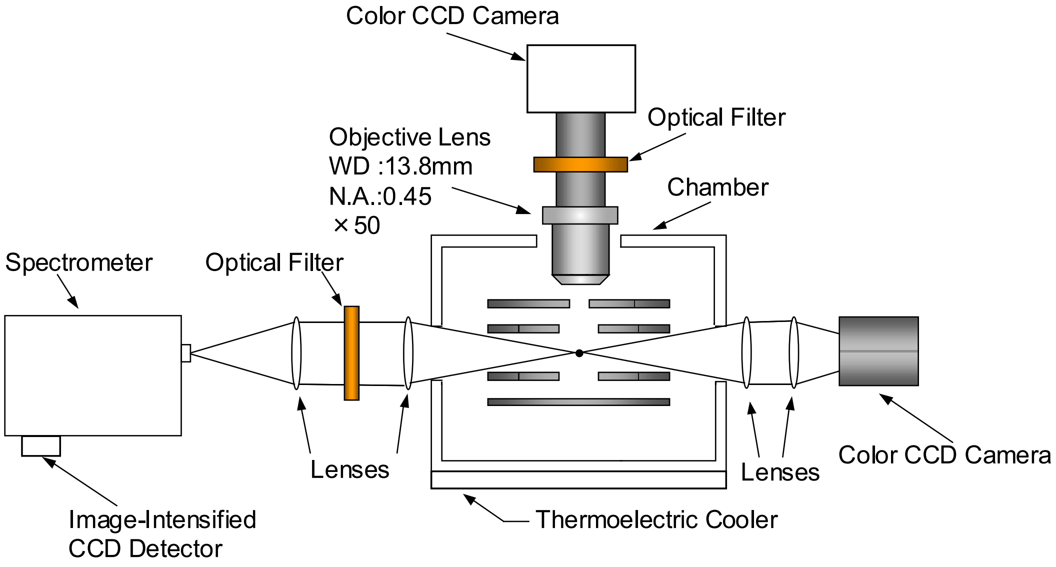
Color CCD Camera
Optical Filter
Objective Lens
WD :13.8mm
N.A.:0.45
×50
Chamber
Spectrometer
Optical Filter
Lenses
Lenses
Color CCD Camera
Image-Intensified
CCD Detector
Thermoelectric Cooler

Fig. 3.10: Schematic of experimental setup for optical spectroscopy and microscopy of the droplets in the ion trap.

3.2.2 Specifications of the main instruments

In what follows we describe specifications of the main instruments, including the chamber, the pump laser, the spectrometer and the optical microscope.

Chamber for housing the ion assembly

The chamber for housing the ion trap assembly is composed of five parts, a top plate, a sidewall and an upper and a lower base plates as shown in the upper side of Fig. 3.11. The top prate is holed at the center for inserting the objective lens of the microscope and has four holes around the center for attaching BNC connectors. The ion trap assembly is attached to this plate as shown in the figure. The sidewall has four windows for optical access. The drawings of these parts are shown in Appendix A. A thermoelectric cooler (SL-10W, Nippon Blower Co.,Ltd.) is attached on the lower base plate which is fixed to an optical bench.

Pump laser for exciting dye molecules

In order to efficiently excite Rh6G dye molecules, we employ a Nd:YAG laser operating in the 532 nm second harmonic as a pump laser in this work. For CW pumping, we use a diode pumped green laser (DPGL series, Usho Optical Systems Co. Ltd.). Maximum output power is 17 mW. Beam diameter and divergence are 0.06 mm and 10 mrad, respectively. For pulse pumping, we use a Q-switched Nd:YAG laser (Quanta-Ray LAB-130-30, Spectra-Physics Lasers, Inc). The Q switch is used to shorten the pulse and raise its peak power. Maximum output energy is 100 mJ/pulse. Beam diameter and divergence are < 10 mm and < 0.5 mrad, respectively. Repetition frequency is 30 Hz. Pulse width is 10 ns, which is measured by using the electric circuit shown in the left side of Fig. 3.12. A fraction of the pump beam is detected by a high-speed Si PIN photodiode (S5973, Hamamatsu Photonics K.K.) and recorded by a digital oscilloscope (Infiniium 600 MHz 4Gs/s, Agilent Technologies). The temporal spectrum of the pump beam is shown in the right side of this figure.

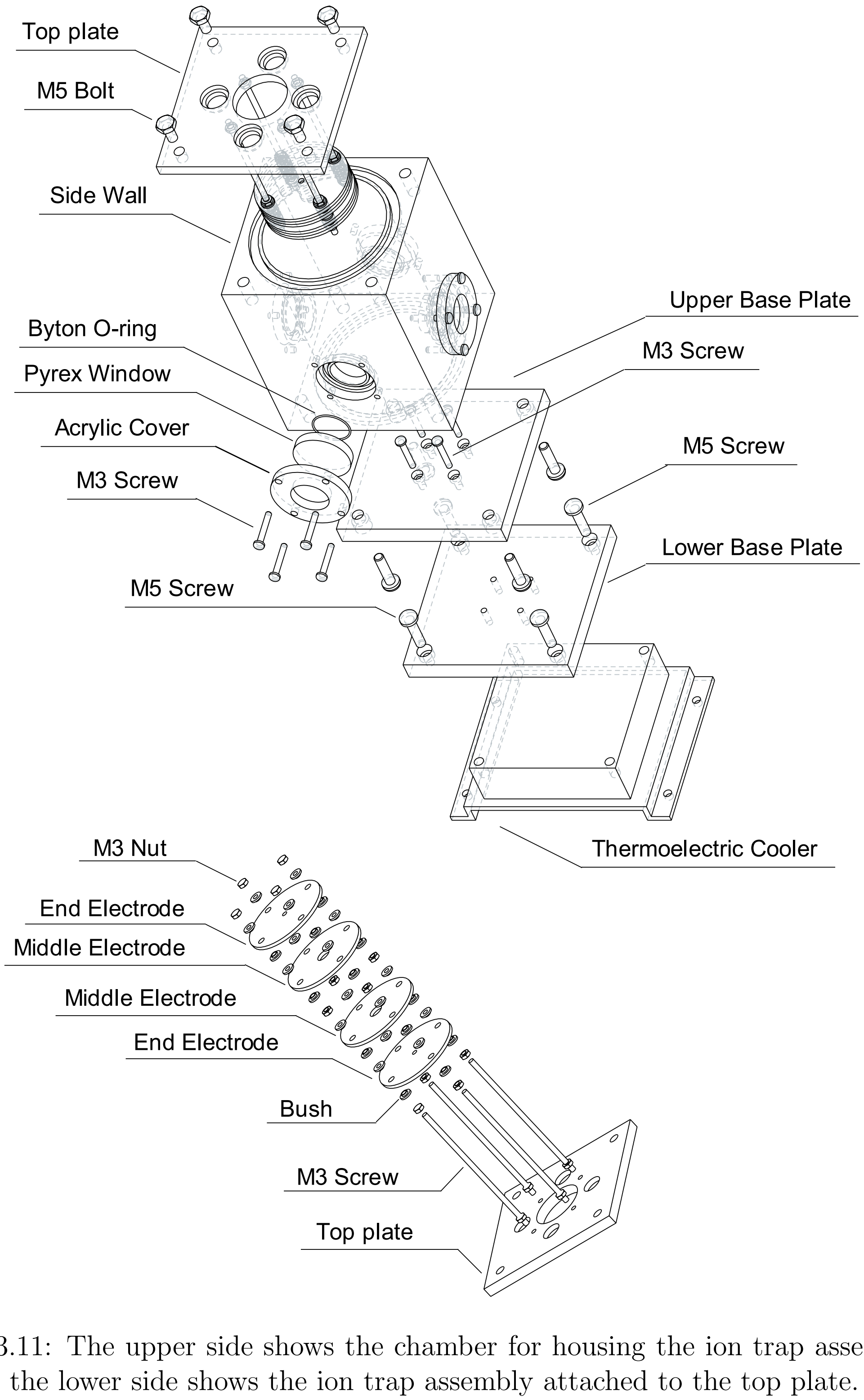
Top plate
M5 Bolt
Side Wall
Upper Base Plate
Byton O-ring
M3 Screw
Pyrex Window
Acrylic Cover
M5 Screw
M3 Screw
Lower Base Plate
M5 Screw
Thermoelectric Cooler
M3 Nut
End Electrode
Middle Electrode
Middle Electrode
End Electrode
Bush
M3 Screw
Top plate

Fig. 3.11: The upper side shows the chamber for housing the ion trap assembly, while the lower side shows the ion trap assembly attached to the top plate.

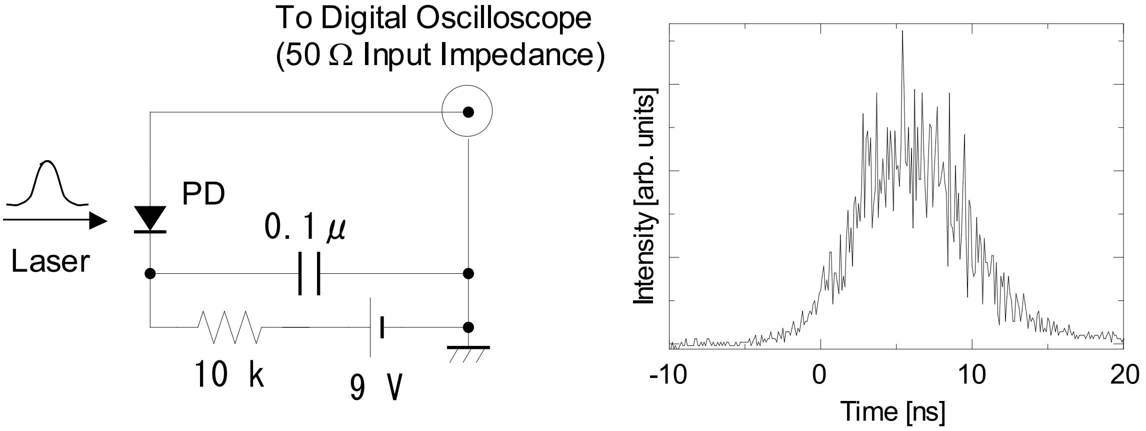

Fig. 3.12: The electric circuit for the measurement of the pulse width (left side). The temporal spectrum of the SHG radiation (532 nm) of the Q-switched Nd:YAG laser (right side)

Monochromator equipped with an image-intensified CCD detector

We use a monochromator (SpectraPro-500i Model SP-558, Acton Research Co.) equipped with dual exit ports; one is for a sliding tube CCD adapter. Focal length f is 500 mm and aperture ratio is $f/6.5$ for 68 × 68 mm gratings. Three gratings with 150, 600 and 1800 groove/mm, are installed in the monochromator. For spectral analysis the monochromator is equipped with an image-intensified CCD detector (ITE/CCD Detector, Princeton Instruments, Inc.) in which the CCD array detector, 1024 × 256 pixels, is cooled using a thermoelectric cooler to $-25°$C, controlled by a ST-138 controller (Princeton Instruments, Inc.). The spectral resolution of the spectrometer for each grating is evaluate by the width of spectral lines from a mercury lamp. The left column in Fig. 3.13 shows the mercury spectra obtained by using (A) 150, (B) 600 and (C) 1800 groove/mm gratings. For each frame, spectra (a), (b), (c) and (d) are recorded when the entrance slit width is adjusted to 150, 100, 50 and 10 μm, respectively. The right column in this figure shows the full widths at half maximum (FWHM) values of the most intense lines as a function of the slit width. Whenever emission

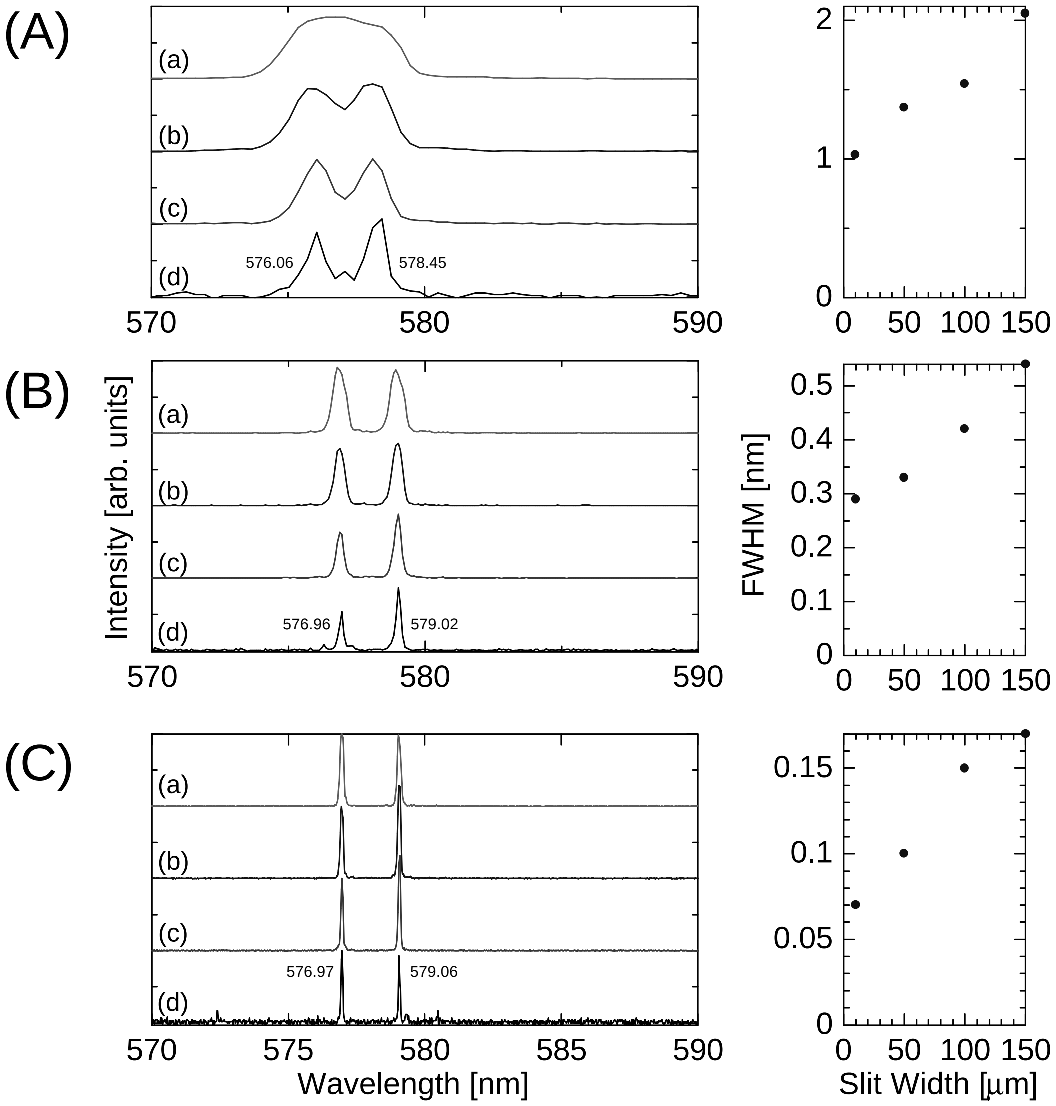

Fig. 3.13: The left column is the mercury spectra obtained by using (A) 150, (B) 600 and (C) 1800 groove/mm gratings. For each frame, spectra (a), (b), (c) and (d) are recorded when the slit width is adjusted to 150, 100, 50 and 10 μm, respectively. The right column shows the values of FWHM plotted as a function of the slit width.

from microdroplets is spectrally recoded, we adjust the entrance slit to 50 μm throughout this study. Thus the spectral resolutions are 0.3 nm for 600 groove/mm grating and 0.1 nm for 1800 groove/mm.

Microscope for obtaining spatial images of levitated microdroplets

We originally developed an optical microscope for obtaining spatial images of radiating microdroplets suspended in the ion trap. Photographic images of the microscope is show in Fig. 3.14. The left side in the figure is the front view of the microscope, while the right is the side view. An objective lens feeds the light emerging from microdroplet into a standard microscope barrel, where the light is filtered by an optical filter and focused onto a color CCD camera, 650 × 488 pixels, (BS-30C, BITRAN Co.). We employ the objective lens (CF Plan, Nikon Co.) with a primary magnification of 50× and a working distance (W. D.) of 13.8 mm. We select the lens whose W. D. is larger than the distance between the

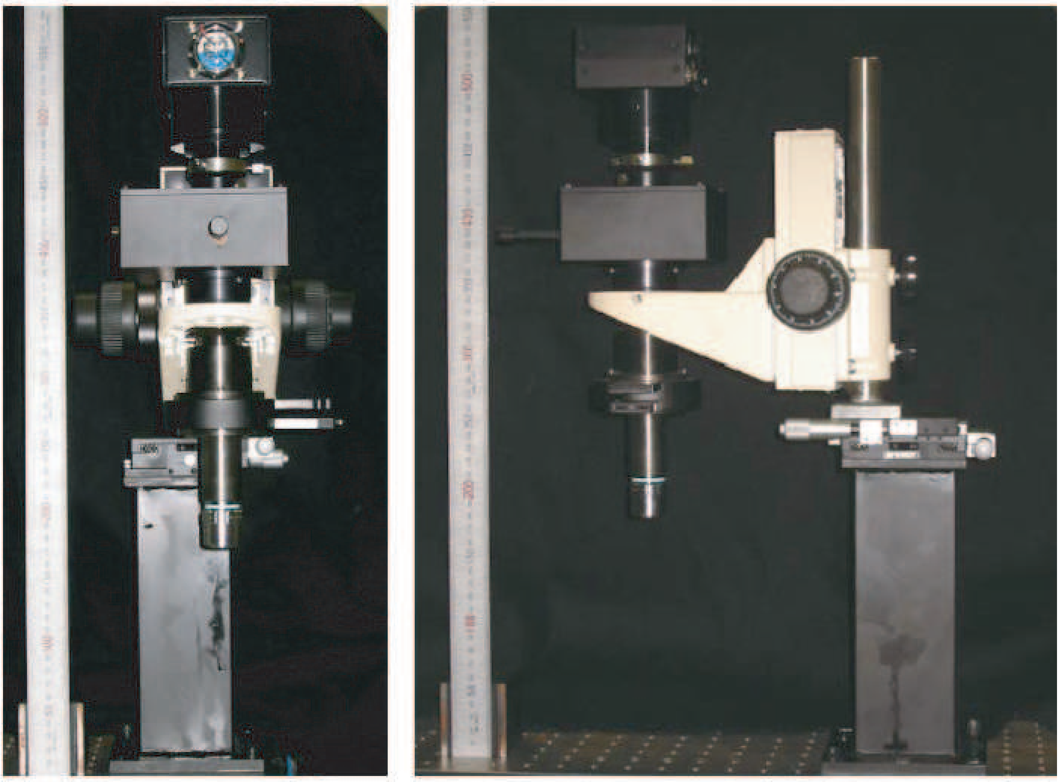

Fig. 3.14: Photographic images of the microscope originally developed for obtaining spatial images of radiating microdroplets suspended in the ion trap. The left is the front view, while the right is the side view.

center of the two middle electrodes and the upper end electrode of the ion trap assembly (see Fig. 3.5).

3.2.3 Methods for simultaneously obtaining emission spectra and microscopic images

Figure 3.15 shows the experimental setup for simultaneously obtaining emission spectra and microscopic images of the microdroplets in the ion trap. Pulses (repetition rate of 30 Hz and duty cycle of 15 percent) synchronous with the Q-switching of the laser is input to a synchronous device. The device gives triggering signals with a suitable delay to a camera controller, a pulse generator and a shutter controller. The electric circuit of the synchronous device is shown in Fig. 3.16 (A) and timing chart of this system is also shown in (B). A mechanical shutter

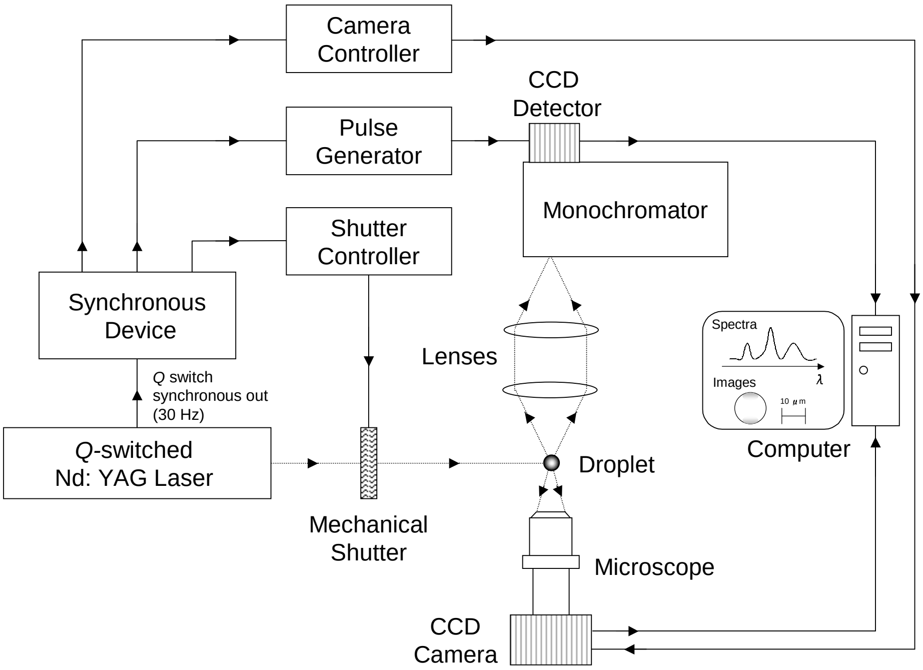
Camera Controller
Pulse Generator
CCD Detector
Shutter Controller
Monochromator
Synchronous Device
Lenses
Spectra
Images
λ
10 μm
Computer
Q switch synchronous out (30 Hz)
Q-switched Nd: YAG Laser
Droplet
Mechanical Shutter
Microscope
CCD Camera

Fig. 3.15: Experimental setup for simultaneously obtaining emission spectra and microscopic images of the microdroplets in the ion trap.

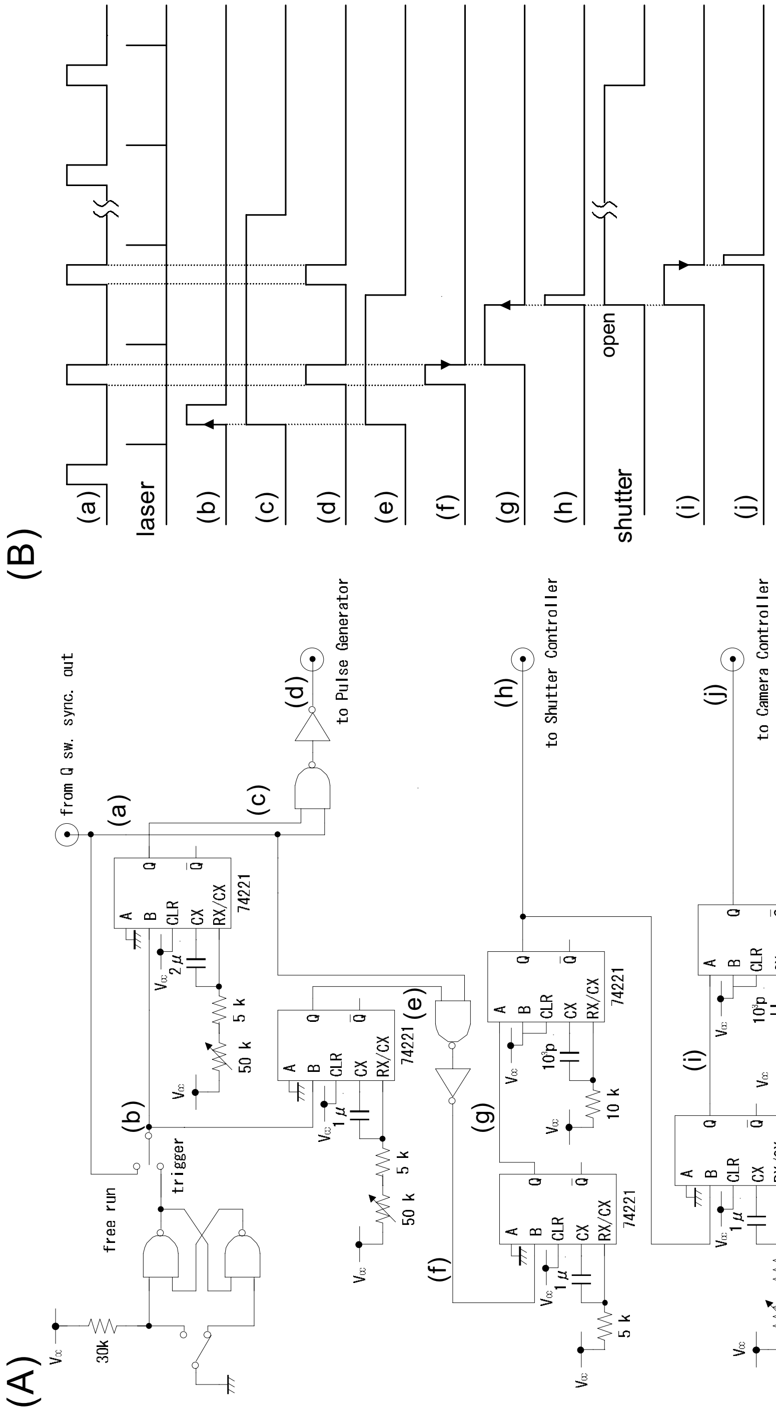
(A)
(B)
from Q sw. sync. out
free run
trigger
30k
Vcc
74221
A
B
CLR
CX
RX/CX
Q
Q̄
2µ
1µ
10p
5 k
50 k
10 k
(a)
(b)
(c)
(d)
(e)
(f)
(g)
(h)
(i)
(j)
to Pulse Generator
to Shutter Controller
to Camera Controller
laser
shutter
open

Fig. 3.16: (A)The electric circuit of the synchronous device. (B) Timing relationships of this system.

(EC-601, NIDEC COPAL Co.) is placed in front of the Q-switched Nd: YAG laser and operated by the shutter controller (EN-609, NIDEC COPAL Co.). To reduce photo bleaching of R6G molecules, the shutter is opened and a droplet is illuminated only for the necessary time to take a spectrum and an image. To obtain emission spectra, high voltage pulses from the pulse generator (PG-200, Princeton Instruments, Inc.) are applied to a microchannel plate contained in the CCD detector. To take spatial images, signals from camera controller open the electrical shutter of the CCD camera attached to the microscope.

Chapter 4

Results and Discussion

4.1 Dependence of Lasing Modes on Pump Intensity

In this section we discuss modes of laser emission from levitated microdroplets observed for various pump intensities. A single dye-doped glycerol droplet of micrometer size was confined in an ion trap and irradiated by a pulsed or a cw green laser. Photographic images of the emitting droplet and emission spectra were simultaneously recorded and compared each other for various intensities of the exciting laser. Both the images and the spectra obtained from the strongly excited droplet have no resemblance to those from the weakly excited one. With stronger excitation, lasing action is found to occur in the droplet in several specific surface azimuthal modes.

4.1.1 Experimental setup

Glycerol droplets doped with rhodamine 6G (Rh6G) molecules were generated with a method of electro-spray ionization. The concentration of dye molecules was 7×10^{-4} mol/L. The droplet was electrically charged and retained at the center of an ion trap in dry air cooled to 12°C at atmospheric pressure. By levitation the isolated microdroplet is not only prevented from wall effect but also can keep an almost perfect spherical shape due to surface tension, guaranteeing a high Q resonator. Details of the experimental apparatus have been described in Chap. 3. The green second-harmonic radiation (532 nm, pulse of 10 nsec width or cw) of a Nd:YAG laser was used to irradiate the droplet. Laser power was varied from 2.3×10^5 to 2.3×10^8 W/cm^2 by neutral density filters for the Q-switched pulse laser. It was 1.1 W/cm^2 for cw laser. The droplet was photographed perpendicular to the laser beam with a color charge coupled device (CCD) camera mounted to a microscope. An optical filter was placed between the camera and the droplet to block the elastically scattered strong incident radiation and only red-shifted fluorescence was observed. Also perpendicularly emitted radiation from the droplet was spectrally analyzed with a 50 cm-spectrometer equipped with a CCD detector. Both the photographic images and emission spectra were recorded simultaneously during the irradiation by the pulse or the cw laser.

4.1.2 Emission spectra from microdroplet for various pump intensities

Figure 4.1 shows emission spectra obtained for various pump intensities. The cw laser was applied for (a), while the Q-switched laser was applied for (b), (c) and (d). MDRs give rise to peak structures in these emission spectra. In spectrum (a), many peaks are superposed on the well-known broad band structure of Rh6G molecules in glycerol throughout the spectral region observed. On the other hand, in spectra (b), (c) and (d), several sharp spectral lines appear predominantly around 600 nm where the losses due to self-absorption by Rh6G molecules are trivial. Spectrum (d) exhibits no broad band structure because the gain for the resonant emission is so large and the continuum fluorescence is negligibly weak compared to the resonant peaks. Since these peak intensities were observed to increase nonlinearly with the pump power, lasing action is believed to occur in such cases.

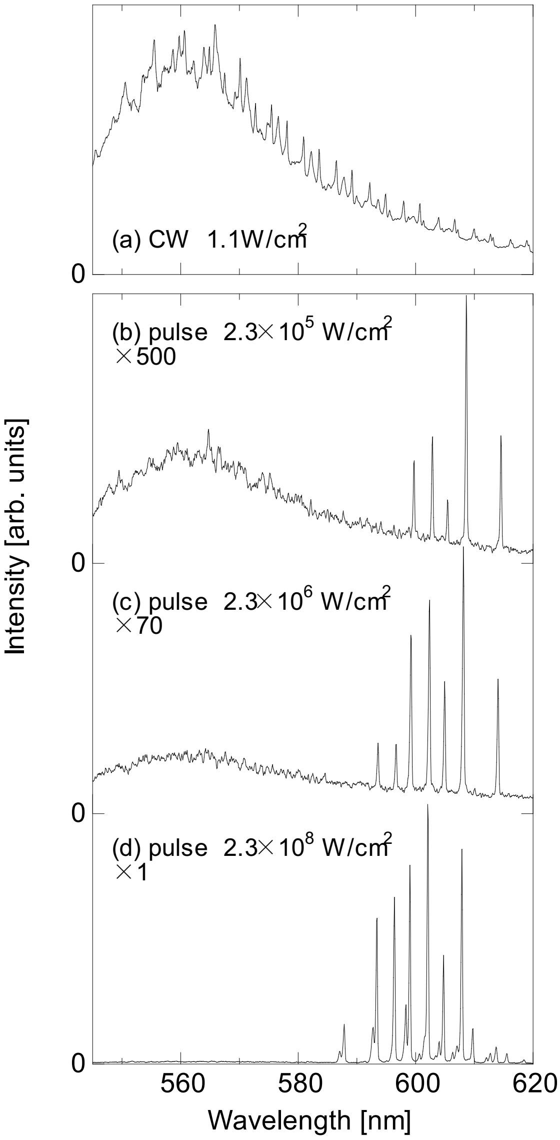

Fig. 4.1: Emission spectra of Rh6G-doped microdroplet for various pump intensities. Only spectrum (a) was obtained by using the cw laser and, in this case, the power is below the lasing threshold, whereas (b), (c) and (d) were obtained by using the pulsed laser.

The spacing of the lines is known to be related to the droplet radius. The approximate spacing in size parameter x between modes of the same order and polarization obtained from the MDR theory is given by [57]

$$\delta x \approx \arctan \rho / \rho \ , \tag{4.1.1}$$

where $\rho = (n^2 - 1)^{1/2}$. By putting in this equation refractive index $n = 1.47$ for liquid glycerol and the observed wavelength spacing of the resonance lines, the radius of the droplet was estimated at 8.0 μm. The corresponding line positions appear to shift slightly from (b) to (c) and from (c) to (d) in the figure. This is due to a slight reduction of the droplet radius during the measurements by the evaporation of glycerol.

4.1.3 Spatial images of microdroplet for various pump intensities

The spatial images of the microdroplet are shown for various pump intensities in Fig. 4.2. These images were simultaneously recorded with emission spectra corresponding to pump intensities in Fig. 4.1. The pump beam was incident from bottom to top in this figure. Only the image (A) was obtained below the lasing threshold, while the images (B), (C) and (D) were above the threshold. The radius a of the droplet is determined from a microscopic spatial image and found to be 8.1 μm which coincides well with the radius estimated from wavelength spacing of the resonance lines.

4.1.4 Discussion

When the exciting laser power is below the threshold as in Fig. 4.2 (A), the yellow-colored fluorescence originates from almost entire region of the droplet. The upper region of the spatial image is brighter than the other portion due to the focusing effect, i.e., incident laser light is refracted at the surface and focused around the opposite side of the particle as schematically shown in Fig. 4.3 (A). The observed intensity distribution is supposed to reflect the intensity distribution of incident light inside the sphere.

Above the threshold as in (B) and (C) in Fig. 4.2, bright, red spots appear in the top and bottom regions near the surface of the sphere besides the fluorescence from the inner region. Excited dye molecules are abundantly produced especially

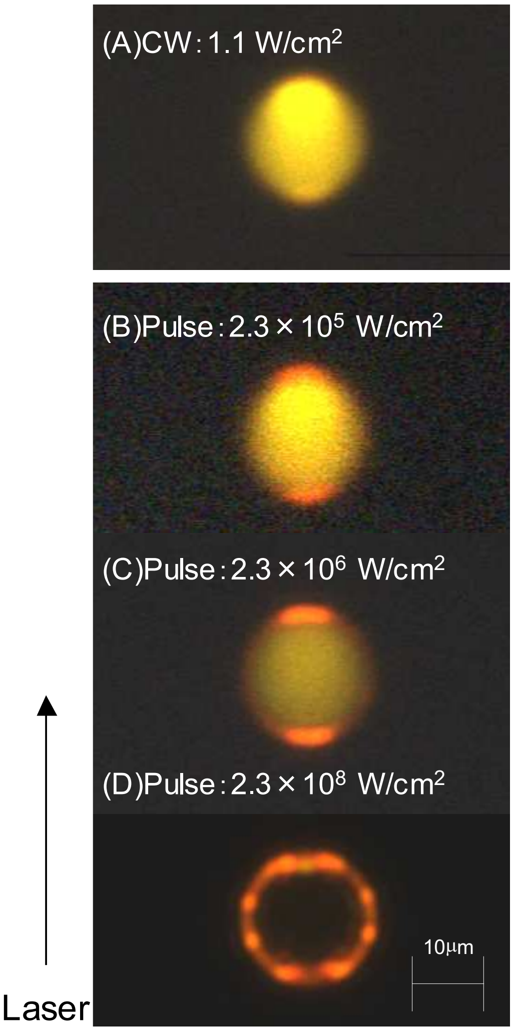
(A)CW: 1.1 W/cm²
(B)Pulse: 2.3 × 10⁵ W/cm²
(C)Pulse: 2.3 × 10⁶ W/cm²
(D)Pulse: 2.3 × 10⁸ W/cm²
10μm
Laser

Fig. 4.2: Microscopic spatial images of light-emitting microdroplet. Images (A), (B), (C) and (D) were simultaneously obtained with corresponding spectra (a), (b), (c) and (d) in Fig. 4.1, respectively.

in the top region due to the focusing effect. Light waves which start from this region are almost totally reflected inside the sphere when the incident angle at the surface is larger than a certain critical angle. If they return to the same position in phase, resonant standing waves grow along the great circles which pass through this region. Optical feedback is thus confined near the surface, and lasing action

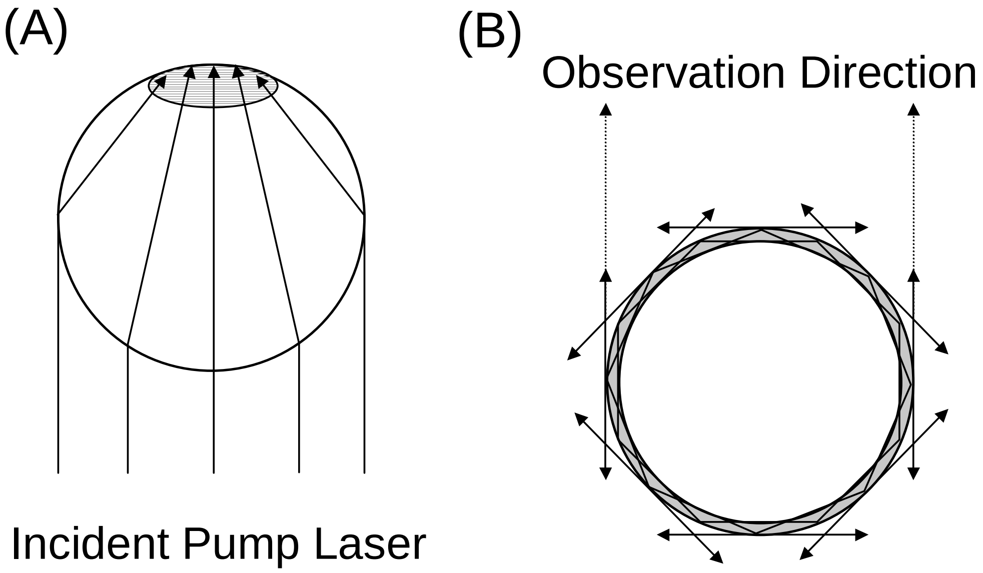

Fig. 4.3: (A) Schematic image of focusing effect. (B)MDRs with low order number confine light waves near the surface of droplet. Only light waves emerging to the direction of observation can be detected.

occurs in these surface modes. Some of the light waves leak through the surface tangentially. Only light waves emerging to the direction of observation can be detected, which causes two bright spots in the spatial images as schematically shown in Fig. 4.3 (B). These image and the emission spectrum in Fig. 4.1 (b) and (c) reveal that the bright spots and the inner fluorescence correspond to the sharp spectral lines and the broad band structure, respectively. The image with bright spots near the surface is consistent with a characteristic of MDRs of low order numbers assigned from the emission spectrum.

At the strongest excitation, only a red rim is discerned as shown in Fig. 4.2 (D). Moreover, the emitting rim structure is not uniform but composed of eight bright spots which are arranged symmetrically about the axis of the exciting laser beam. Since laser beams emerging tangentially from the great circles parallel to the observation direction are detected, the great circles passing through these spots are inclined at discrete angles with respect to the incident laser beam. The observed structure thus suggests that specific surface azimuthal modes are selected for lasing.

Spatial images of laser emission have been reported by several authors for droplets held around a fiber [58] or on a substrate [20]. But we have observed for the first time that the spatial images of the lasing droplet revealed such a distinct symmetric mode structure. This should come from the fact that the almost perfect spherical shape of the droplet is realized due to the levitation of the droplet in the ion trap.

4.1.5 Summary

We have simultaneously observed spatial images and emission spectra of a single microdroplet levitated in an ion trap. The comparison between images and spectra obtained for various intensities of pump power show that the laser emission first occurs in the great circles involving the focusing region of the droplet. Bright spots near the surface of the droplet in the images correspond to sharp peaks of the emission spectra. These observations can be explained by the light waves of the MDRs which are confined near the surface of the sphere. At the strongest excitation in this work, the image displays only red rim which has not a uniform but a symmetric ring structure. Lasing of specific azimuthal modes with such symmetric structures has been observed for the first time.

4.2 Polarization Properties of Lasing Modes

In this section we discuss polarization properties of single lasing microdroplets levitated in an ion trap obtained from both emission spectra and microscopic images. The polarization phenomena strongly depend on the observation direction and the orientation of a transparent axis of the polarization analyzer. We suggest such effects originate because excited molecular dipoles preserve for sufficient period the memory of the polarization of the pump field.

4.2.1 Experimental setup

Microdroplets were composed of liquid glycerol doped with 7×10^{-4} mol/L Rh6G molecules. The droplets were generated by a method of electrospray ionization and injected into an ion trap. The ion trap assembly was housed in a chamber in which dry air was cooled to 6°C using a thermoelectric cooler attached to the base plate of the chamber. Details of the apparatus were described in Chap. 3. A droplet in the ion trap was irradiated by an SHG radiation of a Q-switched Nd:YAG laser (532 nm, pulse width of 10 ns and repetition rate of 30 Hz). The pump power was 8×10^5 W/cm^2, and its intensity was stronger than that of the lasing threshold ($< 10^4$ W/cm^2). The diameter of the pump beam was 0.5 mm and was much larger than the positional fluctuation of a levitated droplet. As shown in Fig. 4.4, direction and polarization of the pump beam are defined as the Z-axis and the X-axis, respectively. The pump beam from the Q-switched Nd:YAG laser was passed through a $\lambda/4$ plate, followed by a polarizer to fix the polarization axis to the desired orientation. Unlike the previous section, analyzing polarizers were additionally installed between the droplet and the spectrometer and the detector of the microscope to obtain the polarization properties of lasing

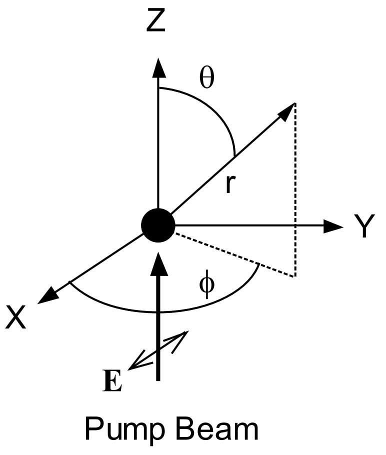

Fig. 4.4: The incident pump beam whose propagation direction and polarization are parallel to the z- and x-axes, respectively.

droplets.

4.2.2 Polarization phenomena obtained from microscopic images of lasing droplets

Figure 4.5 shows microscopic images of a lasing droplet with a radius of 13 μm. These images were taken 60 s apart including the 2 s exposure for the same droplet. Arrows at the left of each image indicate the incident directions and the polarization of the pump beam, while an arrow at the right indicates the orientation of the transparent axis of the analyzer. Images (A) and (C) were

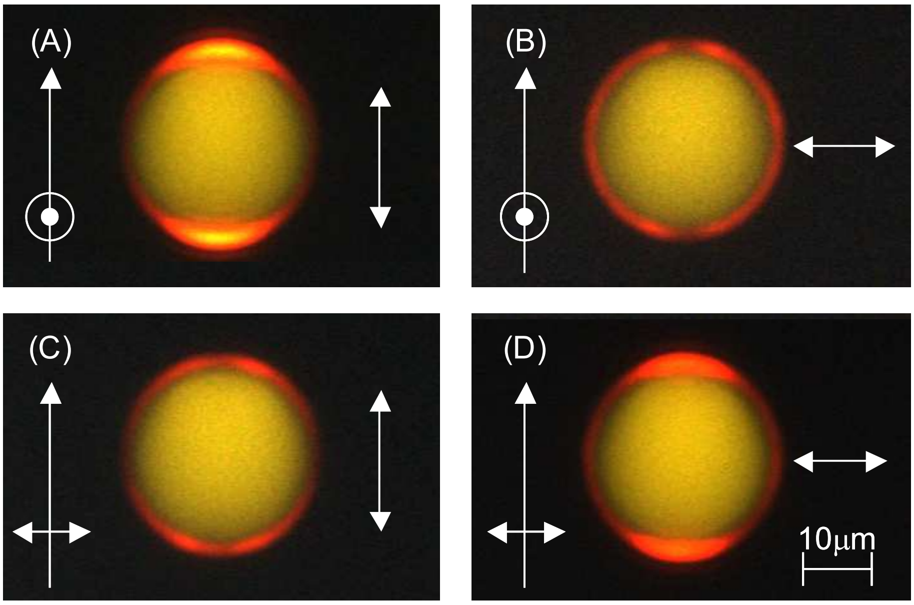

Fig. 4.5: Microscopic images of a lasing microdroplet. Arrows at the left of each image indicate the direction and polarization of the pump beam, while an arrow at the right indicates the transparent axis of the analyzer. In images (A) and (D), laser emissions due to MDRs dominate at both poles, whereas, in (B) and (D), intensities at both poles are considerably weak.

obtained through an analyzer whose axis was parallel to the Z-axis, whereas images (B) and (D) were obtained through the analyzer installed perpendicularly to the Z-axis. The two images at the top of this figure were photographed from the direction of the X-axis, while the two images at the bottom were from the direction of the Y-axis. All images exhibit red-colored laser emission due to MDRs near the surface of droplets in addition to the yellow-colored fluorescence from the inner region. Although laser beams can emerge tangentially from the surface of the droplet into any direction, only beams emitted into the observation direction are detected. Structures due to MDRs are therefore caused by laser beams emitted from the great circles which are parallel to the observation direction. In images (A) and (D), the intensities of the top and bottom poles of the droplet are considerably strong. In images (B) and (C), on the other hand, the intensities of these regions are very weak.

4.2.3 Identification of Polarization of MDRs

Emission spectra are shown in Fig. 4.6 for the same droplet as that in Fig. 4.5. Spectra (A) and (D) were taken 1 min apart, and were recorded under the same polarization conditions as images (A) and (D) in Fig. 4.5 which are inserted in each spectrum. Several sharp lines due to MDRs in the emission spectra correspond to the red-colored lasing emission from the poles of the droplet as seen in the images, while the band structure peaked around 570 nm to the yellow-colored fluorescence. By comparing spectra (A) with (D), it is noted that the laser lines in (A) have a simpler structure than those in (D). In the case of (A), radiation from the TE modes is not detected because, in the pole regions, the transparent axis of the analyzer is parallel to the radial vector and the electric fields of the TE modes have no radial components. The laser lines in (A) are therefore attributed to radiation from the TM modes. The electric fields of TM modes may have not only parallel but also perpendicular components. Hence it follows that the laser lines in (D) corresponding to those in (A) are identified with TM modes and the rest of the peaks in (D) with TE modes.

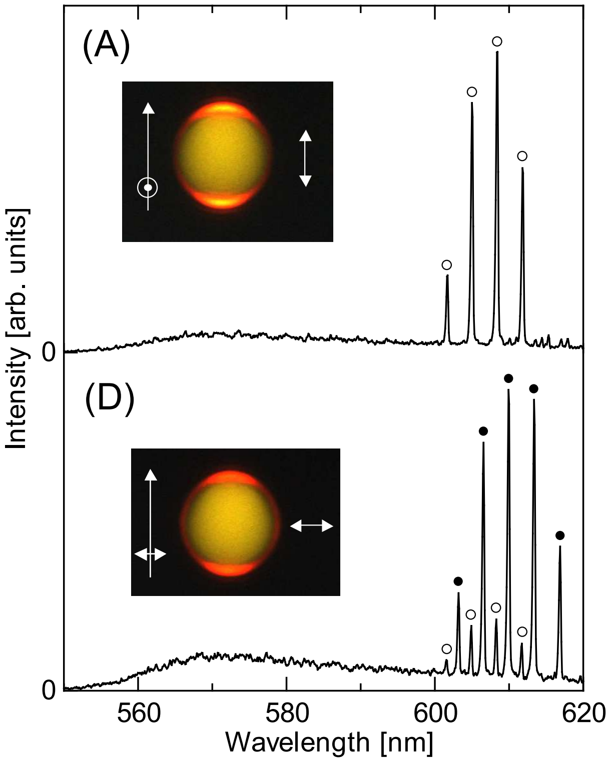

Fig. 4.6: Emission spectra of the lasing microdroplet. Spectra (A) and (D) were obtained under the same polarization conditions as images (A) and (D) in Fig. 4.5. These images are inserted to each spectrum. Only radiation from TM modes can be detected in spectrum (A) since laser light due to MDRs dominates at both poles and TE modes have no radial components. The peaks corresponding to TM and TE modes are indicated by open and closed circles, respectively

When emission spectra were recorded with higher spectral resolution, it was noted that the positions of the laser lines shifted slightly toward shorter wavelength in chronological order. This is due to a reduction in the droplet radius during measurements by the evaporation of glycerol. The amount of blue shift of lasing peaks, $\delta\lambda$, is 0.2 nm/min, which is negligible in the case of lower resolution as in Fig. 4.6. The reduction rate, δa, is approximately given by $\delta a = (a/\lambda)\delta\lambda$ [59], and it is estimated at 4 nm/min in the present case.

4.2.4 Discussion

Distinct polarization phenomena observed at both poles in the spatial images are explained as follows. It is well known that the polarization of emission from cooler dilute dye molecules in glycerol solutions shows stronger dependence on that of excited light because the Brownian rotational motion and the inter-molecular excitation energy exchange are more strongly suppressed [60]. Rotational relaxation time for Rh6G molecules in ethanol was measured at room temperature by several investigators, and was reported to be about 300 ps [61]. This relaxation time is known to be proportional to the ratio of viscosity to temperature [62]. Under our experimental condition the rotational relaxation time can be estimated to be hundreds of ns, since the viscosity of glycerol is larger than that of ethanol by three orders of magnitude and the temperature was lower than room temperature. Memory of polarization will be lost if the rotational relaxation time of molecules in solution is faster than the decay time of the excited state. Kamada *et al.* [63] measured the temporal profile of laser emission from a dye-doped polymer particle of a similar size to ours. They estimated that the time constant of the lasing is in the order of a few ps. This time constant is much shorter than the rotational relaxation time of the molecules. This leads us to assume that a substantial amount of excited molecular dipoles in the droplet memorize the direction of the electric field of pumping light before the stimulated emission and subsequently radiate light waves with the same polarization as the pump field. Therefore it will be useful to consider the distribution of internal electric fields formed by the pump beam inside the droplet.

According to the Mie theory, when the pump beam is incident along the Z-axis and its polarization is parallel to the X-axis, the components of the internal electric field ($\mathbf{E}_{int}$) are expanded by the following functions (see Chap. 2):

$$\begin{aligned} E_r^{TE} &= 0, \\ E_\theta^{TE} &= j_l(\rho)\frac{1}{\sin\theta}Y_{l1}^e, \\ E_\phi^{TE} &= -j_l(\rho)\frac{\partial}{\partial\theta}Y_{l1}^o, \end{aligned} \tag{4.2.1}$$

for TE modes, and

$$\begin{aligned} E_r^{TM} &= l(l+1)\frac{j_l(\rho)}{\rho}Y_{l1}^e, \\ E_\theta^{TM} &= \frac{[\rho j_l(\rho)]'}{\rho}\frac{\partial}{\partial\theta}Y_{l1}^e, \\ E_\phi^{TM} &= -\frac{[\rho j_l(\rho)]'}{\rho}\frac{1}{\sin\theta}Y_{l1}^o, \end{aligned} \tag{4.2.2}$$

for TM modes, where ρ is equal to nkr (k is the wave number and n is the refractive index of the sphere) and $j_l(\rho)$ are Bessel functions. Subscripts, r, θ and ϕ, denote the components in the spherical coordinate as shown in Fig.4.4. The functions Y_{l1}^e and Y_{l1}^o are defined as

$$Y_{l1}^e(\theta,\,\phi) \;=\; P_{l1}(\cos\theta)\cos\phi \tag{4.2.3}$$

and

$$Y_{l1}^o(\theta,\,\phi) \;=\; P_{l1}(\cos\theta)\sin\phi, \tag{4.2.4}$$

where $P_{l1}(\cos\theta)$ gives the associated Legendre functions with $m=1$.

The lasing emissions at the poles of the droplet in Fig. 4.5 (A) and (B) are associated with MDRs growing along the great circles on the X-Z plane ($\phi = 0$). In these cases, $\mathbf{E}_{int}$ on the great circle may have three components, E_θ^{TE}, E_r^{TM} and E_θ^{TM}, because the other components are equal to zero due to $Y_{l1}^o(\theta,\,0) = 0$ as seen in eq. (4.2.4). At both poles, only $E_r^{TM}\mathbf{e}_r$, where $\mathbf{e}_r$ represents a unit vector in the r direction, is parallel to the transparent axis of the analyzer in (A) but perpendicular to that in (B). Hence elastically scattered light waves from these regions should be observed as in (A) but not as in (B).

In order to experimentally confirm the results derived from the Mie theory, Fig. 4.7 (A) and (B) were obtained for microscopic images of a droplet without an optical filter which is usually placed between the droplet and the detector to block the elastically scattered strong incident radiation. The polarization conditions of images (A) and (B) in Fig. 4.7 were the same as those of (A) and (B) in Fig. 4.5, but the pump intensity (2×10^3 W/cm^2) was much weaker than that in the

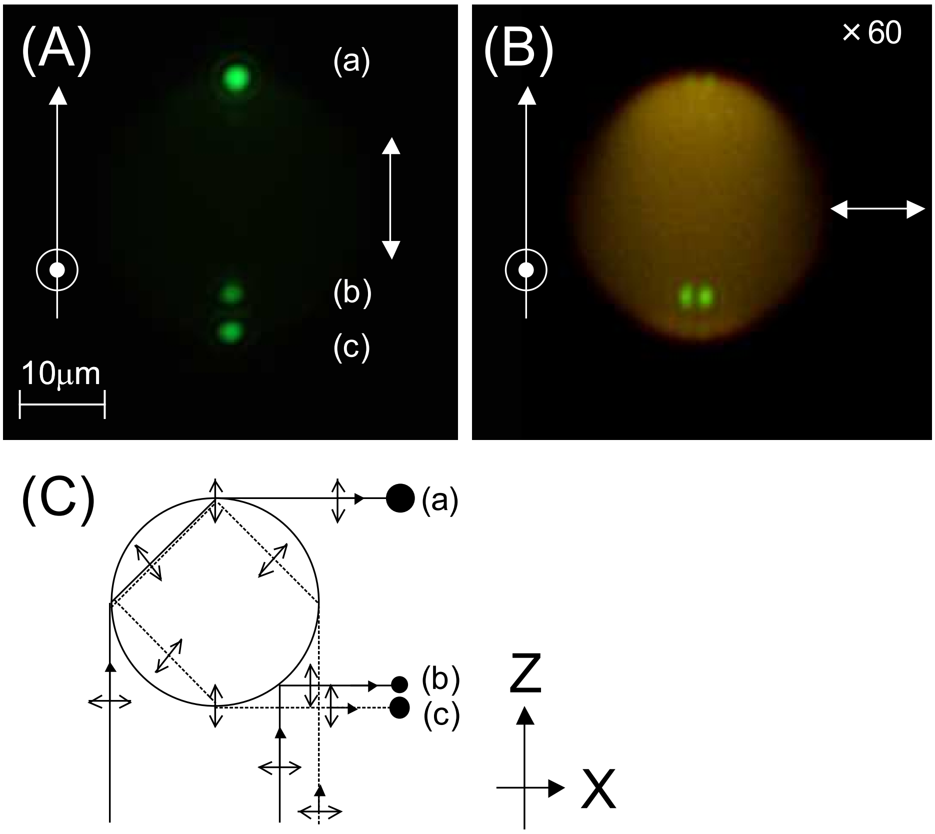

Fig. 4.7: Microscopic images of a microdroplet obtained without an optical filter. The polarization conditions of images (A) and (B) were the same as those of (A) and (B) in Fig. 4.5, but the pump intensity was much weaker than that in the cases of Figs. 4.5 and 4.6. The bright spots in (A) are caused by light rays as shown schematically in (C). Note that the x axis is vertical in (A) and (B), while horizontal in (C).

cases of Figs. 4.5 and 4.6 and was below the lasing threshold. In Fig. 4.7 (A), three bright, green spots are observed, which agrees with the results reported in ref. [64] and is understood in terms of ray trajectories as shown schematically in Fig. 4.7 (C). Spot (a) is caused by a light ray typically traveling one chord within the particle. It corresponds to $p = 1$ in the notation of van de Hulst [65], where $p-1$ represents the number of internal reflections of the ray, while spot (c) corresponds to a ray traveling at least three chords within the particle ($p = 3$).

Spot (b) is due to direct reflection at the external surface of the droplet. This ray has negligible contribution to the excitation of dye molecules inside the droplet. When the polarization analyzer was rotated by 90 degrees, the intensities of these spots were considerably decreased, as shown in Fig. 4.7 (B). These results indicate that pump beams are polarized to the r direction at both poles, and are consistent with those derived from the Mie theory.

Laser beams emitted from dipole moments excited by $E_r^{TM}\mathbf{e}_r$, one of the three nonzero components at the poles, are detected through the analyzer in (A) but not in (B) in Fig. 4.5. Light waves from dipole moments oscillated by $E_\theta^{TE}\mathbf{e}_\theta$ and $E_\theta^{TM}\mathbf{e}_\theta$, the remaining nonzero components, are not observed in either case because $\mathbf{e}_\theta$, the unit vector of θ direction, is parallel to the observation direction in the region close to the poles on the great circle. On the other hand, in the cases of 4.5 (C) and (D), $\mathbf{E}_{int}$ on the great circle on the Y-Z plane ($\phi = \pi/2$) has no components except E_ϕ^{TE} and E_ϕ^{TM} due to $Y_{l1}^{e}(\theta, \pi/2) = 0$. At the poles, the light waves caused by E_ϕ^{TE} and E_ϕ^{TM} are transparent through the analyzer as in (D) but are blocked by the analyzer as in (C).

4.2.5 Summary

We have observed the polarization effects in both emission spectra and microscopic images from a lasing droplet levitated in an ion trap. We have also analyzed the polarization of the pump field by using the Mie theory. From the analysis we suggest that these effects originate because excited dipole moments preserve well the memory of the electric field of the pump beam and emit laser light of the polarization strongly related to the polarization of the pump field.

4.3 Dependence of Lasing Modes on Dye Concentration

In this section we discuss the lasing modes of levitated microdroplets of various dye concentrations. In the last section we have revealed lasing dye-doped microdroplets exhibit distinct polarization phenomena both in emission spectra and in microscopic images. The experimentally determined polarization of lasing peaks was found to be very useful to identify the lasing modes of MDRs. It is expected that, as well known for dye lasers, lasing modes of dye-doped microdroplets strongly depend on dye concentration. Here we show that both microscopic images and emission spectra of lasing droplets change drastically as the decrease of dye concentration and have revealed for the first time that the laser emission of the droplet originates from the coupling of only TE modes with dye molecules in the most dilute case employed in the present work. These results are discussed based on the theoretical Q values of MDRs corresponding to lasing peaks in emission spectra.

4.3.1 Experimental setup

Microdroplets were composed of liquid glycerol doped with Rh6G molecules whose concentration was varied from 7×10^{-6} to 7×10^{-4} mol/L. The droplets were generated by a method of electrospray ionization and injected into the ion trap. Details of the apparatus are described in Chap. 3. A droplet in the ion trap was irradiated by a Q-switched Nd:YAG laser operated in the 532 nm second harmonic (pulse width of 10 ns and repetition rate of 30 Hz). The pump power was 4×10^6 W/cm^2, and its intensity was stronger than that of the lasing threshold ($< 10^4$ W/cm^2). Polarization properties of emission spectra and spatial images were obtained by the similar experimental alignment mentioned in the last section.

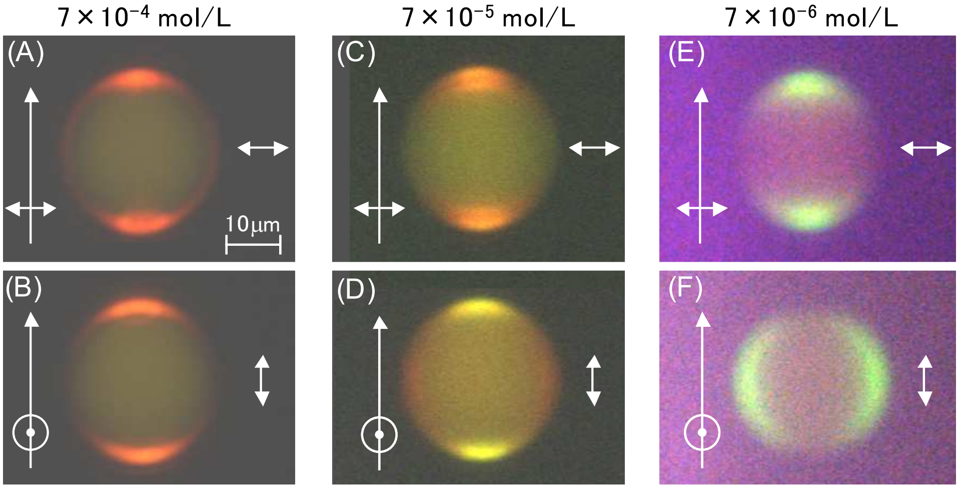

Fig. 4.8: Microscopic images of lasing microdroplets of various dye concentrations. Arrows at the left of each image indicate the direction and polarization of the pump beam, while an arrow at the right indicates the transparent axis of the analyzer. In images (A) - (E), laser emissions due to MDRs dominate at both poles, whereas, in (F), intensities at both poles are considerably weak and lasing from side regions dominates.

4.3.2 Microscopic images of microdroplets

Figure 4.8 shows microscopic spatial images of lasing droplets with 12 μm radii for various concentrations of dye molecules in glycerol solutions. The dye molarities of the droplets in the images of left, middle and right columns are 7×10^{-4}, 7×10^{-5} and 7×10^{-6} mol/L, respectively. Arrows at the left side of each image indicate the direction and the polarization of the pump beam, while an arrow at the right side indicates the transparent axis of the analyzer.

The images (A) through (E) exhibit that laser emission due to MDRs dominates at both poles (top and bottom regions) of the droplets. As mentioned in the previous section, we determined polarization of MDRs from the spatial images when laser emission dominantly emerged from both poles. In the case where the transparent axis of the analyzer is oriented as the lower side of this figure, radiation from TE modes is not detected at the poles because TE modes have no radial components of electric fields. Laser emission observed in the images (B) and (D), therefore, results from the coupling between Rh6G molecules with TM modes of MDRs. On the other hand, in the case where the transparent axis of the analyzer is oriented as the upper side of this figure, radiation not only from TE but also from TM modes is detected at the poles because TM modes may have parallel and/or perpendicular components to radial direction of electric fields.

Only the image (F) exhibits laser emission from side regions of the droplet. As mentioned above if laser emission is from both poles under this polarization condition, radiation from only TM modes will be detected. In the images (E) and (F), only laser emission with polarization perpendicular to radial direction emerges from the droplet. This leads us to suggest that the emission originates from the coupling of only TE modes with Rh6G molecules in this most dilute case. The suggestion will be supported also by polarization properties observed in emission spectra of the droplet as mentioned in the following subsection.

4.3.3 Emission spectra of microdroplets

For pump laser intensity above lasing threshold, as shown in Fig. 4.9, emission spectra represent several sharp spectral lines corresponding to MDRs around the spectral region where losses due to self-absorption by Rh6G molecules are trivial. In this figure bulk absorptions are also shown. The emission spectra (A), (C) and (E) were obtained from the same droplets and under the same polarization conditions as the images (A), (C) and (E) in Fig. 4.8. We find that, as dye concentration decreases from Fig. 4.9 (A), the laser lines shift toward shorter wavelength and the structures of the spectra become more complicated.

Laser lines in the spectrum (A) evidently consist of two clusters; one is composed of relatively intense peaks and the other is the weaker ones. Spacing between laser lines belonging to each cluster is in agreement with the asymptotic relation as seen in eq. (4.1.1). This result leads us to suggest that the lasing emission is supported by MDRs having at most two order numbers corresponding to the

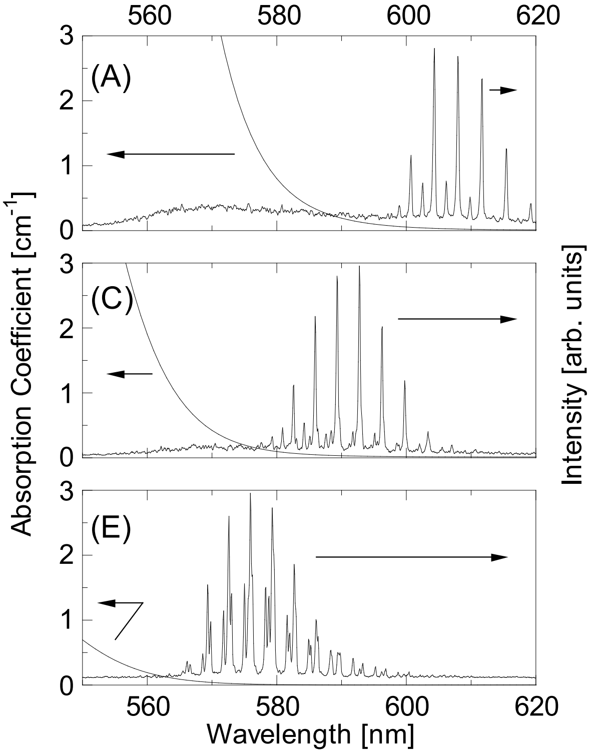

Fig. 4.9: Emission spectra of the lasing microdroplet. Spectra (A), (C) and (E) were obtained under the same polarization conditions as images (A), (C) and (E) in Fig. 4.8. As dye concentration decreases from (A) to (E), laser lines shift toward shorter wavelength and the structures of the spectra become more complicated.

two clusters. In spectra (C) and (E), on the other hand, lasing due to MDRs of several order numbers makes the structures of the spectra complicated.

Emission spectra (A) - (E) in Fig. 4.10 were obtained from the same droplets and under the same polarization conditions as images (A) - (E) in Fig. Fig. 4.8, correspondingly. By comparing spectra (A) with (B), we find that the laser lines in (B) have a simpler structure than those in (A). In (B), radiation from the TE modes is not detected because, in the pole regions, the transparent axis of the analyzer is parallel to the radial vector and the electric fields of the TE modes have no radial components as mentioned in Chap. 2. The laser lines in (B) are therefore attributed to radiation from the TM modes. The electric fields of TM modes may have not only parallel but also perpendicular components to the radial

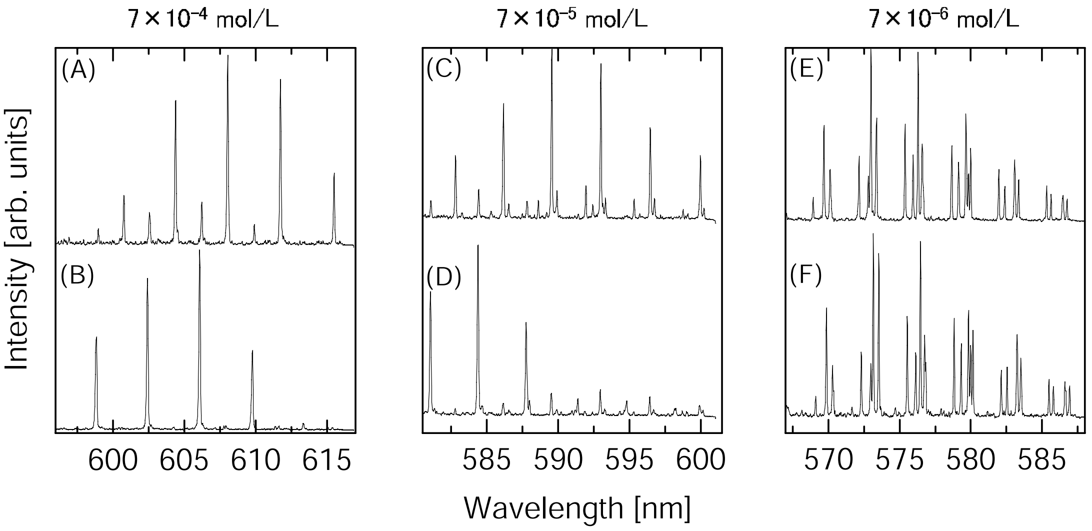

Fig. 4.10: Emission spectra (A) - (E) were obtained from the same droplets and under the same polarization conditions as (A) - (E) in Fig. 4.8, correspondingly.

vector. Hence it follows that the laser lines in (A) corresponding to those in (B) are identified with TM modes and the rest of the peaks in (A) with TE modes. Relatively intense laser lines in (D) are also identified with TM modes. On the other hand, the dominant peaks in (C) which also appeared very weakly in (D) are attributed to radiation from the TE modes.

It is to be noted that lasing from TM modes occurs at shorter wavelength than that from TE modes and the difference between the lasing positions in the case of 7×10^{-5} mol/L is more distinct than that of 7×10^{-4} mol/L. The difference is, however, not seen in the most dilute case of 7×10^{-6} mol/L and the structure of lasing peaks in (E) is almost the same as that in (F). This result strengthens the suggestion made from microscopic images that, in the most dilute case in our observation, excited Rh6G molecules couple only with TE modes in lasing.

4.3.4 Mode identification of MDRs

As mentioned in § 2.2.2, peak positions of MDRs can be determined by characteristic equations derived from the boundary conditions for the tangential components of electric and magnetic fields at the surface of the sphere. Using the Riccati-Bessel functions $\psi_l(z)$ and the Riccati-Hankel functions $\xi_l(z)$, the characteristic equations are give by

$$\psi_l(y)\xi_l'(x) - n\xi_l(x)\psi_l'(y) = 0 \ , \tag{4.3.1}$$

for TE modes, and

$$n\psi_l(y)\xi_l'(x) - \xi_l(x)\psi_l'(y) = 0 \ , \tag{4.3.2}$$

for TM modes, where primes denote the derivatives of the functions and y is equal to nx. Modes of MDRs are most often assigned by fitting the peak positions of emission spectra to those of Mie resonances. An algorithm has been developed to facilitate such an assignment [66]. Observed characteristics of polarization of MDRs have substantially improved the task of the assignment.

The algorithm reported by authors in ref. [66] is as follows. (i) We list N lasing peaks at wavelengths λ_{Ei} $(i = 1, 2, \cdots, N)$. The wavelengths are determined from a emission spectrum as shown in Fig 4.11. (ii) We assume tentative values of a refractive index n and a droplet radius a, and calculate theoretical resonance

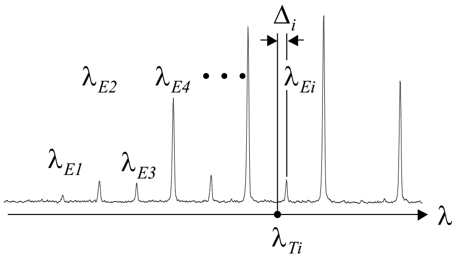

Fig. 4.11: N lasing peaks at wavelength λ_{Ei} $(i = 1, 2, \cdots, N)$ and calculated theoretical resonance position λ_{Ti}. $\triangle_i$ is defined as the difference between λ_{Ti} and λ_{Ei}.

positions λ_T from eqs. (4.3.1) and (4.3.2). (iii) For each λ_{Ei}, the closest λ_T is elected as λ_{Ti} and, we define $\triangle_i$ as the difference between λ_{Ti} and λ_{Ei}. (iv) We consider the correlation,

$$C = \frac{1}{N} \sum_{i=1}^{N} \frac{1}{1 + (\triangle_i/\triangle)^2}, \tag{4.3.3}$$

where $\triangle$ is spectral resolution (in our case $\triangle = 0.1$ nm), and maximize C by adjusting two fitting parameters, n and a, over the range of physically possible values.

Figure 4.12 shows a result identified by such an algorithm for the most dilute droplet. Theoretically obtained mode positions are plotted on the emission

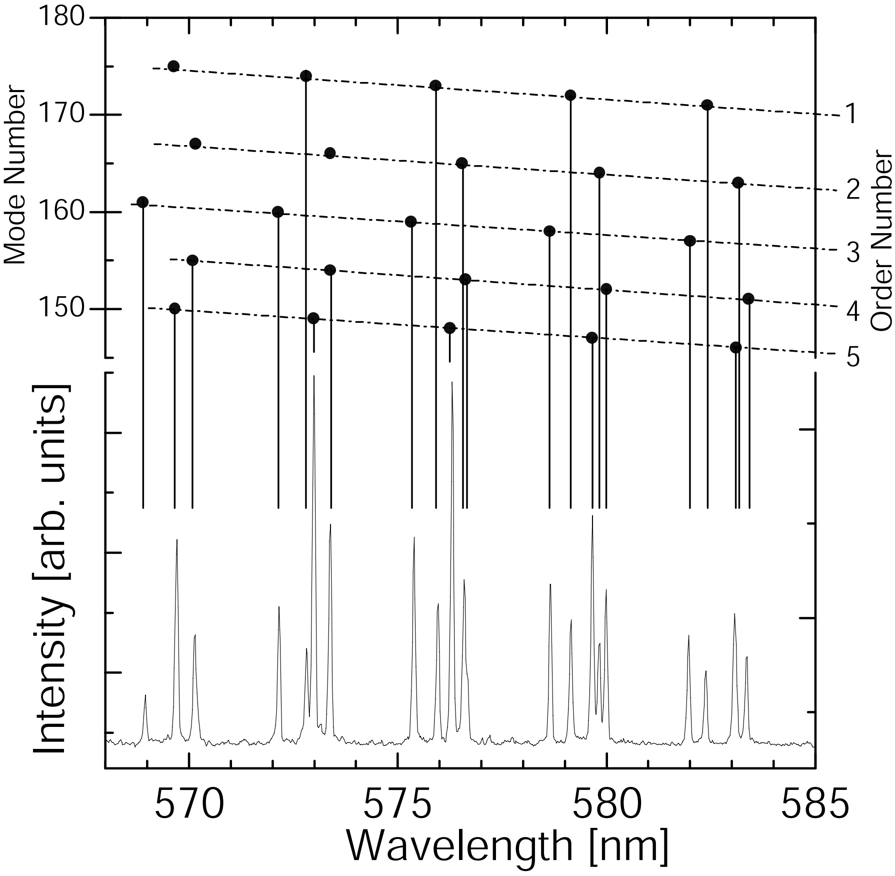

Fig. 4.12: Calculated MDRs mode positions (upper) and the emission spectrum for the droplet of 7×10^{-6} mol/L (lower).

spectrum and are linked to lasing peaks by lines. C is maximized in this case when the refractive index is 1.412 and the droplet radius is 11.86 μm. All lasing peaks shown in this figure are identified as TE modes, which coincides with polarization properties of spatial images and emission spectra as mentioned in the previous subsections. The results of the mode identifications for the droplets of three different concentrations are summarized in Table V. It is confirmed from the assignment that the laser emission of MDRs belongs to a single order number in the case of 7×10^{-4} mol/L and to several modes of lower order numbers in the case of more dilute concentrations.

Table V: Mode identification of MDRs for droplets with various dye concentrations.

		Dye molarity [mol/L]		
		7×10^{-4}	7×10^{-5}	7×10^{-6}
Radius [μm]		12.09	12.32	11.86
Refractive index		1.433	1.406	1.412
Mode number (s)		138-142	161-147	146-174
Order number (l)		7	3-5	1-5
Q value*	TE (s, l)	4.1×10^6 (140, 7)	6.0×10^7 (147, 5)	1.4×10^8 (149, 5)
	TM (s, l)	2.5×10^6 (140, 7)	8.1×10^7 (151, 5)	9.5×10^7 (149, 5)**

*Theoretical Q values of MDRs corresponding to the most intense peaks.
**In this case lasing emission from TM modes was not observed.

4.3.5 Discussion

We discuss three features found in experimental results of microscopic images and emission spectra: 1) As dye concentration decreases, the positions of the laser lines shift toward shorter wavelength, 2) lasing from TM mode occurs at shorter wavelength than that from TE mode and the difference is more distinct with reducing dye concentration, and 3) lasing only from TE modes occurs in the most dilute case studied. A qualitative understanding of these findings follows from the wavelength shift in the gain curves for lasing and the difference between the Q

values of TE and TM modes. An effective Q of a droplet is approximated as [67]

$$\frac{1}{Q} = \frac{1}{Q_0} + \frac{1}{Q_{pert}} , \tag{4.3.4}$$

where Q_0 is a theoretical Q value evaluated from the width of the Mie resonance and Q_{pert} is related to perturbations including internal absorption, internal scattering and shape distortion. However, we take into account only Q_0's as far as discussing the difference between TE and TM modes, since Q_{pert}'s are little affected by the modes.

A gain curve for lasing is approximately given by the difference between the fluorescence and the absorption curves of the dye solution and has a peak around the spectral region of the tail of the absorption spectrum [68]. Decreasing the dye concentration shifts the tail of the absorption spectrum toward the shorter wavelength as shown in Fig. 4.9. Accordingly, the peak of the gain curve and, as a result, lasing peaks shift to the blue.

As seen in Table V, when laser emission occurs from both TE and TM modes, Q_0 of the most intense peak of the TE mode is approximately equal to that of the TM mode for each dye molarity. However, the Q_0's of TE modes are larger than those of TM modes with the same mode number as seen in Chap 2. As an example, Fig. 4.13 shows Q_0's of l = 135 - 150 and s = 5 modes of MDRs. Here the parameters of the droplet were assumed to a = 12 μm and n = 1.4 which correspond to similar ones of the droplets employed in this work. Closed and open circles refer to resonant positions of TE and TM modes, respectively. It is to be noted that the difference between Q_0's of TE and TM modes with the same mode number becomes larger at the shorter wavelength. Since a Q value which is larger than a certain value is required for obtaining sufficient gain, laser emission from TM modes should occur at shorter wavelength than that from TE modes. This explains the difference between the lasing positions of TE and TM modes becomes more pronounced with reducing dye concentration.

For the most dilute dye concentration, however, lasing from only TE modes was observed. In this case, the Q value of the TE mode is much higher than that

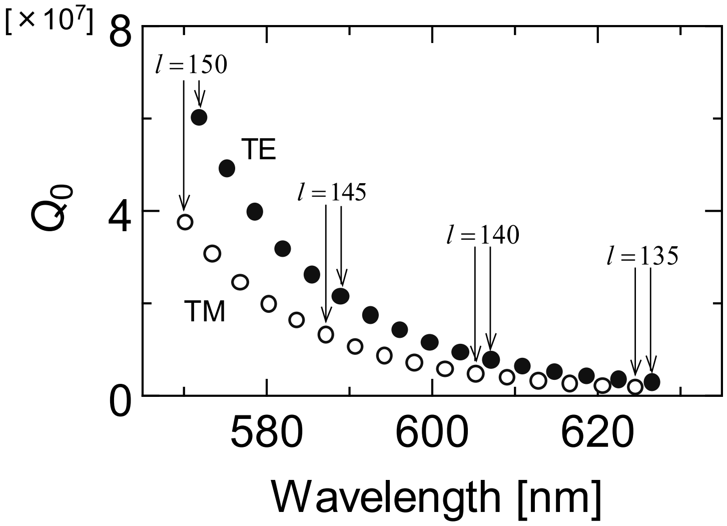

Fig. 4.13: Calculated Q_0's of l = 135 - 150 and s = 5 modes of MDRs. The parameters of the droplet are a = 12 μm and n = 1.4, similar to ones of the droplets in the present observations. Closed and open circles refer to resonant positions of TE and TM modes, respectively.

of the TM mode for MDRs with the same mode and order numbers as seen in Table V and Fig. 4.13. Lasing of TM modes is thus suppressed by the competing TE modes around the region of maximum gain. Since the resonance position of a TM mode with the same Q value as that of a TE mode locates at much shorter wavelength, absorption loss exceeds the gain in such region and the lasing of the TM mode should not occur.

4.3.6 summary

We have investigated the dependence of lasing modes of single dye-doped microdroplets on dye concentrations. Polarization characteristics of both emission spectra and microscopic images were obtained for the molarities of 7×10^{-4}, 7×10^{-5} and 7×10^{-6} mol/L. As the dye concentration decreases, the spectral positions of the laser lines shifted toward shorter wavelength and the structures of the laser lines became more complicated. Except for the most dilute case, lasing from both TE and TM modes was observed. The mode identification of the lasing peaks suggested that lasing of MDRs belongs to a single order number in the most concentrated case and to several order numbers in more dilute cases.

At the most dilute concentration investigated the structure of the lasing spectra was independent of the observation direction and the polarization of the pump beam. In this case, microscopic images revealed that only laser emission with perpendicular polarization to the radial directions emerge from the droplet. These results lead us to conclude that lasing from the droplet originates from coupling only TE modes of MDRs with Rh6G molecules. A qualitative understanding of these findings follows from the analysis of the Q values estimated by the Mie theory. Since the Q value of the TE mode is much larger than that of the TM mode of MDRs with the same mode and order numbers, the TE mode suppresses the gain of the competing TM mode and prevents the TM mode from lasing.

Chapter 5

Conclusion

5.1 Summary of the Present Work

In the present experimental and theoretical work, the lasing properties of spherical microparticles have been investigated. In Chap. 2 we reviewed the Mie theory which is commonly used to investigate light scattering by microparticles. We obtained expressions representing amplitude of electromagnetic fields in side the spherical particles and showed that the MDRs are explained by using these expressions.

In Chap. 3 details of the experimental apparatus have been described. Glycerol droplets doped with Rh6G molecules were generated by a method of electrospray ionization and injected into the ion trap originally developed for this work. The single microdroplets levitated in the ion trap were irradiated by a pulse or a cw frequency-doubled (532 nm) Nd:YAG pump laser. Lasing emission from the droplets was focused onto the slit of a spectrometer equipped with the CCD detector for spectral analysis and was also photographed by using the color CCD camera mounted on the originally developed microscope.

In Chap. 4, we first discussed dependence of lasing modes of the spherical particles on the pump intensities. Microscopic images and emission spectra of a single droplet were simultaneously observed for various pump intensities. Neither the spectra nor the images of strongly excited droplets resembled those of weekly excited ones. From emission spectra, we found that the levitated microdroplet acts as a high Q resonator and lasing action occurs above a certain threshold. Below the threshold, the image was nearly uniform, reflecting the fluorescence from almost entire region of the droplet. Above the threshold, however, the images exhibited symmetrically arranged bright spots near the surface of the droplet, which suggests that the lasing action occurs in specific surface azimuthal modes in the droplet. It was observed for the first time that spatial images of the lasing droplet revealed such a distinct symmetric mode structure.

We next discussed polarization properties of spherical microlasers obtained from both microscopic images and emission spectra. We showed for the first time that polarization of laser light waves from the droplet strongly depended on the observation direction and the polarization of exciting light. The polarization properties were discussed by comparing the rotational relaxation time with the time constant of the lasing and analyzed based on the Mie theory. As a result, we suggested such phenomena occurs because excited molecular dipoles preserved for sufficient period the memory of the polarization of the pump field. The polarization properties allow us to experimentally determine polarization of the lasing modes and are very useful for identifying the modes of MDRs of the lasing spherical microlasers.

Finally, we discussed the lasing modes of the dye-doped microdroplets for the various dye molarities. Reducing the dye concentration results in the drastic change of both emission spectra and microscopic images. As the dye concentration decreases, the spectral positions of the laser lines shifted toward shorter wavelength and the structures of the laser lines became more complicated. At the most dilute concentration the structure of the lasing peaks was independent of the observation direction and the polarization of the pump beam. In this case, microscopic images, on the other hand, reveal that only laser emission with perpendicular polarization to the radial directions emerge from the droplet. These results lead us to conclude that lasing from the droplet originates from coupling only TE modes of MDRs with Rh6G molecules at the most dilute concentration.

A qualitative understanding of these findings follows from the analysis of the Q values estimated by the mode identification of MDRs and the absorption loss of the droplet. Since the Q value of the TE mode is much higher than that of the TM mode at MDRs of the same mode and order number, the TE mode depletes the gain for lasing sufficiently to prevent lasing from the TM mode. Additional investigations are needed to quantitatively resolve these issues.

Temporal properties of the emission from the droplet are not treated in this thesis. The properties play an important role in determination of the Q values of MDRs. When we define τ as the average lifetime of a photon in the resonant mode, the Q value is given by

$$Q = \omega_0 \tau \ , \tag{5.1.1}$$

where ω_0 is the resonant frequency. The theoretically evaluated Q value, including the consideration of the absorption losses, is 1×10^7 for the MDRs identified from the main peaks in emission spectra. Accordingly, the cavity lifetime τ is estimated at 3 ns in our case and is comparable to the pulse width of the pump laser employed in the present study. If we employ the ultra short pulse laser, e.g. mode-locked Ti:sapphire laser, as the pump beam and measure the temporal profiles of the individual laser lines, the cavity lifetime will be experimentally determined and additional information of the MDRs will be obtained. We have such an experimental project as a next step.

5.2 Future Development of this Study

As mentioned in § 2.3.4, we regard the system of a dielectric sphere with MDRs as the photonic atom by analogy with a hydrogen atom. The modes of MDRs penetrating toward outer region of the sphere cause a coherent coupling between spheres. When two photonic atoms are brought together, the photonic molecules will be formed, just as an H_2 molecule is bound due to a overlapping of the wave functions of two H atoms.

We consider the changes in the wave functions of the two H atoms when the atoms are brought together to form a molecule. Figure 5.1 (A) schematically shows the wave functions Ψ_{A} and Ψ_{B} of the two atoms at large separation. When the atoms come close enough, their wave functions overlap and the molecular orbital is formed. The tight binding approximation gives the two combinations: one is $\Psi_{\mathrm{A}} + \Psi_{\mathrm{B}}$ known as the bonding orbital (Fig. 5.1 (B)) and the other is $\Psi_{\mathrm{A}} - \Psi_{\mathrm{B}}$ known as the antibonding orbital (Fig. 5.1 (C)). Each orbital shares two electrons with the two protons. The electron in the bonding orbital exists midway between the two protons, which represents the attractive potential of both protons. On the other hand, the probability density of the electron in the antibonding orbital varnishes at the center of the nuclei, which represents the bonding disappearance.

When the atoms are widely separated, the two wave functions lead to the same

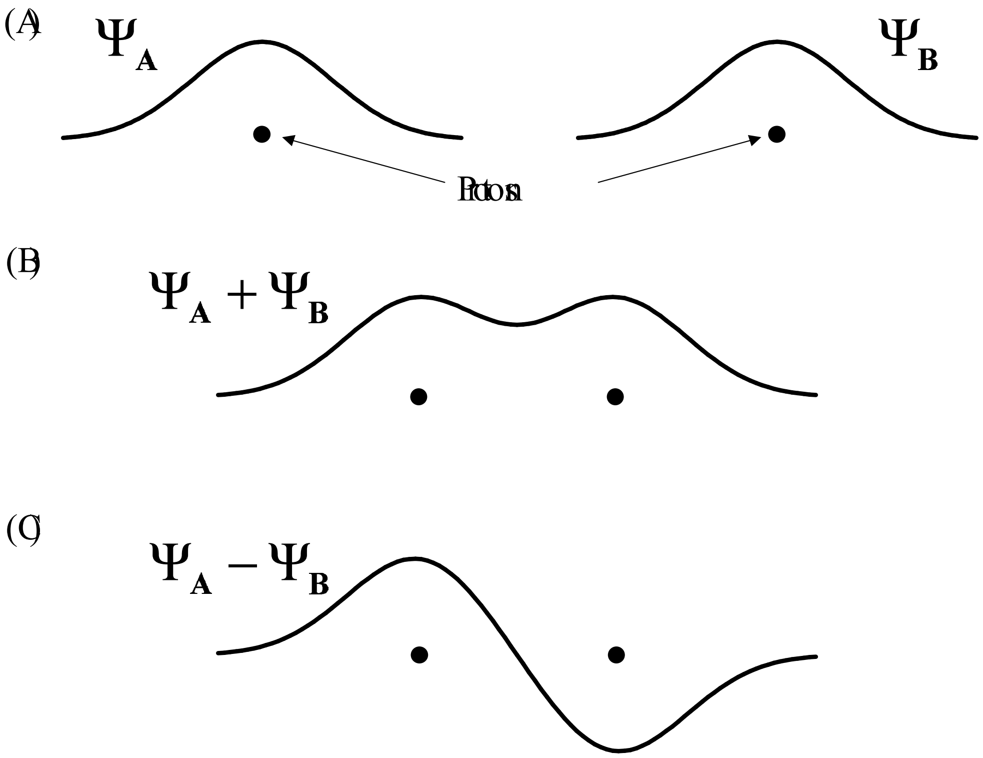

Fig. 5.1: (A) The wave functions Ψ_{A} and Ψ_{B} of the two atoms at large separation. (B) The bonding orbital $\Psi_{\mathrm{A}} + \Psi_{\mathrm{B}}$. (C) The antibonding orbital $\Psi_{\mathrm{A}} - \Psi_{\mathrm{B}}$.

energy, that is, energy levels corresponding to such wave functions are degenerate as shown in Fig 5.2 (A). When the atoms are brought together, however, the degeneracy is removed and two separated level are formed. The electron in the bonding orbital will have a somewhat lower energy than that in the antibonding orbital. When two photonic atoms are brought together, the modes of MDRs penetrating toward the outer region of sphere overlap. The modes with same resonant frequency then split to two coupled modes as shown in 5.2 (B) and the photonic molecules are formed. Mukaiyama *et al.* have reported such intersphere coupled modes in ref. [41].

If we can control the interaction between photonic atoms, we will develop novel type of photonic devices and manipulate photons in micrometer scale. Most recently, we have originally developed a laser manipulation system (see Appendix C). Using the system, we can manipulate spheres in micrometer length scale and

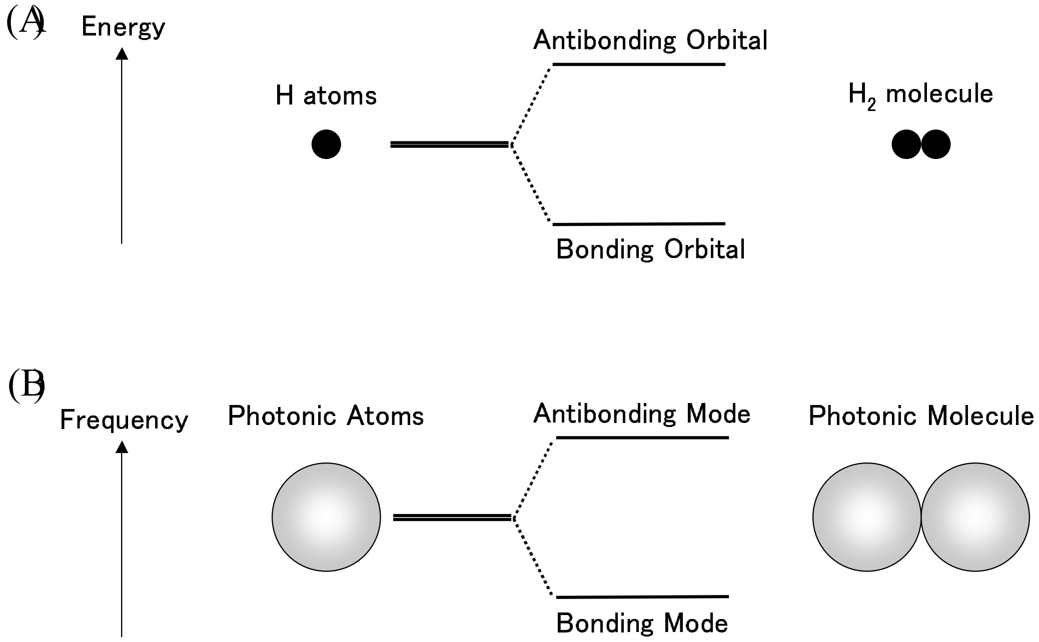
(A)
Energy
Antibonding Orbital
H atoms
H2 molecule
Bonding Orbital
(B)
Frequency
Photonic Atoms
Antibonding Mode
Photonic Molecule
Bonding Mode

Fig. 5.2: (A) The splitting of the degenerate energy level of the H atoms is schematically drawn. (B) The modes with same resonant frequency split to two coupled modes.

control the distance between the spheres. As shown in Fig 5.3 (A), we assume the photon is confined in a coupled mode of the photonic molecules. When two spheres are separated and the interaction is removed, the photon propagates toward the outer region of the sphere as shown in Fig 5.3 (B). The development of such photonic devices is now in progress in our laboratory.

In order to achieve the manipulation of the light wave for application, much attention has been attracted up to now to photonic crystals [69, 70]. In the photonic crystals which have the periodic dielectric structure, light waves experience a periodic scattering potential, just as electrons are scattered by an periodic electric potential in a crystal. As a result frequency gaps can be formed, which are called photonic band gaps (PBG). Using PBG devices is an approach for the photon manipulation. Such an approach is based on the band theory of the solid state physics, whereas an approach by using photonic molecules is on the method of

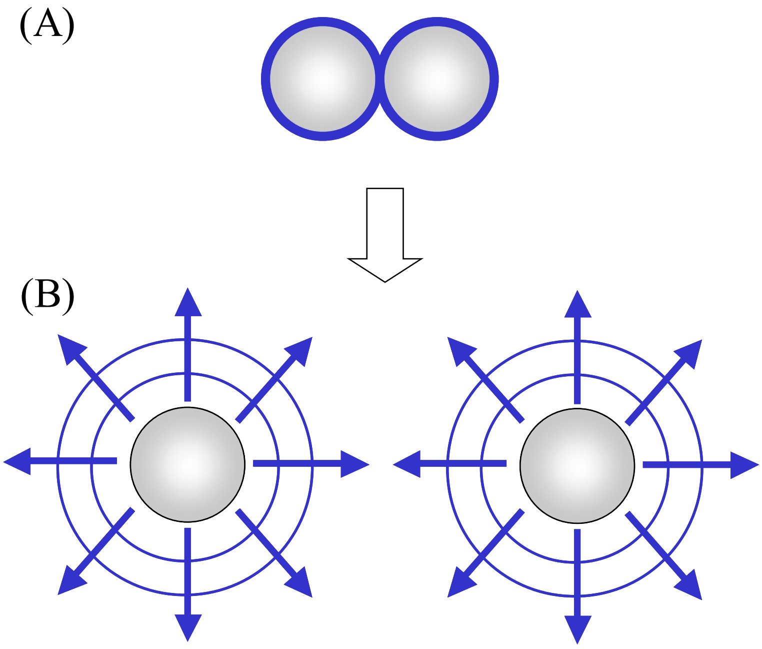

Fig. 5.3: (A) The photon is confined in the photonic molecule. (B) By removing the interaction between the two spheres the photon propagates toward the outer region of the sphere.

molecular orbitals as mentioned above. The microspheres will be a candidate of a key element for novel photonic devices.

Appendix A

Drawings of Ion Trap Assembly

In what follows we show the drawings of the middle and the end electrodes (Fig. A.1), the top plate (Fig. A.2) and the sidewall (Fig. A.3).

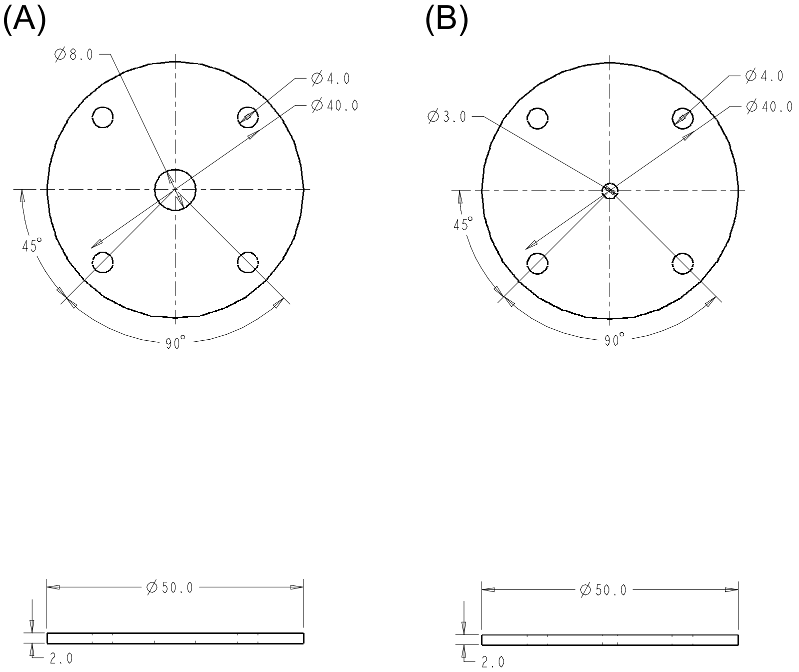
(A)
Ø8.0
Ø4.0
Ø40.0
45°
90°
Ø50.0
2.0
(B)
Ø3.0
Ø4.0
Ø40.0
45°
90°
Ø50.0
2.0

Fig. A.1: The drawings of (A) the middle electrode and (B) the end electrode.

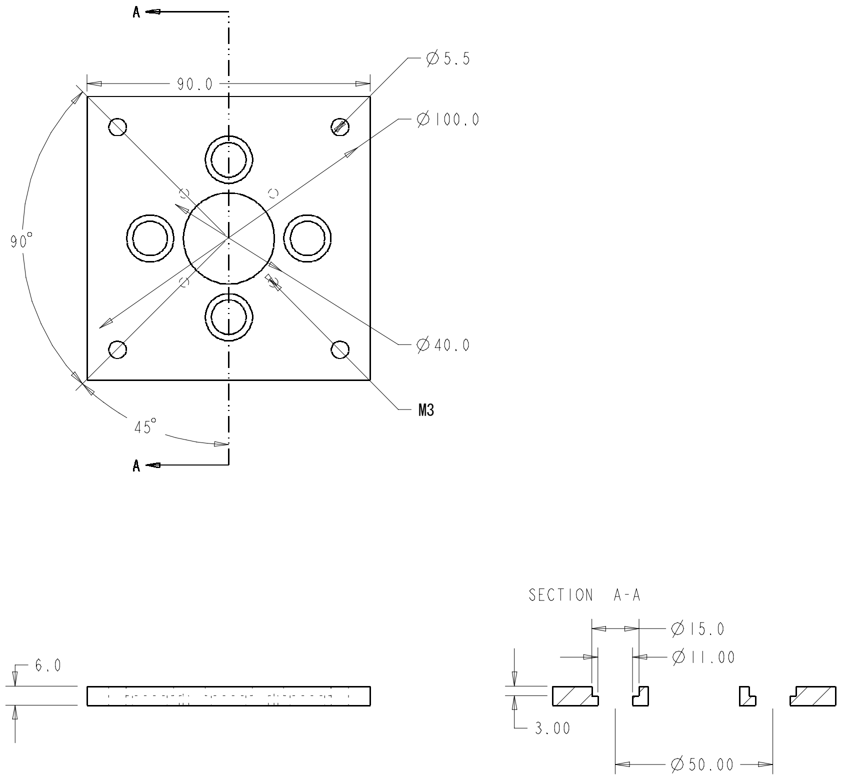
A
Ø5.5
90.0
Ø100.0
90°
Ø40.0
M3
45°
A
SECTION A-A
Ø15.0
Ø11.00
6.0
3.00
Ø50.00

Fig. A.2: The drawing of the top plate.

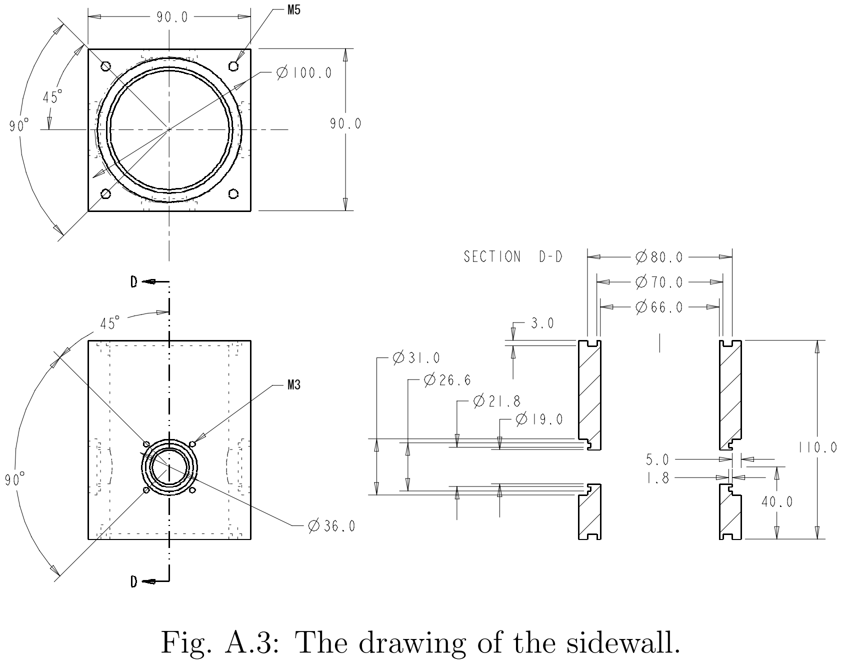
90.0
M5
Ø100.0
45°
90°
90.0
SECTION D-D
Ø80.0
Ø70.0
Ø66.0
D
45°
3.0
Ø31.0
Ø26.6
Ø21.8
Ø19.0
M3
90°
5.0
1.8
110.0
40.0
Ø36.0
D

Fig. A.3: The drawing of the sidewall.

Appendix B

Laser Manipulation System

Since Ashkin [3] discovered the optical levitation technique for small particles, laser manipulation systems have been widely applied to the manipulation of spherical particles [5, 71], biological cells [72], metal particles [73] and so on. In order to manipulate spheres in micrometer scale and to control the distance between the spheres, we have developed a laser manipulation system. Here we briefly describe the principle of the laser trapping based on geometric optics and show the apparatus of this system and some observations of trapped microparticles.

We consider laser beams focused onto a spherical particle as shown in Fig. B.1. We assume that the refractive index of the particle is greater than that of

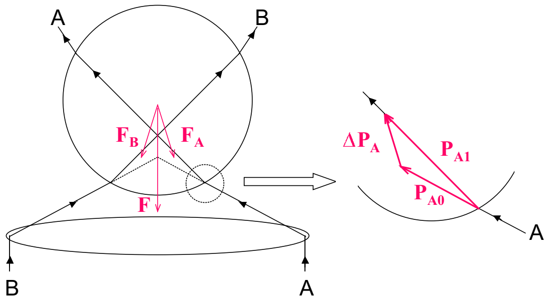

Fig. B.1: Principle of optical trapping. Refraction and reflection at the surface of the particle cause momentum transfer from photon to the particle. The refraction of the ray A leads to the light momentum change $\mathbf{\Delta P_A}$ as shown in the right side.

the surrounding medium. Reflection (not shown in this figure) and refraction at the surface of the particle cause momentum transfer from incident light to the particle. The principal transfer occurs when the ray is incident on the particle, as shown in the right side of this figure. The refraction of the ray A leads to the light momentum change $\Delta\mathbf{P_A} = \mathbf{P_{A1}} - \mathbf{P_{A0}}$, where $\mathbf{P_{A0}}$ and $\mathbf{P_{A1}}$ are photon momenta before and after refraction, respectively. The particle is given the momentum $-\Delta\mathbf{P_A}$ due to conservation laws and is afforded the radiation force $\mathbf{F_A}$. The momentum of the ray B also changes as the same as that of the ray A and the particle is afforded $\mathbf{F_B}$. As a result, the particle is accelerated toward the focal region of the incident beam and is trapped at this region.

Figure B.2 depicts the apparatus of the laser manipulation system. We employ a cw YAG laser (750 mW, LCS-DTL-322, LASER-COMPACT Co. Ltd) for trapping particles. The laser beam is reflected by a two-galvanomirror set (VM2000, GSI LUMONICS Co. Ltd) which is controlled by a computer and is expanded by lenses L1 and L2. The expanded beam is reflected by a right angle prism and

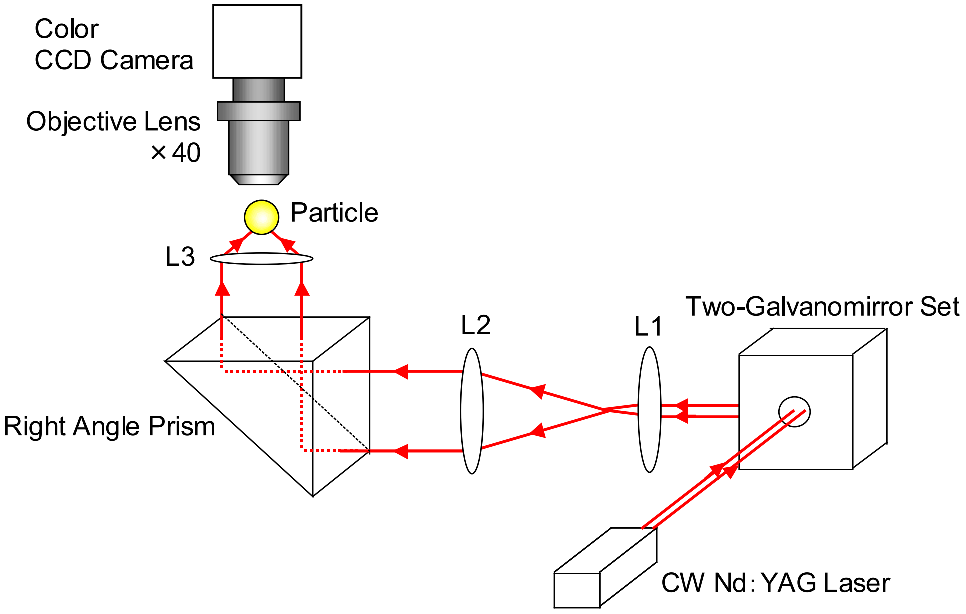

Fig. B.2: The apparatus of the laser manipulation system.

is focused onto a particle by a lens L3 with N. A. = 0.3. The optically levitated particle is monitored by using a microscope.

Figure B.3 (A) shows photographs before (a) and after (b) trapping a 13 μm polystyrene spherical particle. The particle denoted by an arrow in (b) was

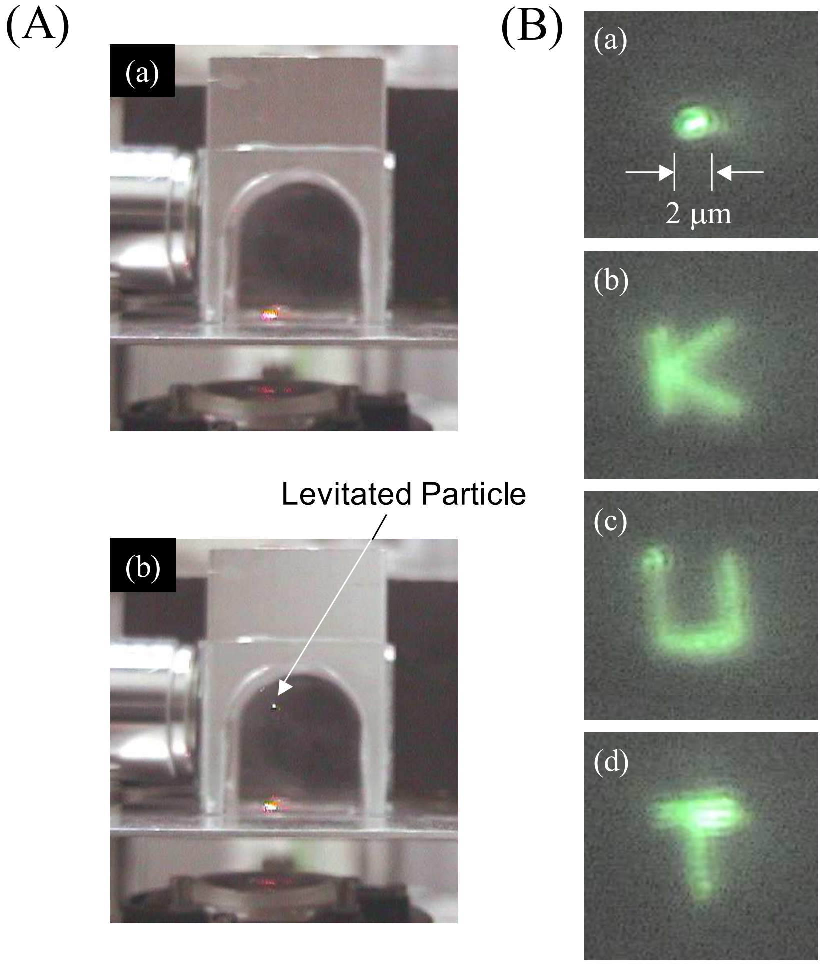

Fig. B.3: (A) Photographs before (a) and after (b) trapping the 13 μm polystyrene spherical particle. The optically levitated particle is denoted by the arrow in (b). (B) The particle in (a) was extremely stable and remained for hours. In (b) through (d) by scanning the laser beam, the particle was moved along the characters "K, U and T".

optically levitated about 1 cm above a glass substrate and its scattered light was detected. Figure B.3 (B) shows microphotographs of a 2 μm particle. Elastically scattered green light was recorded by the microscope as shown in Fig B.2. The particle in (a) was extremely stable and was fixed in space for hours. When we scan the laser beam by the two galvanomirrors, the trapped particle is manipulated along the beam trajectory. Figure B.3 (B) (b) through (d) show the particle was moved along the characters "K, U and T".

The next step of this study is the development of the device which can manipulate photons in micrometer size scale. The system is useful for the development of novel photonic devices based on the photonic molecules as mentioned in Chap. 5. By using such a system, we can control the distances between the particles in micrometer scale and construct photonic devices.

Bibliography

[1] L. Rayleigh: "The Problem of the Whispering Gallery," in *Scientific Papers* (Cambridge University Press, Cambridge, 1912) p. 617-620.

[2] R. K. Chang and A. J. Campillo (Eds): *Optical Processes in Microcavities* (World Scientific Publishing, Singapore, 1996).

[3] A. Ashkin: "Acceleration and Trapping of Particles by Radiation Pressure," Phys. Rev. Lett. **24** (1970) 156.

[4] A. Ashkin: "Applications of Laser Radiation Pressure," Science **210** (1980) 1081.

[5] A. Ashkin and J. M. Dziedzic: "Stability of Optical Levitation by Radiation Pressure," Appl. Phys. Lett. **24** (1974) 586.

[6] R. Thurn and W. Kiefer: "Structural Resonances Observed in the Raman Spectra of Optically Levitated Liquid Droplets," Appl. Opt. **24** (1985) 1515.

[7] J. B. Snow, S.-X. Qian and R. K. Chang: "Stimulated Raman Scattering from Individual Water and Ethanol Droplets at Morphology-Dependent Resonances," Opt. Lett. **10** (1985) 37.

[8] A. Biswas, H. Latifi, R. L. Armstrong and R. G. Pinnick: "Double-Resonance Stimulated Raman Scattering from Optically Levitated Glycerol Droplets," Phys. Rev. Lett. **40** (1989) 7413.

[9] R. E. Benner, P. W. Barber, J. F. Owen and R. K. Chang: "Observation of Structure Resonances in the Fluorescence Spectra from Microspheres," Phys. Rev. Lett. **44** (1980) 475.

[10] S. Holler, N. L. Goddard and S. Arnold: "Spontaneous Emission Spectra from Microdroplets," J. Chem. Phys. **108** (1998) 6545.

[11] E. M. Purcell: "Spontaneous Emission Probabilities at Radio Frequencies," Phys. Rev. **69** (1946) 681.

[12] S. Haroche and J.-M. Raimond: "Cavity Quantum Electrodynamics," Scientific American, Apr. (1993) 26.

[13] A. J. Campillo, J. D. Eversole and H-B. Lin: "Cavity Quantum Electrodynamic Enhancement of Stimulated Emission in Microdroplets," Phys. Rev. Lett. **67** (1991) 473.

[14] M. D. Barners, W. B. Whitten, S. Arnold and J. M. Ramsey: "Homogeneous Linewidths of Rhodamine 6G at Room Temperature from Cavity-Enhanced Spontaneous Emission Rates," J. Cham. Phys. **97** (1992) 7842.

[15] M. D. Barnes, C.-Y. Kung, W. B. Whitten, J. M. Ramsey, S. Arnold and S. Holler: "Fluorescence of Oriented Molecules in a Microcavity," Phys. Rev. Lett. **76** (1996) 3931.

[16] C. G. Garret, W. Kaiser and W. L. Long: "Stimulated Emission into Optical Whispering Modes of Spheres," Phys. Rev. **124** (1961) 1807.

[17] S.-X. Qian, J. B. Snow, H.-M.Tzeng and R. K. Chang: "Lasing Droplets: Highlighting the Liquid-Air Interface by Laser Emission," Science **231** (1986) 486.

[18] J. B. Snow, S.-X. Qian and R. K. Chang: "Nonlinear Optics with a Micrometer-Size Droplet," Opt. News, May (1986) 5 .

[19] A. Biswas, H. Latifi and R. L. Armstrong: "Time-Resolved Spectroscopy of Laser Emission from Dye-Doped Droplets," Opt. Lett. **14** (1989) 214.

[20] M. K. Gonokami, K. Takeda, H. Yasuda and K. Ema: "Laser Emission from Dye-Doped Polystyrene Microsphere," Jpn. J. Appl. Phys. **31** (1992) L99.

[21] J. F. Owen, R. K. Chang and P. W. Barber: "Determination of Optical Fiber Diameter from Resonances in the Elastic Scattering," Opt. Lett. **6** (1981) 272.

[22] R. K. Chang, J. F. Owen, P. W. Barber, B. J. Messinger and R. E. Benner: "Inelastic Light Emission from Spherical Particles and Cylindrical Fibers," J. Raman Spectros. **10** (1981) 178.

[23] R. L. Armstrong: "Nonlinear Optical Effects in Microcylinders and Microdroplets," Chap. 7 of ref. [2].

[24] J. F. Owen, P. W. Barber, P. B. Dorain and R. K. Chang: "Enhancement of Fluorescence Induced by Microstructure Resonances of a Dielectric Fiber," Phys. Rev. Lett. **47** (1981) 1075.

[25] S. L. McCall, A. F. J. Levi, R. E. Slusher, S. J. Pearton and R. A. Logan: "Whispering-Gallery Mode Microdisk Lasers," Appl. Phys. Lett. **60** (1992) 289.

[26] J. Faist, C. Gmachl, M. Striccoli, C. Sirtori, F. Capasso, D. L. Sivco and Y. Cho: "Quantum Cascade Disk Lasers," Appl. Phys. Lett. **69** (1996) 2456.

[27] Y. Kawabe, Ch. Spiegelberg, A. Schülzgen, M. F. Nabor, B. Kippelen, E. A. Mash, P. M. Allemand, M. K. Gonokami, K. Takeda and N. Peyghambarian: "Whispering-Gallery-Mode Microring Laser Using a Conjugated Polymer," Appl. Phys. Lett. **72** (1998) 141.

[28] S. C. Hill, C. K. Rushforth, R. E. Benner and P. R. Conwell: "Sizing Dielectric Spheres and Cylinders by Aligning Measured and Computed Resonance Location: Algorithm for Multiple Orders," Appl. Opt. **24** (1985) 2380.

[29] J. D. Eversole, H.-B. Lin, A. L. Huston and A. J. Campillo: "Spherical-Cavity-Mode Assignments of Optical Resonances in Microdroplets Using Elastic Scattering," J. Opt. Soc. Am. A **7** (1990) 2159.

[30] H.-M. Tzeng, K. F. Wall, M. B. Long and R. K. Chang: "Evaporation and Condensation Rates of Liquid Droplets Deduced From Structure Resonances in the Fluorescence Spectra," Opt. Lett. **9** (1984) 273.

[31] G. Chen, Md. M. Mazumder, R. K. Chang, J. C.Swindal and W. P. Acker: "Laser Diagnostics for Droplet Characterization: Application of Morphology Dependent Resonances," Prog. Energy Combust. Sci. **22** (1996) 163.

[32] W. B. Whitten, J. M. Ramsey, S. Arnold and B. V. Bronk: "Single-Molecule Detection Limits in Levitated Microdroplets," Anal. Chem. **63** (1991) 1027.

[33] A. Schülzgen, S. Arnold and G. Griffel: "Excitation of Resonances of Microspheres on an Optical Fiber," Opt. Lett. **20** (1995) 654.

[34] N. Dubreuil, J. C. Knight, D. K. Leventhal, V. Sandoghdar, J. Hare and V. Lefè vre: "Eroded Monomode Optical Fiber for Whispering-Gallery Mode Excitation in Fused-Silica Microspheres," Opt. Lett. **20** (1995) 813.

[35] O. Sbanski, V. E. Roman, W. Kiefer and J. Popp: "Elastic Light Scattering from Single Microparticles on a Femtosecond Time Scale," J. Opt. Soc. Am. A **17** (2000) 313.

[36] Y. Yamamoto and R. E. Slusher: "Optical Processes in Microcavities," Physics Today, June (1993) 66.

[37] F. J. Duarte: *Tunable Lasers Handbook*, ed. F. J. Duarte (Academic Press, Inc., San Diego, 1995) Chap. 5.

[38] D. R. Lide (Ed): *CRC Handbook of Chemistry and Physics* (CRC Press, Inc., Boca Raton, 1996) 77th ed. **6**-112.

[39] S. Arnold, S. Holler and S. D. Druger: "Imaging Enhanced Energy Transfer in a Levitated Aerosol Particle," J. Chem. Phys. **104** (1996) 7741.

[40] S. Arnold, N. L. Goddard and S. C. Hill: "Nonclassical Polarization Effects in Fluorescence Emission Spectra from Microdroplets," J. Chem. Phys. **111** (1999) 10407.

[41] T. Mukaiyama, K. Takeda, H. Miyazaki, Y. Jimba and M. Kuwata-Gonokami: "Tight-Binding Photonic Molecule Modes of Resonant Bispheres" , Phys. Rev. Lett. **82** (1999) 4623.

[42] J. D. Jackson: *Classical Electrodynamics* (John Wiley & Sons, Inc., New York, 1998) 3rd ed., Chap. 9.

[43] G. B. Arfken and H. J. Weber: *Mathematical Methods for Physicists* (Harcourt/Academic Press, San Diego, 2001) 5th ed., Chap. 1.

[44] C. F. Bohren and D. R.Huffman: *Absorption and Scattering of Light by Small Particles* (John Wiley & Sons, Inc., New York, 1983) Chap. 4.

[45] See Chap. 8 of ref. [43] for splitting the partial differential equations into a set of ordinary differential equations.

[46] See Chap. 12 of ref. [43] for the detail explanation of the associated Legendre functions.

[47] See Chap. 11 of ref. [43] for the detail explanation of the spherical Bessel functions.

[48] See p. 771 of ref. [43] for the relation between the Legendre polynomials and the Bessel functions of the first kind.

[49] See Chaps. 4 and 5 of ref. [42] for the Maxwell's boundary conditions of the electric and magnetic fields, respectively.

[50] H. C. van de Hulst: *Light Scattering by Small Particles* (Dover Publications, New York, 1981) Chap. 9.

[51] S. C. Hill, and R. E. Benner: *Optical Effects Associated with Small Particles*, ed. P. W. Barber and R. K. Chang (World Scientific, 1988) Chap. 1.

[52] P. W. Barber and S. C. Hill: *Light Scattering by Particles: Computational Methods* (World Scientific Publishing, Singapore, 1996) Chap. 4.

[53] See Chap. 9 of ref. [42] for the orbital angular momentum operator.

[54] P. Eisberg and R. Resnick: *Quantum Physics of Atoms, Molecules, Solids, Nuclei and Particles* (John Wiley & Sons, Inc., New York, 1985) 2nd ed., Chap. 7.

[55] W. Paul: "Electromagnetic traps for charged and neutral particles," Rev. Mod. Phys. **62** (1990) 531.

[56] S. Zhang and J. Jin: *Computation of Special Functions* (John Wiley & Sons, Inc., New York, 1996) Chap. 14.

[57] P. Chýlek, J. T. Kiehl and M. K. W. Ko: "Optical Levitation and Partial-Wave Resonances," Phys. Rev. A **18** (1978) 2229.

[58] H. Taniguchi, H. Tomisawa and J. Kido: "Ultra-Low-Threshold Europium Chelate Laser in Morphology-Dependent Resonances," Appl. Phys. Lett. **66** 1578 (1995).

[59] H.-M. Tzeng, K. F. Wall, M. B. Long and R. K. Chang: "Evaporation and Condensation Rates of Liquid Droplets Deduced from Structure Resonances in the Fluorescence Spectra," Opt. Lett. **9** (1984) 273.

[60] P. P. Feofilov: *The Physical Basis of Polarized Emission* (Consultants Bureau, Inc., New York, 1961) Chap. 4.

[61] G. R. Fleming: *Chemical Applications of Ultrafast Spectroscopy* (Oxford University Press, Inc., New York, 1986) Chap. 6.

[62] S. Kinoshita, I. Tanaka, T. Kushida, Y. Kinoshita and S. Kimura: "Time-Dependent Fluorescence Depolarization of Fluorescein in Rat Thymus Lymphocytes," J. Phys. Soc. Jpn. **51** (1982) 598.

[63] K. Kamada, K. Sasaki, H. Misawa, N. Kitamura and H. Masuhara: "Picosecond Lasing Dynamics of a Single Dye-Doped Microparticle in Solution," Chem. Phys. Lett. **210** (1993) 89.

[64] S. Arnold, S. Holler, J. H. Li, A. Serpengüzel, W. F. Auffermann and S. C. Hill: "Aerosol Particle Microphotography and Glare-Spot Absorption Spectroscopy," Opt. Lett. **20** (1995) 773.

[65] See Chap.12 of ref. [50]

[66] J. D. Eversole, H. -B. Lin, A. L. Huston, A. J. Campillo, P. T. Leung, S.Y. Liu and K. Young: "High-Precision Identification of Morphology-Dependent Resonances in Optical Processes in Microdroplets," J. Opt. Soc. Am. B, **10** (1993) 1955.

[67] M. M. Mazumder, D. Q. Chowdhury, S. C. Hill and R. K. Chang : "Optical Resonances of a Spherical Dielectric Microcavity: Effects of Perturbations," Chap. 6 of ref. [2].

[68] H.-B. Lin, A. L. Huston, B. L. Justus and A. J. Campillo: "Some Characteristics of a Droplet Whispering-Gallery-Mode Laser," Opt. Lett. **11** (1986) 614.

[69] J. S. Foresi, P. R. Villeneuve, J. Ferrera, E. R. Thoen, G. Steinmeyer, S. Fan, J. D. Joannopoulos, L. C. Kimerling, H. I. Smith and E. P. Ippen: "Photonic-bandgap microcavities in optical waveguides," Nature **390** (1997) 143.

[70] E. Chow, S. Y. Lin, S. G. Johnson, P. R. Villeneuve, J. D. Joannopoulos, J. R. Wendt, G. A. Vawter, W. Zubrzycki, H. Hou and A. Alleman: "Three-dimensional control of light in a two-dimensional photonic crystal slab," Nature **407** (2000) 983.

[71] A. Ashkin and M. Dziedzic: "Feedback Stabilization of Optically Levitated Particles," Appl. Phys. Lett. **30** (1977) 202.

[72] A. Ashkin: "Forces of a Single-Beam Gradient Laser Trap on a Dielectric Sphere in the Ray Optics Regime," Biophys. J. **61** (1992) 569.

[73] K. Sasaki, M. Koshioka, H. Misawa, N. Kitamura and H. Masuhara: "Optical Trapping of a Metal Particle and a Water Droplet by a Scanning Laser Beam," Appl. Phys. Lett. **60** (1992) 807.